3D Elements for Phased-Array Systems
Analysis and Design

Yepes Juliá, Cristina

DOI
10.4233/uuid:32d708da-ef49-44f0-82fc-33f98f491594

Publication date
2020

Document Version
Final published version

Citation (APA)
Yepes Juliá, C. (2020). *3D Elements for Phased-Array Systems: Analysis and Design*. [Dissertation (TU Delft), Delft University of Technology]. https://doi.org/10.4233/uuid:32d708da-ef49-44f0-82fc-33f98f491594

3D Elements for Phased-Array Systems

Analysis and Design

3D Elements for Phased-Array Systems

Analysis and Design

DISSERTATION

for the purpose of obtaining the degree of doctor
at Delft University of Technology
by the authority of the Rector Magnificus, Prof. dr. ir. T.H.J.J. van der Hagen,
chair of the board for Doctorates,
to be defended publicly on 17th January 2020 at 12:30 o'clock.

by

Cristina YEPES JULIÁ

Master of Science in Telecommunication Engineering,
Public University of Navarra, Spain,
born in Murcia, Spain.

This dissertation has been approved by the promotors.

Composition of the doctoral committee:

Rector Magnificus	Chairman
Prof. dr. ir. A. Neto,	Delft University of Technology, promotor
Prof. dr. ir. F. E. van Vliet,	University of Twente, promotor
Dr. ir. D. Cavallo,	Delft University of Technology, copromotor
Independent members:	
Prof. dr. S. Maci,	University of Siena, Italy
Prof. dr. C. Craeye,	Université catholique de Louvain, Belgium
Prof. dr. P. Knott,	RWTH Aachen University, Germany
Prof. dr. ir. A. Yarovoy,	Delft University of Technology, Netherlands
Other member:	
Dr. ir. S. Monni,	TNO Defense, Safety and Security, daily supervisor
Reserve member:	
Prof. dr. ir. N. Llombart,	Delft University of Technology, Netherlands

Dr.ir. S. Monni has, as a daily supervisor, contributed significantly to the preparation of this dissertation.

The work presented in this thesis has been performed at TU Delft and TNO and financed by TNO.

Keywords: Frequency Selective Surfaces, spatial filters, phased array antennas, angular filtering, Floquet theory, Additive Manufacturing (AM), three-dimensional (3-D) printing.

Printed by: Ipskamp Drukkers B.V., Enschede, Netherlands.

Cover design: Cristina Yepes.

An electronic version of this dissertation is available at: http://repository.tudelft.nl/

ISBN 978-94-028-1862-8

To my family and friends

Contents

Chapter 1

Introduction

Phased array antennas are gaining in popularity. They seem no longer to be of interest only for military (radar) systems, but are encountered today in many civilian systems, such as mobile communication base stations, car radars, etc. A phased array antenna is a group of individual radiators, positioned in such a way as to produce a maximum radiation into a specific direction. By changing the phase distribution of the elements, it is possible to create a maximum coherent radiation into a desired direction.
Phased array antenna technology has been in use for some decades, mostly for radar applications. Despite the maturity that this technology has reached at the present time, there are still issues related to the practical implementation of phased array antennas, especially when deployed in complex electromagnetic environments, such as base stations for 5G applications, radar on ship decks, SATCOM terminal antennas on an airplane fuselage. Some specific problems that require novel and advanced solutions are addressed in this thesis and consist of sea clutter, scan loss and frequency selectivity.

- **Angular selectivity**: Phased arrays operating in densely populated areas, such as a base stations in urban environment or radar on a ship deck, are subject to interference due to own signal back scattered by nearby objects located in the field-of-view of the antenna, e.g. buildings surrounding the base station, or the sea illuminated by the radar. While this problem was typically tackled by implementing spatial filtering through suitable pattern nulling algorithms, with the advent of digital beamforming alternative strategies are needed. In this thesis an approach is proposed at antenna element pattern level, by properly shaping the radiation pattern.

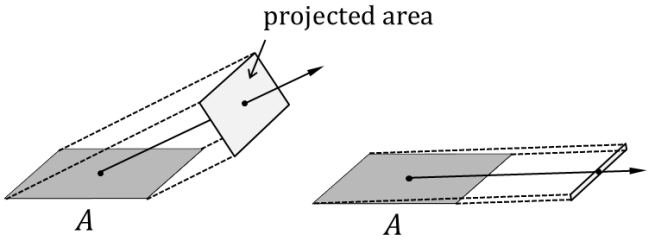

Figure 1.1: Reduction of projected area of a flat radiating aperture for wide scanning.

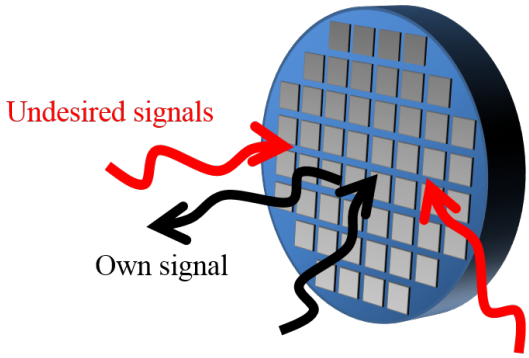

Figure 1.2: Interference due to nearby radiating systems.

- **Scan loss**: Typically, the array gain peaks at the bore sight, implying that the scan gain decreases as the scan angle moves away from the bore sight. The scan loss is defined as the relative gain loss with respect to the bore-sight scan. For a rectangular radiating aperture, the scan loss is typically proportional to the cosine of the elevation angle, corresponding to the projected geometrical aperture reduction (see Fig. 1.1). The system performance and the sensitivity of the radar would greatly benefit from a reduced gain variation within the scan range.

  Additional issues such element mismatch losses or other efficiency problems, i.e. surfaces waves and edge effects, can also affect the scan loss of the array.

- **Frequency selectivity**: It is crucial for phased array systems to avoid spurious interferences due to the continuously growing use of wireless systems operating in adjacent or overlapping frequency bands (see Fig. 1.2). Band-pass filters are needed between the antenna and the Low Noise Amplifiers (LNAs) to avoid receiver desense. Also, in the transmit chain, filters are needed to suppress the emission of harmonic frequency components and to comply with standard regulations for emission outside the operating band. The physical size of these filters is relatively large, thus occupying

a large fraction of the available surface, when used in phased array applications. In this perspective, new antenna concepts should be proposed, where the radiating antenna element itself already performs part of the filtering function (filtering antenna or filtenna), such to relax the requirements on the filters placed down in the front-end chain.

In order to overcome these issues, a number of new antenna solutions will be investigated in this work. The aim is to propose concepts capable of:

- increasing the frequency selectivity, with focus on out-of-band rejection and suppression of high order harmonics.
- achieving wide scanning in azimuth with minimized gain variation within the field of view.
- Increase the angular selectivity, by enhancing the gain for scanning to large positive angles, and purposely reducing the gain for negative angles.

To reach these goals, additional degrees of freedom can be used that are not commonly employed in the design of phased arrays. Thanks to the novel emerging manufacturing techniques (e.g. injection molding - antenna in package-, three-dimensional printing) 3D elements could be realized, eliminating the need to implement elements in the usual printed (horizontal) configuration and allowing for volumetric elements that have a vertical dimension.

1.1 Frequency Selectivity

Active phased array antennas must comply with stringent requirements in terms of sensitivity to interference caused by other nearby radiating systems, especially in complex platforms, which are populated by an ever increasing number of sensors and communication systems. Radio-frequency (RF) interference can cause a number of issues, e.g. saturation of the array receiver, with consequent loss of sensitivity and missed detections, or increased false alarm rates. This performance degradation can be prevented by implementing frequency selective functions in the antenna panel and RF front-end. For this purpose, filters are inserted in the transmit/receive module of the individual antenna elements (see Fig. 1.3(a)), although this approach can be problematic due to the limited available physical space.

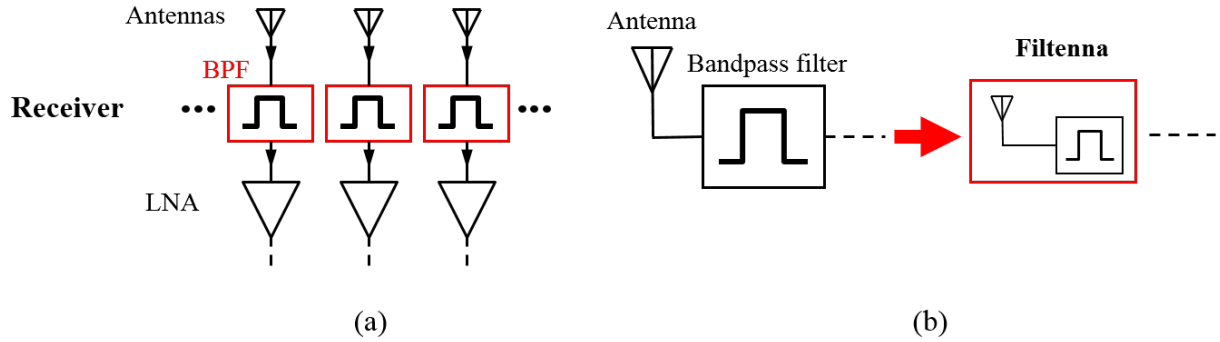

Figure 1.3: (a) Filters inserted in the receive module of the individual antenna elements, and (b) filtenna concept: the radiating antenna element itself already performs the filtering function.

A possible method to realize compact filters is to use the antenna element itself to perform part of the filtering function, implementing the so called filtenna concept [1–4] (see Fig. 1.3(b)). An example of a phased array unit cell design with integrated filtering properties was presented in [5]. However, higher-harmonic suppression was achieved over a small frequency bandwidth and scanning of the antenna array caused detuning of the filter response.

Another approach to block the undesired radiation is the implementation of frequency selective surfaces (FSSs). The advantage of this latter solution is to alleviate the complexity of the antenna feed structure or the RF front-end by reducing the requirements on other filtering stages [6]. Nevertheless, FSSs can also suffer from the appearance of higher-order harmonics close to the operational bandwidth and their response can strongly vary with the angle of incidence [7]. FSSs typically consist of one or multiple layers composed of resonant elements arranged in periodic grids [7]. An approach to improve the angular stability is to add additional quarter-wave ($\lambda/4$) dielectric slabs on the two sides of the FSS [7,8]. However, such a solution leads to electrically thick structures and is not effective in rejecting higher-order harmonics.

Recently, an improved concept based on miniaturized-element FSS (MEFSS) was proposed in [9]. This solution consists of a number of layers, each made of a periodic arrangement of sub-wavelength elements. Considering that the elements are much smaller than the wavelength, the behavior of each layer can be represented as a shunt impedance (capacitive or inductive), with respect to a plane-wave propagation, over a large frequency range [10]. The design of a MEFSS suppressing harmonic responses was presented in [11], and achieved stable behavior for oblique incidence in the principal planes. The thickness was electrically small, less than $\lambda/10$, rather than a multiple of $\lambda/4$, resulting in lower losses. Nevertheless,

in [11] or in other more recent designs [12] the FSS was only characterized and tested under plane-wave illumination. It is therefore still an unexplored aspect the interaction of FSSs in close proximity of antennas, being essential to determine the behaviour of such filtering solution in a realistic scenario.

1.2 Angular Coverage and Selectivity

Modern antenna arrays for radar and communication applications are required to provide wide bandwidth and high gain, with directive and electronically steerable beams. To satisfy the requirements of the antennas in terms of gain and scan angle, different approaches can be used such as conformal antennas and phased arrays with wide-angle impedance matching (WAIM).

1.2.1 Conformal Array Antennas

To realize a close to hemispherical angular coverage with nearly constant gain, multi-panel configurations [13–16] or conformal arrays [17] have been proposed. An overview of different approaches to achieve full hemispherical scan coverage was presented in [18]. One solution that does not require any mechanical steering consists of a pyramidal arrangement of several planar phased array faces [13, 14], as shown in Fig. 1.4(a) and (b). When increasing the number of faces, the individual array needs to scan over a reduced angular range. In such multi-panel arrays, only one of the faces needs to be operational at any given time and the face is switched as required. However, an added advantage is that more than one array can be operating simultaneously for communication with different satellites simultaneously, providing multiple beam coverage.

Another variation of a phased array concept with hemispherical scan coverage is to arrange the radiating elements on a spherical surface [15], as shown in Fig. 1.4(c). For the sake of a simpler practical implementation, the spherical surface was approximated in [15] as a number of small flat triangular faces. In this configuration, each triangular subarray panel constitutes a module. The beam scanning is provided by switching the appropriate combination of modules on or off, and by providing phase shift to the elements in each module. Based on this concept, a hemispherical phased array operating at Ku-band was developed in [17], for in-flight entertainment. With respect to the relevant requirements of a Satcom user terminal antenna, this solution achieves good scan performance at the cost of increased volume. More specifically, the final optimized antenna in [17] combines both receive and transmit capabilities at Ku-band in the same aperture.

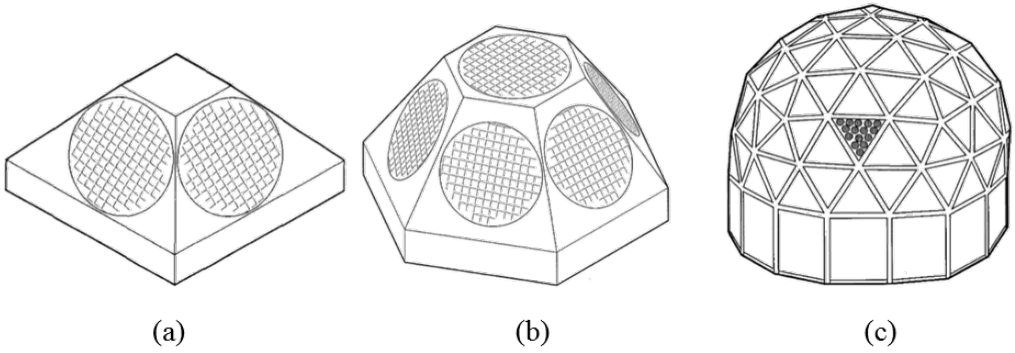

Figure 1.4: (a) A four-panel phased array arrangement: individual array scans ±45°; (b) a seven-panel phased array arrangement: individual array scans ±30°; and (c) schematic of a Geodesic sphere phased array antenna [15].

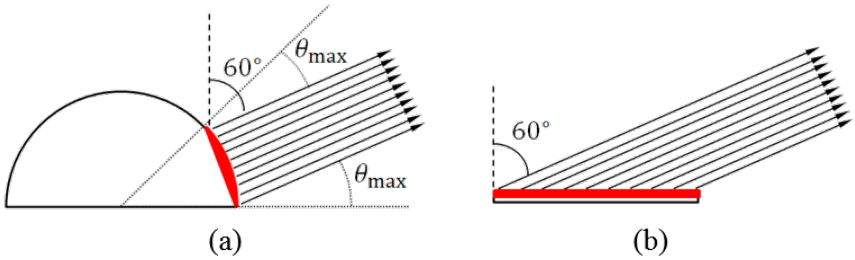

Figure 1.5: Maximum scan angle for (a) conformal and (b) planar array.

However, the height of the structures are still too large to be installed on airplanes without significant impact on the aircraft drag and on the fuel consumption. Moreover, a conformal antenna configuration requires to switch electronically between different sectors of the radiating aperture to scan the beam to different directions. As depicted in Fig. 1.4(c) the generation of two pencil beams pointing to different angles utilizes different active regions of the radiating surface. Since the active sub-array covering a part of the field of view is composed by a small subset of the total number of elements, the number of transmit/receive (T/R) modules is largely oversized and results in a significant increase in volume occupation and cost of the array.

On the other hand, by employing different portions of the array for different angular region, the requirements on maximum scan angle are greatly relaxed. This concept is explained in Fig. 1.5, where a conformal array and a planar array are depicted, assuming that both scan to 60 degrees with the same projected area. It can be observed that, for the planar array, the maximum scan angle for all elements of the array (under local periodicity assumption)

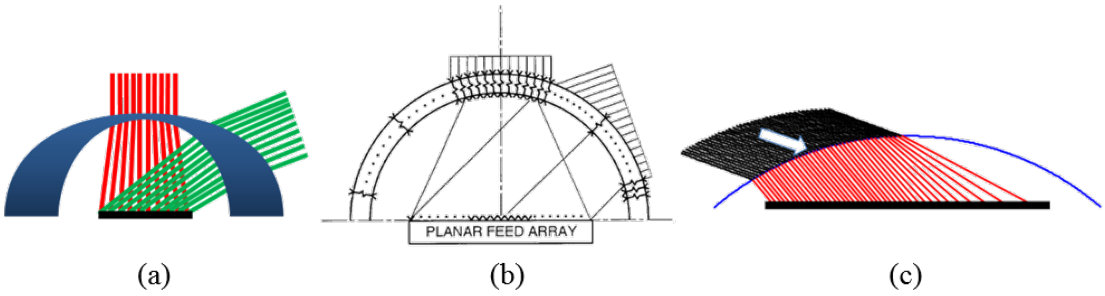

Figure 1.6: (a) Dielectric, (b) transmitarray and (c) metasurface domes to enhance the scan range of a planar phased array.

coincides with the pointing angle. On the contrary, for the conformal aperture, the elements of the array radiate much closer to broadside and the maximum scan angles for the elements at the edge of the active subarray is much smaller than the pointing angle of 60 degrees. For this reason, all the performance parameters that typically deteriorate for very large scanning angles, such as the polarization purity and the matching efficiency, remain very good for conformal arrays. Since only one sector of the conformal array contributes to the radiated field, to maintain the same gain as for a planar array configuration, the conformal array needs to be much larger. Thus, although it allows for a less dense sampling, a conformal array still contains a high number of radiating elements. Indeed, in the design in [17], the number of radiating elements is 1440 with an inter-element spacing comparable to the wavelength at the highest frequency of operation.

1.2.2 Dome

To avoid the excessive number of T/R modules typical of conformal array structures and to enlarge the field of view of an array antenna, a different approach involves the use of a single planar phased array in combination with a curved dome. The dome has the function of generating collimated beams with enhanced scan range and gain coverage, when illuminated by the phased array. The dome can be realized as a dielectric lens [19,20], as sketched in Fig. 1.6(a). An alternative implementation is based on a transmitarray concept, as proposed in [21], and is shown in Fig. 1.6(b). The main drawback of such a solution is, besides the weight, the overall height of the structure. For example, in the implementation presented in [20] and [21], the dome height is approximately equal to the array length. To reduce the overall height of the structure, a meta-surface dome was proposed in [22]. This consists of an electrically thin passive surface realized with a locally periodic metal pattern printed on a dielectric substrate, where both the size of the metal elements and the period are sub-

wavelength. The surface implements a phase gradient that deflects the incident rays coming from the array aperture. Such metasurfaces are also referred to as Huygens surfaces [23,24] when they are perfectly matched, thus characterized by unitary transmission. It is seen that a single printed layer for realizing a metasurface cannot provide a perfect matching of a plane wave with a phase shift that varies over a range of 360. However, the introduction of three tightly coupled metasurface layers, whose total thickness is still electrically thin, can provide perfect matching and full 2 phase variation [24]. The practical implementation of such a concept is still not trivial, since a multi-layer printed circuit board cannot be easily realized with a curved shape. Thus a multi-faceted version of the dome would be beneficial. Moreover this type of solution is typically narrowband. Recently in [25] a novel design for an all electric dome was proposed, which allows preserving the operating band required for terminal antennas while increasing the scan angle.

Regardless of the manufacturing aspects, the main drawback of this approach is the complexity of the beamforming, which requires optimized amplitude and phase control at element level for every direction of scanning, frequency and polarization. In fact, it was shown in [22] that a predistortion of amplitude and phase applied to the planar feed phased array is necessary to improve the scan performance when combined with the dome.

Planar antenna arrays require only a simpler linear phase shift and a static amplitude taper to be used to form the beams. However, as the antenna array scans, the active input impedance of the elements changes as a function of scan angle. The impedance varies differently in the two principal scanning planes. In particular, this variation is proportional to $1/\cos(\theta)$ while scanning in the H-plane and proportional to $\cos(\theta)$ when scanning in the E-plane. This change in impedance causes a decrease of efficiency, since more power is reflected at the antenna element feed, because of an impedance mismatch.

1.2.3 Wide-Angle Impedance Matching

A wide angle impedance matching (WAIM) layer can be placed as a superstrate above a phased array antenna. This was originally proposed in [26] and consisted of an electrically thin dielectric layer located in the close vicinity of the array, to mitigate the impedance mismatch while scanning. Being planar and very close to the array plane, the WAIM can be integrated with the array in a single PCB. The design of WAIMs have been investigated for a long time [26], but is still a wide researched topic. Today much research is done into the use of artificial dielectrics or metamaterials in WAIMs to improve its performance, either in scanning range or operational bandwidth [26–30].

State-of-the-art performance for wideband and wide scan arrays were demonstrated in [30],

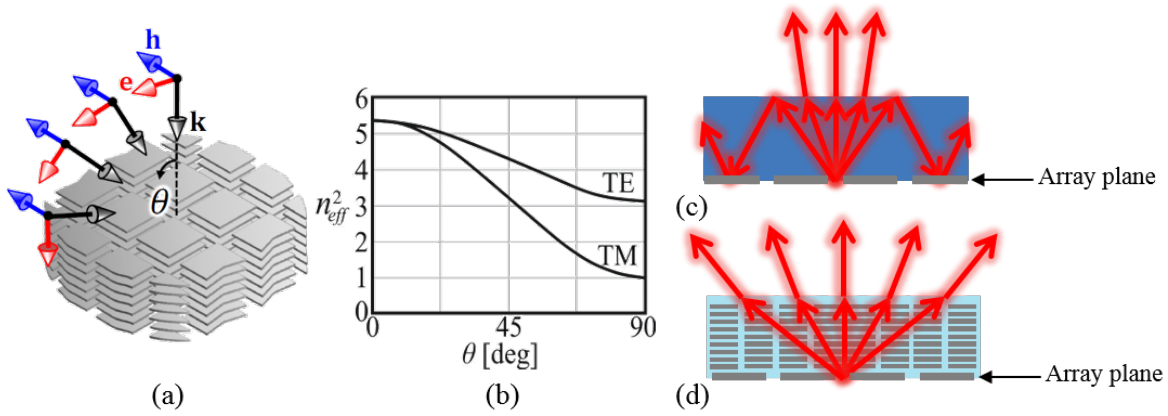

Figure 1.7: (a) Artificial dielectric layers to realize an equivalent anisotropic material. (b) Equivalent refractive index as a function of the angle of incidence. (c) Scan blindness in array with dielectric superstrate and (d) avoidance of surface wave with ADL superstrates.

where a connected slot array integrated with an artificial dielectric WAIM (see Fig. 1.7) was proposed. An artificial dielectric consists of periodic metallic patches, small with respect to the wavelength, embedded in a host material in order to create an equivalent material with modified properties (Fig. 1.7(a)). The equivalent electromagnetic parameters of the artificial material can be engineered by properly designing the spatial density of the metallic inclusions. The main advantage of an artificial dielectric compared to a real dielectric is the anisotropy, i.e. the effective refractive index of the ADLs decreases with the angle of incidence of a plane wave propagating through the material, as shown in Fig. 1.7(b). This is a key property to avoid the excitation of surface waves: an isotropic dielectric slab placed above a radiating array supports surface waves when scanning, because of the total internal reflection at its top surface (Fig. 1.7(c)); on the contrary, artificial dielectric slabs synthesize a lower and lower permittivity for increasing angles of incidence, so that the critical angle never occurs at their interface with free space (Fig. 1.7(d)). This avoids the occurrence of scan blindness even for very large scanning angles.

When combining the connected slot array with the artificial dielectric superstrate, the presence of the artificial dielectric above the radiating elements enhances the upward radiation, so that the distance between the array plane and the ground plane can be largely reduced without strong alterations of the performance. This allows to realize the feeding structure with standard vias, so that the array is low-cost and easier to manufacture, compared to the vertical arrangement of the antenna PCBs. Moreover, the artificial dielectric also performs a wideband impedance transformation, to widen the frequency bandwidth (the bandwidth

is proportional to the number of layers). A prototype demonstrator based on the described concept was recently presented in [30]. The array was shown to be able to scan with good matching efficiency up to ±60° on one main plane and to ±80° on the other plane, over an octave bandwidth up to Ku-band. However, while improving the matching performance, the planar integrated WAIM does not increase the gain coverage, which is still limited by the projected area of the array aperture. Therefore, because of the planar configuration, the full gain coverage can only be obtained with additional minor mechanical scanning to increase the projected area, or by using multiple array panels.
In cases where a full coverage is not needed, the design of antennas with asymmetric radiation pattern would allow to increase the gain coverage.

1.2.4 Pattern Shaping

In addition to wide bandwidth and high gain, antenna arrays for radar and communication applications often operate in environments where a multitude of sensors and radiating systems need to co-exist. As already mentioned, to avoid interference between different antenna systems, the implementation of angular filtering functions can be beneficial. Moreover, in some of the mentioned applications, it is sometimes not required for the antennas to exhibit a field of view that is symmetric with respect to broadside, but rather a gain profile that is stable over a certain desired angular region.

To obtain wide-scan capability while still maintaining a low antenna profile, hybrid scanning methods have been implemented [31–34]. The approach used in these works is to replace the typical planar array configuration, with symmetric field of view, with an array that scans the beam from broadside to a positive, as high as possible, angle. This asymmetric scan behaviour can be optimized by tilting the element pattern. The full coverage is then achieved by mechanical rotation of the array along the azimuth. An array of tilted stacked patches for digital video broadcast terminals was presented in [33], providing a 20 to 70 degrees coverage in elevation through electronic scan and 360 degrees in azimuth through mechanical scan. The design choices were aimed at minimizing the number of active modules, and thus the cost of the array. The asymmetric element pattern allowed reducing the amplitude of the grating lobes that appear due to an array spacing larger than half wavelength. However, with this configuration, the grating lobe level remains only 5.8 dB lower than that of the main lobe. Further attempts have been done to reduce the radiation toward undesired directions, while maintaining a large element spacing, e.g. in [34], by resorting to an overlapped beam-forming network. However, the improvement

in terms of pattern selectivity is achieved at the cost of a more complex feeding architecture. Although the mentioned works employed skewed antenna elements, the behavior of this type of arrays in terms of radiation characteristics has not been investigated in detail. The symmetry properties of arrays of antennas with asymmetric current distribution were studied in [35, 36], based on a Floquet analysis.

Other existing solutions for pattern shaping include amplitude and phase weighting of the elements [37–39] and density taper [40, 41], requiring complex beam forming structures to control independently the amplitude and phase of each element. Element level pattern diversity has also been used in [42] to combine different modes in the radiating elements as an additional degree of freedom.
Angular filters have been realized mainly with frequency selective surfaces or leaky wave structures [43–45], with the aim of increasing the directivity and reducing the levels of the side lobes or grating lobes. In [46, 47], rectilinear leaky-wave antennas were synthesized to realized radiation patterns with angular selectivity and asymmetry properties. However, with this concept, the entire array radiates a broad beam with an angular passband filtering function, precluding the possibility to generate highly directive beams that can be scanned within the field of view of interest.

1.3 Additive Manufacturing Technologies

Additive manufacturing (AM) is emerging as a promising technology for the development of novel antennas and radio frequency (RF) components. Numerous advantages can be recognized with respect to standard fabrication techniques, such as freedom in 3D shaping, mass production, design optimization taking also into account mechanical and thermal constraints, and implementation of different RF functionalities, e.g. radiating element, interposer and packaging, in a small volume.
Different AM technologies are applied to the design of RF components and described in the literature. In [48] Fused Deposition Modeling (FDM) is used to manufacture a corrugated horn antenna at 10 GHz with Acrylonitrile Butadiene Styrene (ABS) plastic and metallized afterwards with silver painting. This technology offers the advantage of allowing for the design of a circular to rectangular transition, along with the horn antenna. In [49] a coplanar wire-patch (CWP) working at 2.5 GHz is printed applying inkjet printing technology. The CWP is realized with a Kapton film lying on a Rohacell foam. As seen in [48], AM technology not only help in the fabrication of 3D shapes but also can offer

a solution to create transitions to connect different devices or to manufacture different components in a single piece. In [50] an antenna is fabricated in one piece consisting of a corrugated feed horn, a subreflector with its supports, and a main reflector in Ku-band using Stereolithography (SLA).

Moreover, antennas have been manufactured using techniques for AM of metals. Feed horn antennas can be manufactured through selective laser melting (SLM) technology. Single-band and dual-band all-metal prototypes were manufactured in [51] working at different bands (K, Ku and Q/V-bands). The main advantages of using SLM to fabricate horn antennas are that the external profile can be optimized in order to reduce the overall mass and envelope to avoid the use of external supporting structures, and to minimize thermal stresses arising during fabrication.

Nevertheless, AM mixed material antenna, where printed polymer is combined with printed or paste-like metal, are seldom explored. The capability of embedding metal lines in the 3D printed polymers would be an asset to obtain a higher level of integration in antennas. In [52] a small V-shaped meandered line dipole antenna operation at 1 GHz is fabricated combining conductive nanoparticle ink, from IIMAK family, and 3D printed dielectric material (Rexolite). In [53] an artificial material operating in X-band with metallic cuboid inclusions in a dielectric host material is manufactured. The dielectric is been fabricated with a FDM printer using Thermoplastic polyester polylactic acid (PLA) material. Conductive silver paste is used to fill the empty cuboids and subsequently a second layer of PLA was printed, embedding the metal layer. In these AM mixed material solutions, higher discrepancies are found between simulations and measurements due to the poor quality of the polymers (high losses) combined with the low conductivity of the metal paste. Moreover, deformation of the plastic substrate while applying thermal curing to the metal traces is observed. In [54] a two steps approach is applied, first 2-polymers 3D printing, with conventional PLA for the antenna substrate and graphene conductive PLA for the metal traces, then selective galvanic electrochemical deposition of Cu on these traces. This approach allows for highly conductive metal traces. The main drawback is that it requires two separate processing steps.

The availability of mixed materials additive manufacture potentially paves the way toward (quasi-) monolithic implementation of RF front-ends, with the possibility of embedding RF circuits and components and radiating elements in relatively small volumes [55]. This technology provides additional degrees of freedom for the design of high frequency Antennas in Package (AiP), enabling heterogeneous integration, potentially reducing the losses associated with interconnections, and overcoming misalignment errors [56–58]. However, the characterization of the losses and the efficiency associated to additive manufacturing

processes and material is still subject of intense investigation in the antenna and microwave community and in this thesis an antenna design aiming at quantifying the electrical properties of mixed material additive manufacturing (AM) technology will be described.

1.4 Novel Contributions in this Thesis

The main novel aspects that have been investigated can be summarized as follows:

- The design of a bandpass MEFSS with harmonic rejection properties together with a study on the effects of placing it in the close proximity of a phased array antenna. For this purpose, we use the connected array of dipoles developed in [60]. The investigation of the performance of the combined array-MEFSS system is relevant, since the vicinity of the array to the FSS can cause variations of both the FSS response and the array matching or radiation patterns. The distance should be selected such to avoid the propagation of guided modes between the array plane and the FSS within the operational bandwidth.

- A study of the effects of the fabrication inaccuracies on the performance of the FSS since it can produce significant differences between simulations and measurements [12]. This investigation is useful to identify the geometrical parameters that are most critical for the correct prediction of the performance. This information can be used as guideline for the design of MEFSSs that are more robust against manufacturing errors.

- An extended analysis of the symmetry properties of array antennas with asymmetric current distribution. The analysis in [35] was only addressing the cases of planar antenna elements in infinite array environment. Here, we aim to extend the analysis to elements that can have vertical components in the current distribution, focusing also on inter-element spacing exceeding half wavelength, and to study the asymmetric radiation properties of finite arrays.

- The derivation of a periodic spectral method of moments (MoM) capable of modeling skewed dipoles. Analytical expressions are derived for the active input impedance of tilted dipoles, by assuming a single sinusoidal basis function to describe the current distribution. The active element patterns are also evaluated in closed form and a parametric analysis is then performed to show how the radiation patterns vary with the inter-element distance and the inclination angle of the dipoles. The study

provides useful design guidelines for tilted element arrays to achieve desired radiation characteristics.

- The design of a practical linear phased array antenna of tilted dipole elements to achieve asymmetric radiation characteristics. The dipoles are loaded with artificial dielectrics to increase the gain in certain desired angular regions. An implementation of the array based on printed circuit technology (PCB) is proposed, as well as the design of the feed structure.

- A case of study to assess the potentialities of mixed material AM technology at high frequencies using a 3D configuration of a miniaturized Frequency Modulated Continuous-Wave (FMCW) radar, based on the concept described in [82].

1.5 Outline of the Thesis

This thesis is structured in three main parts. In the first part, which consists of Chapters 2, the focus is on the frequency selective surfaces and their integration with wide scanning wideband phased arrays. The second part, which comprises Chapters 3 and 4, reports on the theoretical analysis and practical design of arrays with an asymmetric radiation pattern. The third part, which constitutes Chapter 5, focuses on the study of additive manufacturing techniques for high frequencies. More in detail, the dissertation is organized as follow:

- In **Chapter 2**[1], the design of a MEFSS is presented, based on a equivalent circuit model. A prototype of the MEFSS is manufactured and tested in the proximity of a phased array antenna. A dispersion analysis is performed to define the optimum distance between the FSS and the antenna to avoid the propagation of surface waves.

- **Chapter 3**[2] presents an investigation in terms of radiation and impedance properties of antenna arrays of tilted dipoles. A spectral method of moments (MoM) is developed for the analysis of infinite and finite arrays with arbitrarily tilted dipoles elements in free space or in the presence of a backing reflector. From this study guidelines to design arrays with asymmetric radiation pattern are derived.

[1] This chapter is an extended version of the published article [J1] (see p. 117)
[2] This chapter is an extended version of the published article [J2] (see p. 117)

- In **Chapter 4**[3], the study done in the previous chapter and the guidelines extracted from it are used to design a linear array of tilted dipoles to achieve radiation patterns with asymmetric angular filtering characteristics. A prototype of this design is manufactured and measured to validate the findings of the study in Chapter 3.
- **Chapter 5** presents a dipole antenna manufactured with additive manufacturing (AM) technology at 24 GHz. Measurements of the antenna are provided together with a briefly discussion of the challenges related to the use of AM processes for the manufactured of high frequency RF antennas and components.
- **Chapter 6** concludes with a review of the most significant results presented in this thesis and an outlook on possible future developments.

[3]The content of this chapter has been submitted for publication in [J3] (see p. 117)

Chapter 2

Angularly Stable Frequency Selective Surface

This chapter presents the design of a bandpass Miniaturized-Element Frequency Selective Surface (MEFSS) with harmonic rejection properties. The MEFSS design is based on an equivalent circuit model, where the inter-layer interaction is only described with a single transmission line representing the fundamental Floquet wave. A prototype of the designed MEFSS is fabricated, consisting of 5 metallic layers separated by a dielectric slab and exhibiting good stability over a wide conical incidence range, up to 45 degrees. Moreover, we study the effects of placing such a design in the close proximity of a wide-scanning connected array of dipoles to implement a phased array with integrated filtering properties. A dispersion analysis is performed to define the distance between the array and the FSS that avoids the propagation of surface waves between the combined structure, allowing to maximize the radiation efficiency. The performance of the array combined with the MEFSS is experimentally characterized, showing high-order harmonic rejection better than 17 dB over a large bandwidth.

2.1 Design of the Frequency Selective Surface

In this section, a multilayer FSS is designed with bandpass and harmonic rejection properties. The targeted bandwidth is about 20% centered around 4 GHz. The starting point for the FSS design is a 3-pole Chebyshev low-pass prototype filter (see Fig. 2.1(a)), where the values for the coefficients g_n can be calculated using the equations in [61], [62] and collected in Table 2.1.

The series element is then transformed using the admittance inverter topology [62] shown

Table 2.1: Geometrical parameters of the coefficients of g of a low pass filter of third order.

g_0	g_1	g_2	g_3	g_4
1	0.6292	0.9703	0.6292	1

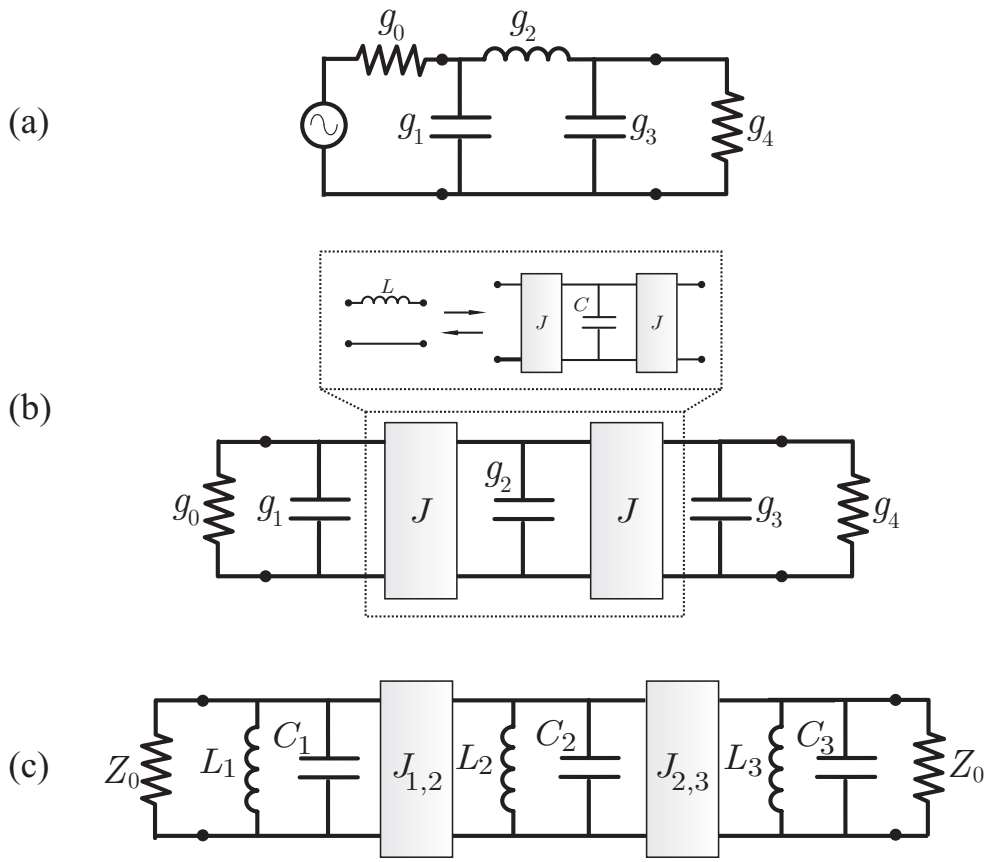

Figure 2.1: Circuit model of a (a) 3-pole Chebyshev low-pass filter, (b) 3-pole Chebyshev low-pass filter using admittance inverter and (c) 3-pole Chebyshev band-pass filter.

in Fig. 2.1(b), where J is the characteristic admittance of the inverter. The low-pass prototype is transformed in a bandpass response centered at 4 GHz (see Fig. 2.1(c)). Admittance inverters can be realized as a Pi-network of inductances as shown in Fig. 2.2(a), where the inductance value can be calculated as

$$L = \frac{1}{\omega J} \tag{2.1}$$

A Pi-to-T transformation is applied with all the inductances, combining some of them for this purpose, and the equivalent circuit is shown in Fig. 2.2(b). The final equivalent circuit is depicted in Fig. 2.2(c), where the series inductances and part of the shunt capacitances

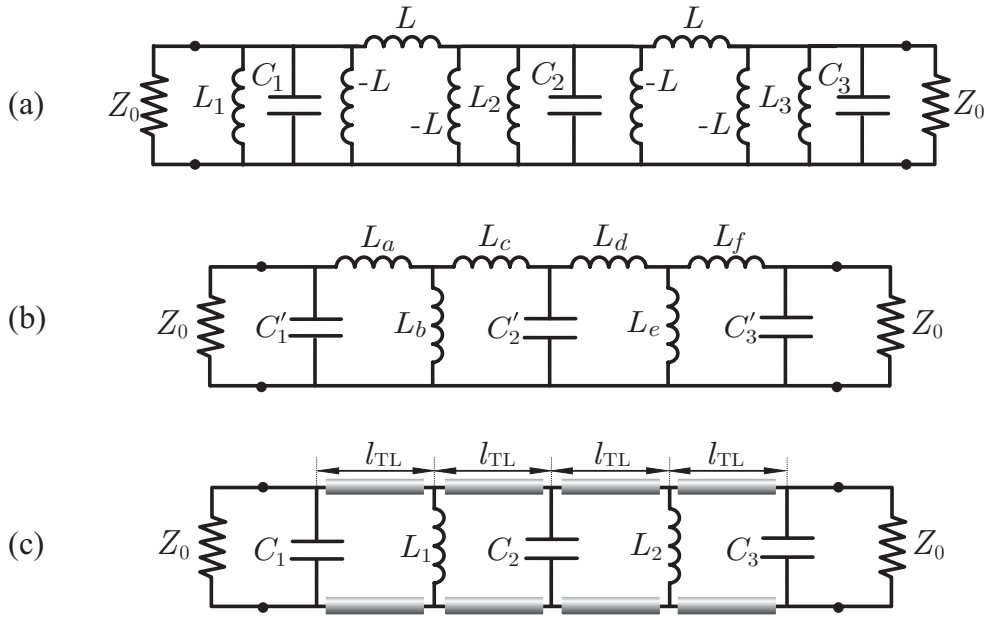

Figure 2.2: (a) Transformation of the admittance inverters shown in Fig. 2.1(c) into a Pi-network of inductances, (b) Pi-to-T transformation between inductances, and (c) final equivalent circuit where the series inductances are replaced by short transmission lines.

are replaced by short transmission lines. The value of the shunt lumped components and the length of the transmission lines (assuming a relative permittivity of $\varepsilon_r = 4.5$) are shown in Table 2.2. These values were calculated considering a desired bandwidth of about 20% at the central frequency of 4 GHz.

Table 2.2: Values of the Lumped Elements and the Transmission Lines

C_1	C_2	C_3	L_1	L_2	$l_{\mathrm{TL}}, h_{diel}$
235 fF	455 fF	235 fF	2.03 nH	2.03 nH	3.175 mm

The capacitive and inductive layers can be realized with metallic periodic meshes and the transmission line sections are represented by dielectric slabs separating the metal layers, as shown in Fig. 2.3(a). The simplest way of realizing a capacitive layer is by using periodic sub-wavelength metal square patches, while the inductive layer can be realized as a periodic metal grid [63]. A first dimensioning of the geometrical parameters of these layers to achieve a desired value of capacitance or inductance can be done, for normal incidence, by using the expressions given in [64]:

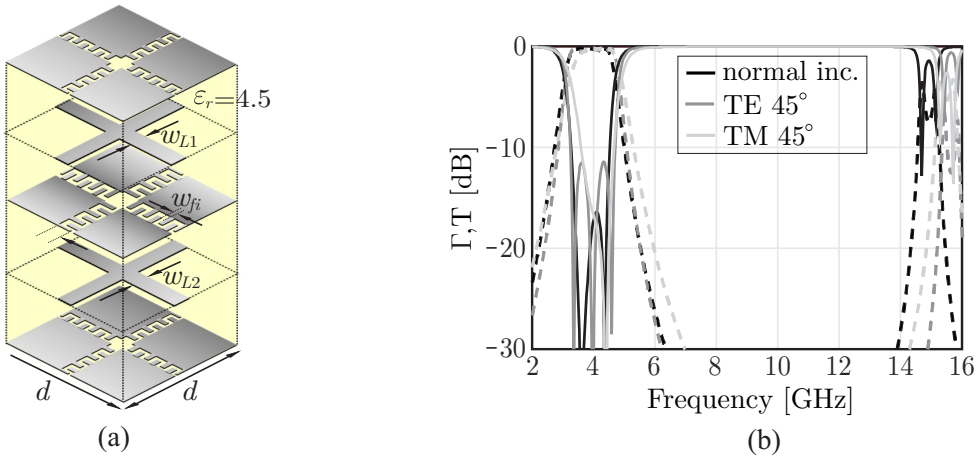

Figure 2.3: (a) FSS unit cell representing the equivalent circuit of Fig. 2.2(c) and (b) reflection (solid line) and transmission (dashed line) coefficients of the FSS for broadside, 45° TE and TM oblique incidence.

$$C = 2\varepsilon_0\varepsilon_r \sum_{m\neq 0} \frac{|\operatorname{sinc}(k_m w_c/2)|^2}{|k_m|} \tag{2.2}$$

$$L = \frac{\mu_0\mu_r}{2} \sum_{m\neq 0} \frac{|\operatorname{sinc}(k_m w_L/2)|^2}{|k_m|} \tag{2.3}$$

where ε_r and μ_r are the relative permittivity and permeability of the medium hosting the layer, w_c and w_L represent the gap between patches and the width of the inductive strips, respectively, $k_m \approx (2\pi m)/d$ and d the period of the structure. To ensure the accuracy of the expressions in (2.2) and (2.3), we enforce the FSS period to be comparable to the inter-layer distance. Smaller distance-to-period ratios would result in higher reactive coupling between layers due to higher-order Floquet waves, so that (2.2) and (2.3) are no longer valid.

It should be noted that (2.2) is valid for square patches. However, in this design the capacitance values are higher than what can be achieved with simple straight gaps between patches taking into account the manufacturing constraints. Therefore, interdigital capacitances were implemented (see Fig. 2.3(a)) and optimized with the aid of commercial electromagnetic solvers.

The unit cell period is $d = 4.2$ mm, equivalent to $\lambda_0/18$, where λ_0 is the wavelength at 4 GHz. The geometrical parameters for the capacitive and inductive layers of the FSS unit cell are presented in Table 2.3. The metal layers are separated by dielectric spacers of permittivity $\varepsilon_r = 4.5$ and thickness $h_{diel} = 3.175$ mm. The overall height of the structure

Table 2.3: Geometrical Parameter (in mm) of the FSS Unit cell

w_{fi}	l_{f1}	l_{f2}	l_{f3}	w_{L1}	w_{L2}	d	h_{diel}
0.15	0.46	0.92	0.46	0.17	0.17	4.2	3.175

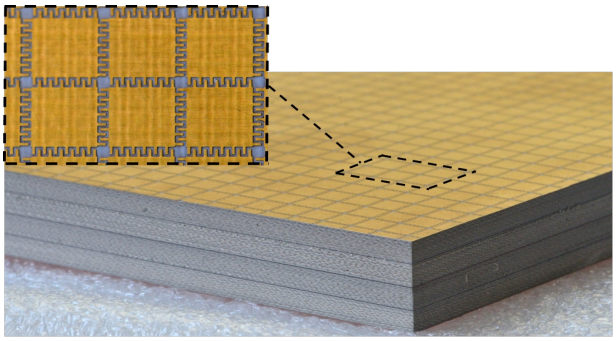

Figure 2.4: Photograph of the manufactured FSS.

is $\lambda_0/6$. The minimum gap width in the interdigitated capacitances is kept as 0.15 mm, which is compatible with standard printed circuit board (PCB) technology.
Figure 2.3(b) shows the simulated reflection (Γ) and transmission (T) coefficients for normal incidence and for transverse electric (TE) and transverse magnetic (TM) oblique incidence at 45°. It can be noted that the reflection coefficient is lower than -10 dB, (corresponding to a transmission higher than -0.5 dB) over a bandwidth of about 23% centered at 4 GHz. The higher order harmonics are rejected up to 14.3 GHz, with transmission coefficient below -20 dB.

2.2 Analysis of the Prototype of a Frequency Selective Surface

The designed FSS has been manufactured and a photo of the prototype is shown in Fig. 2.4. The overall dimensions of the fabricated panel are 445.2×400 mm^2. The metal layers are made of 18 µm-thick copper. The dielectric material is Nelco 9450, with relative permittivity $\varepsilon_r = 4.5$, dissipation factor of $\tan\delta = 0.003$ and thickness 3.175 mm. The material used for the bonding layers is Arlon Cuclad 6250, with a thickness of 38.1 µm and relative permittivity of $\varepsilon_r = 2.32$.
With respect to the measurements of the reflection coefficient, the FSS is located in the far field of a transmitting horn antenna, and the specular reflection is measured at different

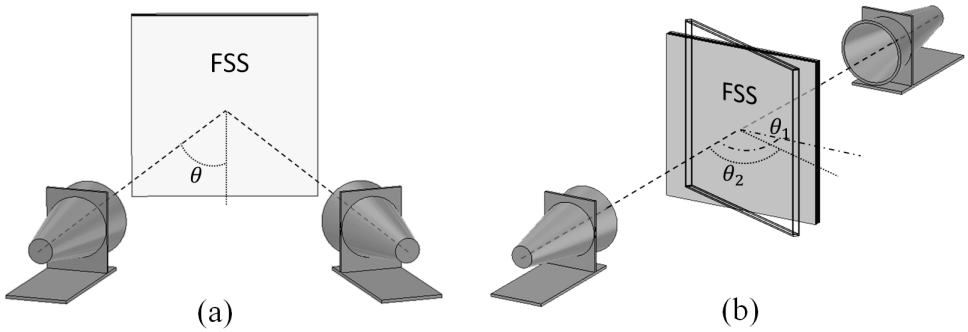

Figure 2.5: Drawing of the measurements setup for (a) reflection and (b) transmission coefficients.

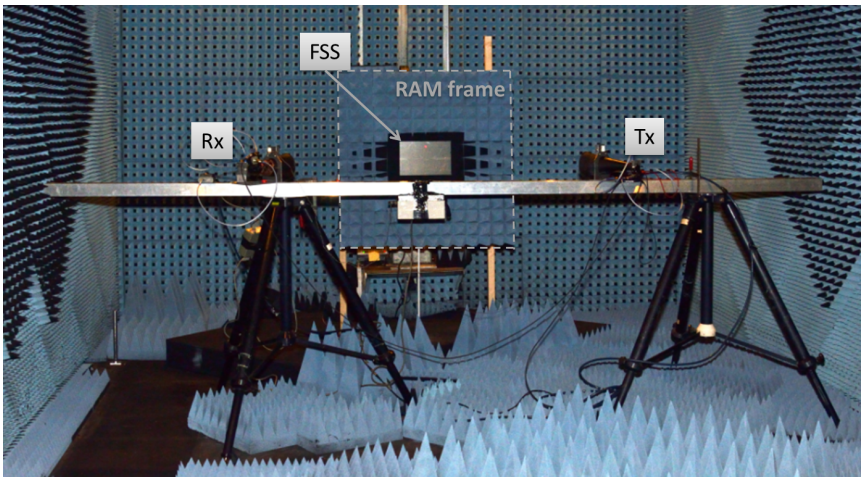

Figure 2.6: Reflection coefficient measurement setup in TNO's anechoic chamber.

angles by a receiving horn also in the far field (see Fig. 2.5(a)). The reflected power is then normalized to the power reflected by a metal plate with the same dimensions of the FSS. For the transmission coefficient, the two horns are aligned in the direction of maximum gain and the FSS is placed in the middle (see Fig. 2.5(b)), with different orientations. The transmitted power in the presence of the FSS is then normalized by the power measured in absence of the FSS. Reflection and transmission coefficients of the manufactured FSS were measured in TNO's anechoic chamber. A picture of the setup used for measuring the reflection coefficient is depicted in Fig. 2.6. The FSS was mounted with a radiation absorbent material (RAM) window such to shield it from the supporting frame.

The reflection and transmission coefficient for broadside, TE and TM oblique incidence at 45° are shown in Fig. 2.7, comparing CST simulations with measurements. The thickness of the metal and bonding layers are also included in the simulations. It can be noted that the measured results are shifted by 10% towards higher frequency and the bandwidth is

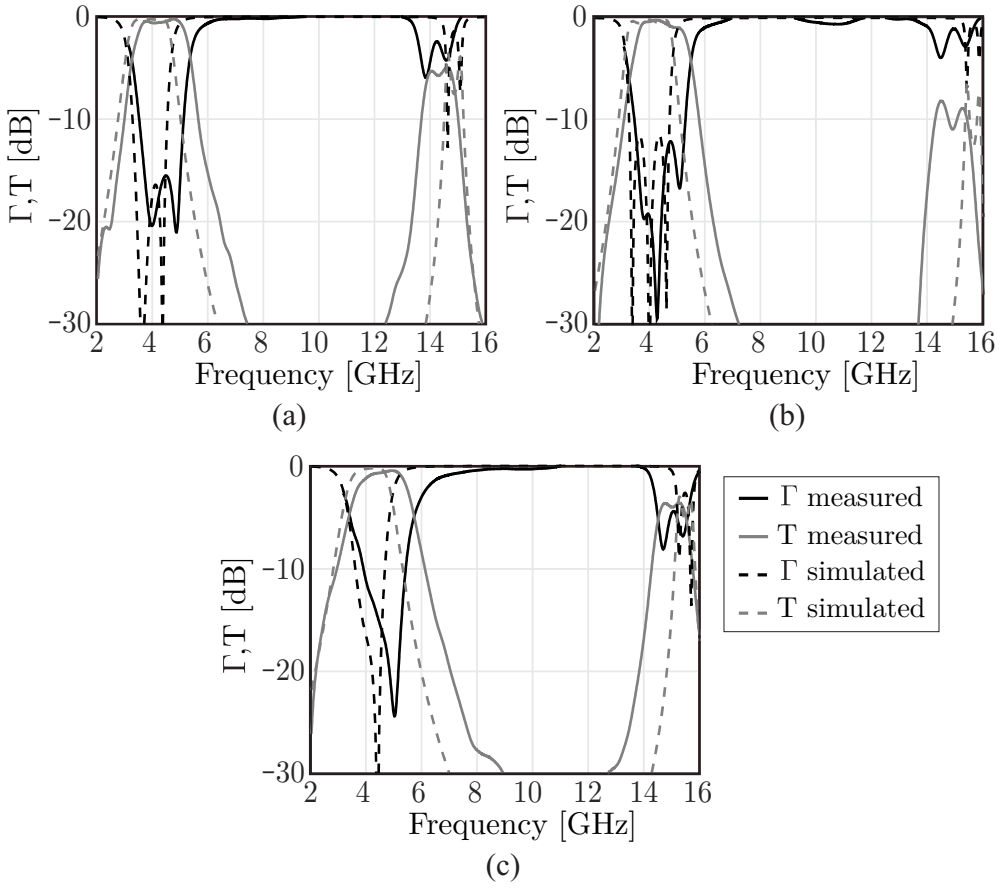

Figure 2.7: Comparison between simulated and measured Γ and T of the FSS for (a) normal, (b) TE 45° and (c) TM 45° plane-wave incidence.

enlarged compared to the simulations. The measured response is characterized by a central frequency of $f_0 = 4.5$ GHz and 27% bandwidth. Moreover, the position of the higher order harmonic is shifted towards lower frequencies, at 13.7 GHz, but still above 3_0.
It should be also mentioned that the values of the measured reflection coefficient slightly exceed unity at some frequencies, within the FSS rejection band. This is due to inaccuracies of the measurement setup in terms of alignment, exact positioning of the FSS and the metal plate, as well as reflections from the supporting structures utilized for the FSS, the metal plate and the horns.

2.2.1 Tolerance Study

To explain the discrepancy observed between measurements and predictions, an analysis of the manufacturing tolerances is carried out. The study is based on expected tolerances,

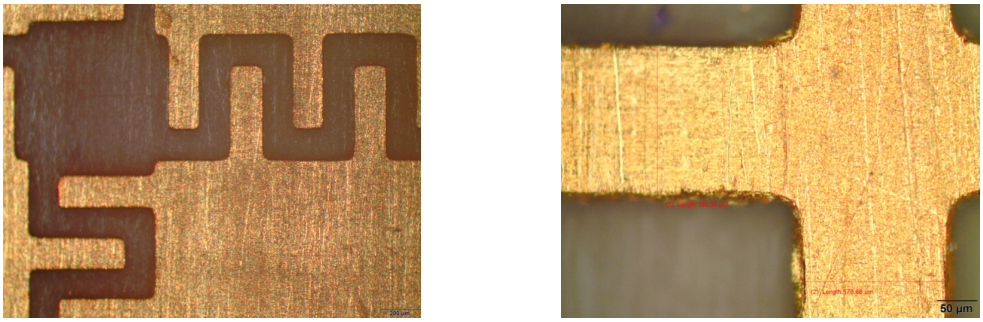

(a) (b)

Figure 2.8: Micrograph of the (a) capacitive and (b) inductive layers.

as specified by the PCB manufacturer, as well as on inspections of the actual geometrical dimensions performed with a microscope. Micrographs of some details of the fabricated layers are shown in Fig. 2.8. The widths of the slots and the metal strips were measured in several areas of the FSS, as well as the metal thickness (through a Dektak surface profiler). It was found that the variations of design parameters are within the following intervals: ± 2 µm for the metal thickness and ± 20 µm for the widths of slots and metal strips. Additional variations of the thickness of the dielectric slabs (± 100 µm) and of their relative dielectric permittivity (± 0.1) were considered.
The results of the parametric investigation using the commercial EM solver [65] are summarized in Fig. 2.9, which shows a group of simulated curves, obtained with different combinations of the varying parameters. The simulations including the tolerance explain the frequency shift observed in the measurements. Slightly lower values of Γ and slower roll off are observed around 6 GHz for TM incidence at 45°, compared to simulations. This might due to additional losses (e.g. from the absorbing material used to create a window in front of the FSS) and to the previously mentioned inaccuracies of the normalization procedure for Γ.
Moreover, the effect of each parameter has been investigated individually. The findings of this analysis can be summarized as follows:

- the width of the interdigital capacitance is the most sensitive parameter and is responsible for the shift in frequency of the FSS bandwidth;
- the thickness variations of the dielectric slabs are largely responsible for the shift in frequency of the spurious harmonic;
- the enlargement of the bandwidth is primarily caused by the variation of the track width in the inductive layer.

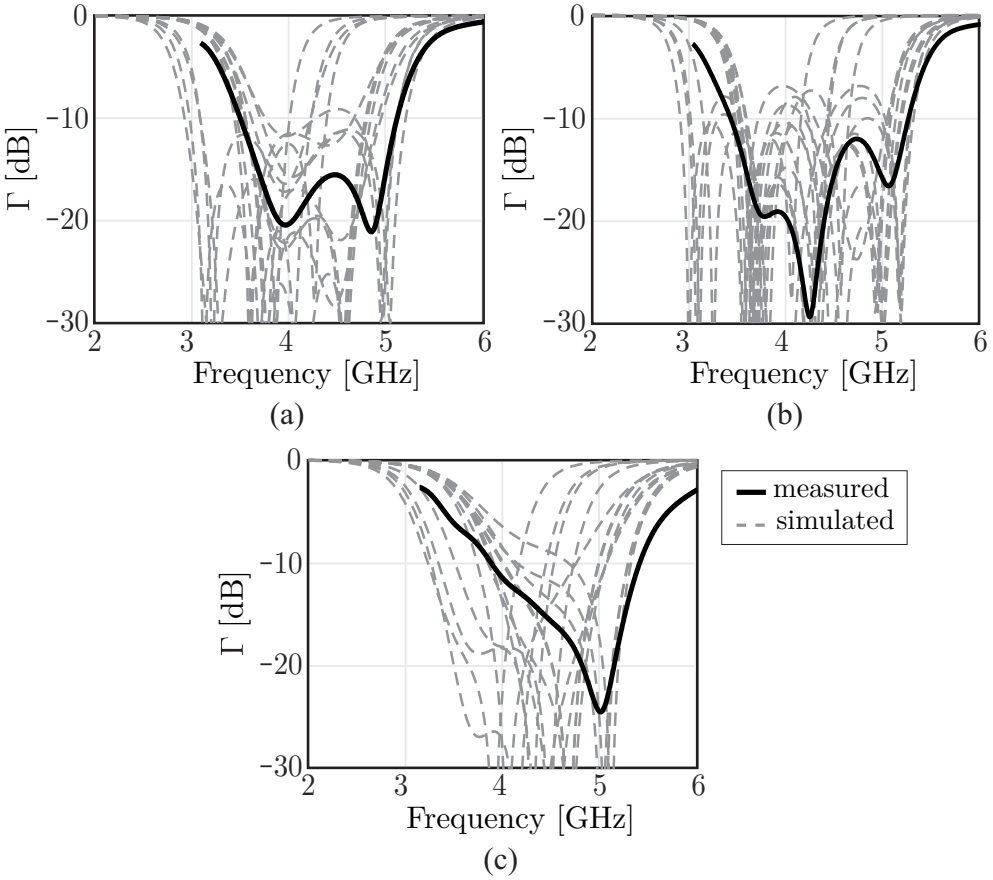

Figure 2.9: Variation of the reflection coefficient (Γ) of the FSS when manufacturing tolerances are included for: (a) normal, (b) TE 45° and (c) TM 45° plane-wave incidence.

2.3 Performance of the FSS in Combination with a Connected Array of Dipoles

The objective of this section is to analyze the performance of the MEFSS in the presence of a phased array antenna. To this aim, the connected array prototype developed in [60] is used. This antenna array is composed of 7×7 elements and can scan within a $\pm 45°$ range for every azimuth angle over the frequency band 3 to 5 GHz. One of the benefits of using connected arrays is that the antenna impedance is stable over a large frequency range, including the FSS bandwidth, so that the antenna represents a constant loading for the FSS within the operating bandwidth [66].

A dispersion analysis is carried out to determine at what distance from the array the FSS should be located to avoid the occurrence of surface waves within the bandwidth of operation.

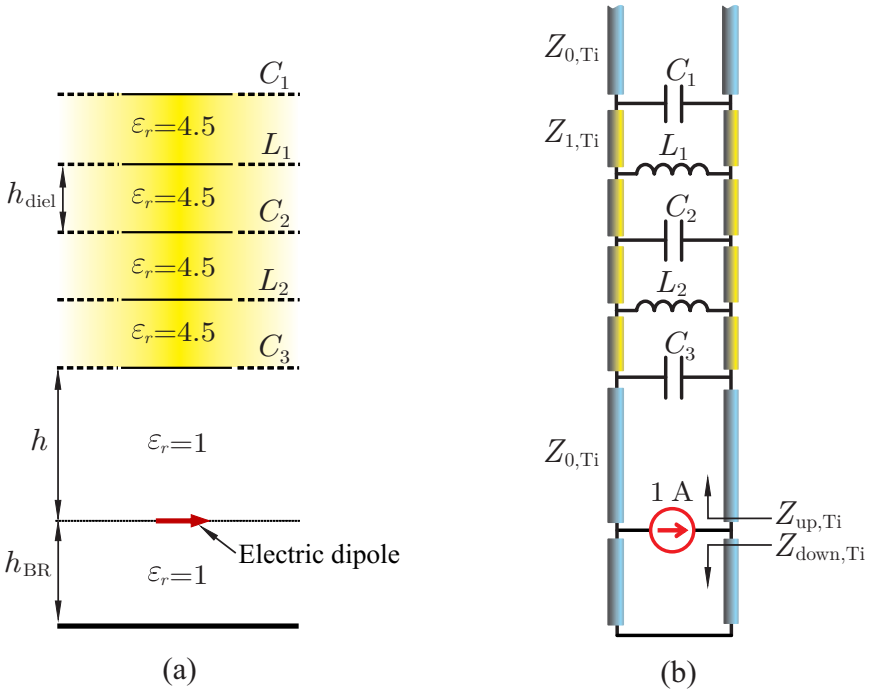

Figure 2.10: (a) Geometry and (b) transmission line model used to calculate modes propagating within the stratification.

2.3.1 Dispersion Analysis

To investigate the modes propagating within the layered medium, we consider the simplified geometry in Fig. 2.10(a): this represents an elementary electric dipole located at distance h from the FSS and at distance h_{BR} from a backing reflector, fixed to 18.9 mm as in [60]. The spectral Green's function can be related to the voltage and current solutions of the transmission line shown in Fig. 2.10(b), for the TE and TM modes. The characteristic impedances of the transmission lines are $Z_{n,\text{TE}} = \zeta_n k_n / k_{zn}$ and $Z_{n,\text{TM}} = \zeta_n k_{zn} / k_n$ for the TE and TM modes, respectively, where the subscript n is 0 for free space and 1 for the dielectric, ζ_n and k_n are the medium impedance and the wavenumber of the corresponding material, and $k_{zn} = (k_n^2 - k_\rho^2)^{1/2}$. The elementary dipole is represented by a shunt current source with unit amplitude.

The propagating surface wave modes can be found by solving the following dispersion equation:

$$D(k_\rho) = Z_{\text{up,Ti}}(k_\rho) + Z_{\text{down,Ti}}(k_\rho) = 0 \tag{2.4}$$

where the impedances $Z_{\text{up,Ti}}$ and $Z_{\text{down,Ti}}$ are defined as in Fig. 2.10(b), and the subscript Ti can refer to either TE or TM. The zeros of the equation (2.4) are found numerically with an iterative Newton method. The resulting TM and TE surface waves poles are shown in

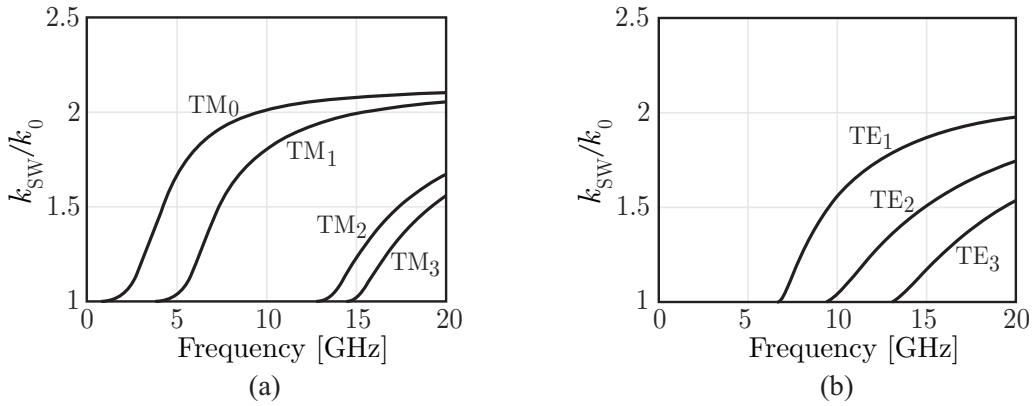

Figure 2.11: Dispersion diagram of the surface wave poles for (a) TM modes and (b) TE modes.

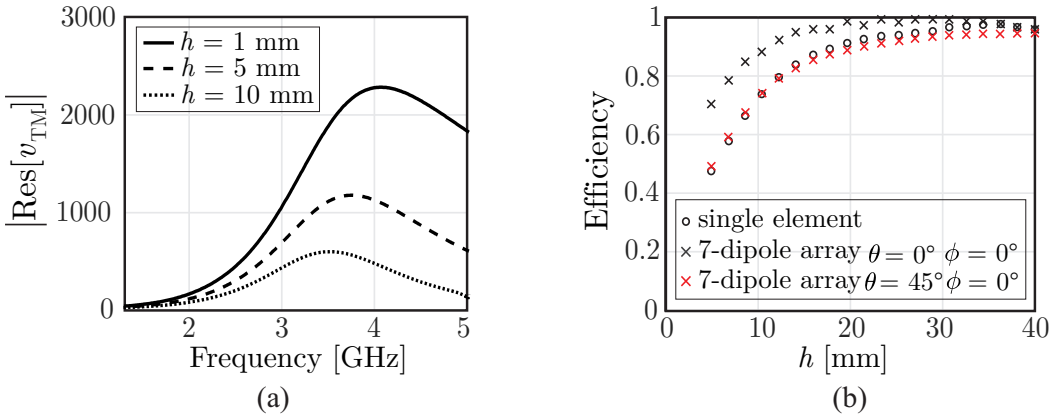

Figure 2.12: (a) Residue correspondent to the TM_0 mode for different distances and (b) simulated radiation efficiency of a single short dipole and an array of 7 short dipoles in the presence of the stratification in Fig. 2.10(a), as a function of the distance h.

the dispersion diagram in Fig. 2.11, as a function of the frequency.

By restricting the observation to the range 3 to 5 GHz, in which the antenna array operates, there is only one dominant TM surface wave. We observed that the position of this polar singularity is not dependent on the distance h, as it is related to propagation in the dielectric. However, the residue associated with the pole varies with the distance, thus the amount of power carried by this wave can change. To clarify this aspect, Fig. 2.12(a) shows the residue of the voltage v_{TM} at the generator $Res[v_{\mathrm{TM}}] = N(k_{\mathrm{SW}})/D'(k_{\mathrm{SW}})$ for different values of h, where $N(k_\rho) = Z_{\mathrm{up,TM}}(k_\rho) \times Z_{\mathrm{down,TM}}(k_\rho)$ and D' represent the derivative of the function in (2.4). The simulated radiation efficiency of a short dipole in the presence of the FSS was also simulated with CST microwave studio and reported in Fig. 2.12(b) at 4 GHz, as a function of the distance h. Also the efficiency of a linear array of 7 collinear short dipoles scanning at broadside is shown, resulting in a higher efficiency.

However, when the array scans in the direction of the surface wave mode ($\theta = 45°$ $\phi = 0°$) the efficiency is reduced. The plotted efficiency is defined as $P_{\text{rad}}/(P_{\text{rad}} + P_{\text{SW}})$, where P_{rad} is the total power radiated to free space and P_{SW} is the power launched into surface waves. From Fig. 2.12(b), it can be observed that the efficiency increases with the distance h and remains above 90% for all distances in the range of 12.5 to 40 mm for broadside, and in the range of 23.5 to 40 mm scanning at $\theta = 45°$ $\phi = 0°$.
Moreover, when the array of connected dipoles is considered in the presence of the layered medium, the distance should be still large enough to assume that only the fundamental Floquet mode is dominating the interaction between the dipoles and the FSS, so that reactive coupling can be neglected. For this reason, a distance of around half wavelength at 4 GHz (37.5 mm) is considered. This value corresponds to 93% efficiency for a short dipole radiating in the presence of the FSS, as can be seen in Fig. 2.12(b).

2.3.2 Matching Properties of the Combined Array/MEFSS

Figure 2.13(a) shows a three-dimensional view of the connected dipole unit cell from [60]. The dipole arms are connected to a loop structure that has the purpose of rejecting the common-mode currents. The feeding structure is then connected to a sleeve balun under the backing reflector, to implement the transition from differential to single-ended transmission line. Figure 2.13(b) displays the same dipole element cascaded with the idealized FSS located at distance $h = 37.5$ mm from the top of the dipole. The simulated values of capacitive and inductive layers of the FSS were modified with respect to the ones in Table 2.3, so that the simulations are representative of the measurements presented in Sect. 2.2.1. The connected array prototype developed in [60] is used to experimentally evaluate the effects of the MEFSS in proximity of an array. Photographs of both structures combined are shown in Fig. 2.14.
In Fig. 2.15, the simulated and measured active voltage standing wave ratio (VSWR) of the standalone connected-dipole array and the combination of the array with the FSS are shown, for broadside and scanning up to 45° in the E-plane and H-plane. The bandwidth defined as VSWR$<$ 3 is highlighted in all the figures. By comparing the two simulated results (Figs.2.15(a) and (b)), it is evident that the presence of the FSS reduces the bandwidth of the antenna from 4 to 5 GHz, while keeping good levels of matching. Narrow resonances occur between 5 and 5.5 GHz also in the presence of the FSS. However, these resonances are mainly due to the limited bandwidth of the dipole feed structure. Outside the range 3 to 5 GHz, the feeding lines of the dipoles do not exhibit good matching characteristics and the common-mode rejection structure is no longer effective. Similar effects

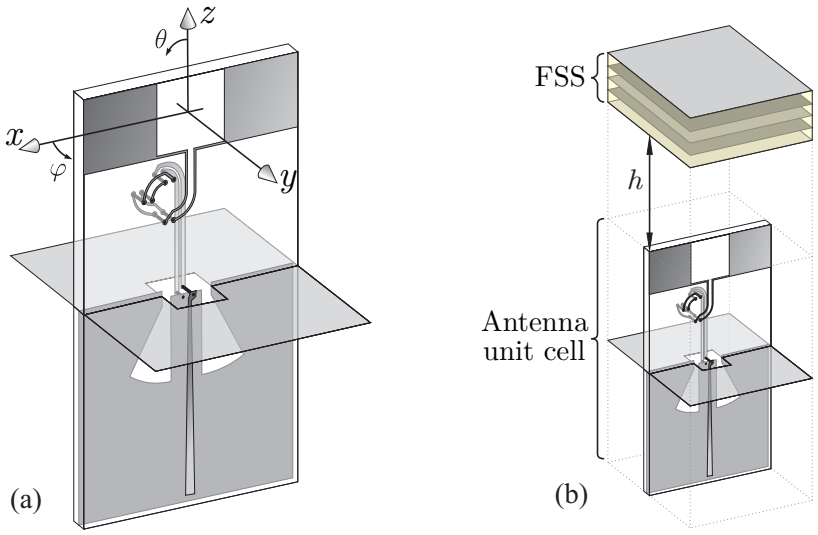

Figure 2.13: (a) Connected dipole unit cell and (b) 3D view of the MEFSS and the connected dipole array combined.

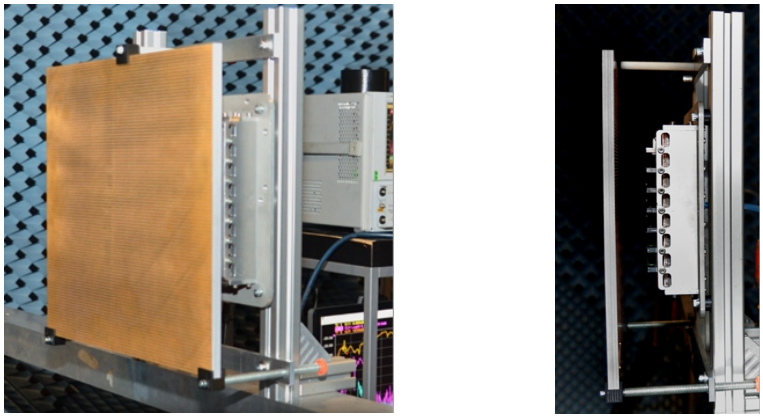

Figure 2.14: Photographs of the manufactured MEFSS in combination with the connected array of dipoles: (a) front and (b) side view.

can be observed from the measured results in Fig. 2.15(c) and (d). The presence of the FSS reduces the bandwidth, compared with the array alone. It can be noted that measured upper limits of the bandwidth are lower than the simulated ones, with and without the FSS. This effect is due to a mismatch of the SMA connector transition for frequency above 4.5 GHz, which is not accounted for in the simulations.

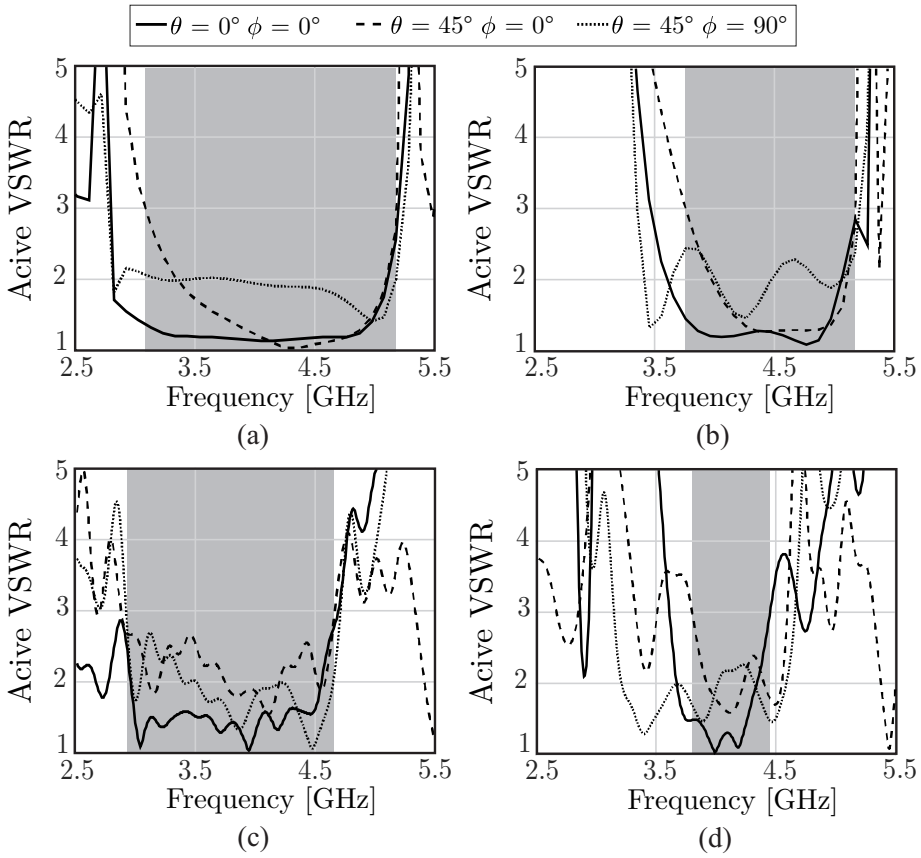

Figure 2.15: Simulated Active VSWR of (a) the array alone and (b) the dipole with the FSS, and measured Active VSWR of (c) the array and (d) in combination with the FSS.

2.3.3 Gain and Patterns of the Combined Array/MEFSS

The transmission coefficients between a horn located in the far field and the central element of the connected array have been measured, with and without the FSS. The active element gain, normalized to the maximum directivity of the unit cell aperture ($4\pi A/\lambda^2$), is plotted in Fig. 2.16 for broadside radiation and for scanning at 45° in the E- and H-plane. It can be appreciated that, within the operational bandwidth of the FSS (highlighted in the figure), the element gain with the FSS is very close to that of the antenna alone. In the frequency range from 6 to 18 GHz, the gain of the antenna with the FSS is 17 dB lower for broadside and for scanning up to 45° in the two main planes.

Oscillations of around 2-3 dB are observed within the FSS pass band and they are mainly due to truncation effects of the finite array. Indeed, the period of these fluctuations can be related to the distance between the measured element and the edges of the array. Time gating with narrower windows would eliminate the oscillations, however this was not

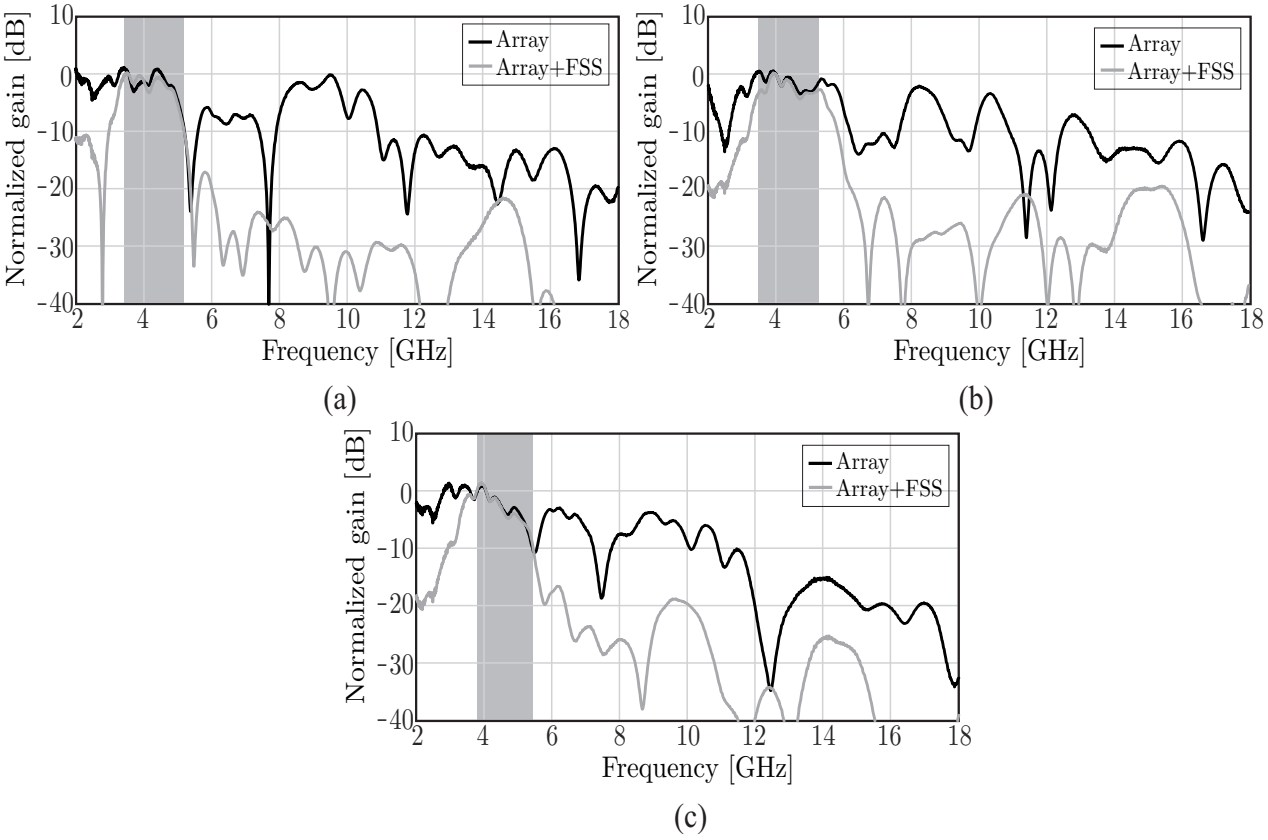

Figure 2.16: Measured active element gain normalized by the ideal directivity of the unit cell aperture, with and without the FSS for (a) broadside, (b) E- and (c) H-plane at 45°.

applied to account for the multiple reflections that might occur between the FSS and the array.

In addition, the measured normalized active element patterns in the E- and H-planes for the case of the antenna alone and in combination with the FSS are shown in Fig. 2.17. Both co-polar and cross-polar components are shown at the frequency of 4 GHz. The normalized co-pol for the antenna alone and in combination with the FSS are similar between $-45°$ and 45°, angles where the FSS is working. The normalized X-pol pattern is below -15 dB in the E-plane and -18 dB in the H-plane for both configurations. Measurements for the D-plane were not possible due to supporting structure limitations. Nevertheless, the X-pol level for $\phi = 45°$ and $\theta = 45°$ was simulated (see Fig. 2.18), being lower than -10 dB within the FSS bandwidth.

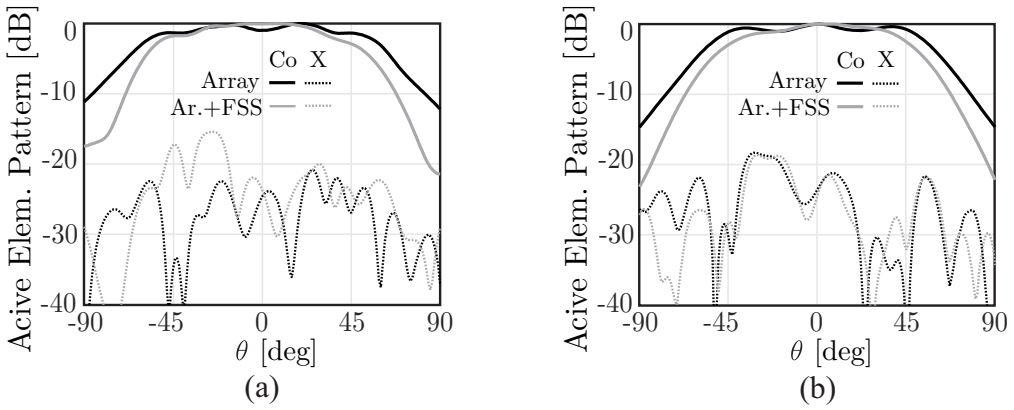

Figure 2.17: Co-polar (Co) and Cross-polar (X) measured normalized active element patterns in the (a) E- and (b) H-plane at 4 GHz.

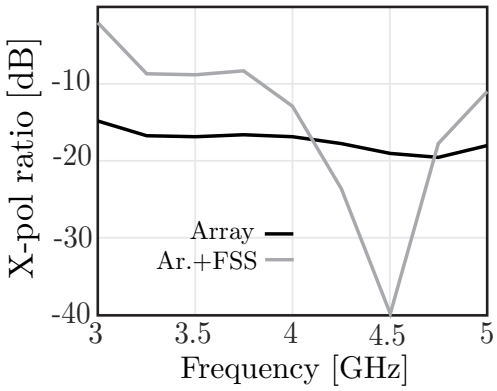

Figure 2.18: Simulated X-pol ratio for the array when scanning to $\theta = 45°$ and $\phi = 45°$, with and without the FSS.

2.4 Conclusions

A miniaturized-element frequency selective surface was designed, fabricated and tested. Measured results showed a bandwidth of 27% around the central frequency of 4.5 GHz. The unit cell size has dimensions of 4.2×4.2 mm^2 and a total height of $\lambda_0/5.2$, where λ_0 is the wavelength at 4.5 GHz. A large rejection of higher order harmonics is achieved with the first harmonic at the frequency of 13.7 GHz, with a transmission coefficient lower than -20 dB.

To investigate the interaction with wide-band antennas with a wide scanning range, the MEFSS was combined with a connected dipole array antenna. The minimum distance between the antenna and the FSS for which no resonances or surface waves propagation occur was investigated through a dispersion analysis. When combining both structures it can be appreciated that the response within the FSS passband agrees well with the

one of the antenna alone, while a broadband out-of-band rejection, better than 17 dB, is measured from 6 to 18 GHz and for scanning up to 45° in the main planes. The FSS is therefore effective in rejecting out-of-band sources of interference over a broad frequency range. Measured active element patterns for E- and H-plane show a slight decrease in beamwidth when the FSS is included.

Chapter 3

Angular Filtering Array: Theory

In this chapter, antenna arrays with tilted dipoles are investigated in terms of radiation and impedance properties. A spectral method of moments (MoM) is developed for the analysis of infinite arrays with arbitrarily tilted dipole elements, in free space or in the presence of a backing reflector. With the aid of this analysis method, the radiation characteristics of arrays of stacked dipoles over a ground plane are studied, explaining the variation of the patterns as a function of the inter-element distance and the angle of inclination of the elements. Finite linear arrays of tilted dipoles are also investigated, to asses the dependence of the array characteristics on the number of elements. The developed method can be used to design arrays with non-symmetric radiation patterns for angular filtering or pattern shaping.

3.1 Periodic MoM for an Array of Skewed Dipoles in Free Space

To investigate the radiation properties of arrays of tilted elements, a periodic MoM solution is derived. For the sake of simplicity, we first consider an array of tilted strip dipoles in free space, as shown in Fig. 3.1. The dipoles are assumed to be tilted by an angle α with respect to the x-axis and excited with a delta-gap source. Although the derivation is described for elements in free space, a similar procedure can be also used to describe dipoles in the presence of a backing reflector and stacked dipole elements.

By applying the equivalence principle, unknown equivalent current densities radiating in free space can be defined on the dipole surface. The total current density for the infinite

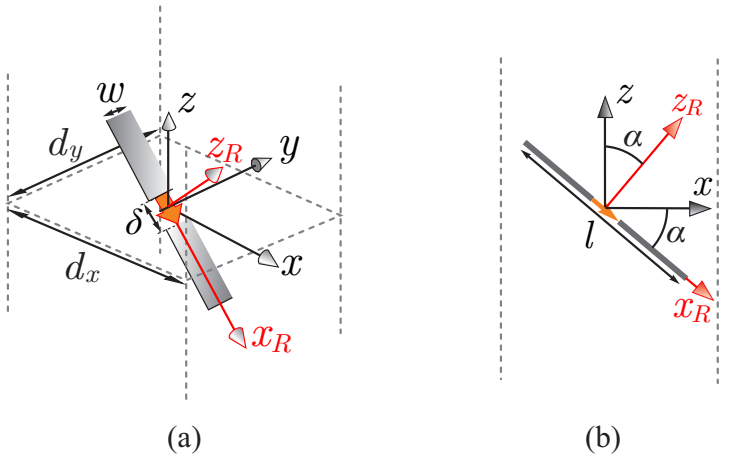

Figure 3.1: Unit cell of an infinite array of tilted dipoles in free space with the original and rotated reference systems: (a) three-dimensional view and (b) side view.

array can be written as a sum of doubly-periodic contributions:

$$\boldsymbol{j}_\infty(x,y,z) = \sum_{n_x=-\infty}^{\infty} \sum_{n_y=-\infty}^{\infty} \boldsymbol{j}(x-n_x d_x, y-n_y d_y, z) e^{-jk_{x0}n_x d_x} e^{-jk_{y0}n_y d_y} \tag{3.1}$$

where $k_{x0} = k_0 \sin\theta\cos\phi$ and $k_{y0} = k_0 \sin\theta \sin\phi$ are the x- and y-components of the wave vector associated with the scanning directions θ and ϕ, and k_0 is the free-space wavenumber at the calculation frequency.

The currents must satisfy the boundary conditions for the total electric field on the dipoles. The tangential electric field vanishes on the metal ($\hat{\boldsymbol{z}}_R \times \boldsymbol{e}_{\text{tot}} = 0$), which is assumed to be perfect electric conductor. In the feeding gaps, the field is related to the current by the impedance boundary conditions ($\hat{\boldsymbol{z}}_R \times \boldsymbol{e}_{\text{tot}} = Z_l \boldsymbol{j}$), where Z_l is an equivalent surface impedance related to the generator impedance of the feeds. Defining the function $\text{rect}_{\text{gap}}(\boldsymbol{r})$ to be 1 in the gap regions and zero elsewhere, we can write the electric field integral equation as:

$$-\boldsymbol{e}_{\text{scat}}(\boldsymbol{r}) + Z_l \boldsymbol{j}(\boldsymbol{r}) \text{rect}_{\text{gap}}(\boldsymbol{r}) = \boldsymbol{e}_{\text{inc}}(\boldsymbol{r}) \tag{3.2}$$

where we introduced the incident electric field $\boldsymbol{e}_{\text{inc}} = (V_0/\delta)\text{rect}_{\text{gap}}(\boldsymbol{r})$. The scattered field can be written in the space domain as a convolution integral:

$$\boldsymbol{e}_{\text{scat}}(\boldsymbol{r}) = \iiint_V \boldsymbol{j}_\infty(\boldsymbol{r}')\boldsymbol{g}(\boldsymbol{r},\boldsymbol{r}')d\boldsymbol{r}' \tag{3.3}$$

where $\boldsymbol{g}$ is the free-space dyadic Green's function, relating the electric field to the electric source, V is an infinite volume containing the entire dipole array, and $\boldsymbol{r} \equiv (x,y,z)$, $\boldsymbol{r}' \equiv (x',y',z')$ are the observation and source points, respectively.

The scattered field can be also evaluated in the spectral domain, in terms of a double Floquet modal expansion in x and y and an inverse Fourier integral for the z-variable:

$$\boldsymbol{e}_{\text{scat}}(\boldsymbol{r}) = \frac{1}{2\pi}\frac{1}{d_x d_y}\int_{-\infty}^{\infty}\sum_{m_x=-\infty}^{\infty}\sum_{m_y=-\infty}^{\infty}\boldsymbol{J}(k_{xm},k_{ym},k_z) \boldsymbol{G}(k_{xm},k_{ym},k_z)e^{-jk_{xm}x}e^{-jk_{ym}y}e^{-jk_z z}dk_z \quad (3.4)$$

where $\boldsymbol{J}$ is the three-dimensional Fourier transform of the current distribution in the unit cell with indexes $n_x = 0$ and $n_y = 0$, and $\boldsymbol{G}$ is the spectral dyadic Green's function, given in (B.4). The Floquet wavenumbers are $k_{xm} = k_{x0} - 2\pi m_x/d_x$ and $k_{ym} = k_{y0} - 2\pi m_y/d_y$, and k_z is the spectral counterpart of the spatial variable z.
The current density on the dipole centered in the origin is assumed to be described as a single entire-domain basis function:

$$j(x_R, y_R, z_R)\hat{\boldsymbol{x}}_R = i_0 b_l(x_R)e(y_R)\delta(z_R)\hat{\boldsymbol{x}}_R \quad (3.5)$$

where we applied the separation of variables and we considered the rotated $(x_R y_R z_R)$-reference system, defined in Fig. 3.1. The axis x_R and z_R are rotated by α with respect to x and z respectively, while the coordinate y_R is coincident with y. The coefficient i_0 is an unknown weight for the current profile and $\hat{\boldsymbol{x}}_R$ is the unit vector aligned with the dipole axis. The chosen basis function comprises a longitudinal piece-wise sinusoidal distribution $b_l(x_R)$ [67–69], an edge-singular transverse profile $e(y_R)$ and a Dirac delta function $\delta(z_R)$, since the dipole thickness is assumed to be infinitesimal. The explicit expression of the sinusoidal basis function is given by

$$b_l(x_R) = \frac{\sin(k_0(l/2 - |x_R|))}{\sin(k_0 l/2)} \quad (3.6)$$

where l indicates the dipole length, The edge-singular transverse profile [70] is written as

$$e(y_R) = \frac{2}{\pi w}\left(1 - \frac{2y_R}{w}\right)^{-1/2} \quad (3.7)$$

where w is the width of the dipole, and a Dirac delta function. To express the current in the (xyz)-reference system (see Fig. 3.1), an axis transformation is needed and it can be written as follows

$$\begin{aligned} x_R &= x\cos\alpha - z\sin\alpha \\ z_R &= x\sin\alpha + z\cos\alpha \end{aligned} \quad (3.8)$$

so that the current distribution can be expressed as

$$j(x,y,z) = i_0 b_l(x\cos\alpha - z\sin\alpha)e(y)\delta(x\sin\alpha + z\cos\alpha)\,. \tag{3.9}$$

As shown in Appendix A, the three-dimensional Fourier transform of the current can be derived as

$$J(k_x,k_y,k_z) = i_0 J_0(k_y w/2)B_l(k_x\cos\alpha - k_z\sin\alpha) \tag{3.10}$$

where J_0 is the Bessel function of zeroth order, representing the Fourier transform of the edge singular distribution and B_l is the Fourier transform of the sinusoidal profile, given by

$$B_l(k) = \frac{2k_0(\cos(kl/2) - \cos(k_0 l/2))}{(k_0^2 - k^2)\sin(k_0 l/2)}\,. \tag{3.11}$$

By applying the Galerkin method [71], we can define the active input impedance of the dipole as the projection (indicated as $\langle\cdot,\cdot\rangle$) of the field scattered by the basis function onto a test function, $\boldsymbol{t}$, chosen as equal to the basis function

$$Z_{\text{in}} = \frac{-\langle\hat{\boldsymbol{z}}_R \times \boldsymbol{e}_{\text{scat}}(\boldsymbol{r}), \boldsymbol{t}(\boldsymbol{r})\rangle}{i_0}\,. \tag{3.12}$$

By substituting (3.4) in (3.12), after some algebraic steps, the input impedance can be expressed in the spectral domain, for dipoles in free space, as follows:

$$Z_{\text{in,fs}} = \frac{-1}{2\pi d_x d_y}\sum_{m_x=-\infty}^{\infty}\sum_{m_y=-\infty}^{\infty} J_0^2\Big(\frac{k_{ym}w}{2}\Big) \int_{-\infty}^{\infty} B_l(k_{x_R})B_l(-k_{x_R})G_{x_Rx_R}(k_{xm},k_{ym},k_z)dk_z \tag{3.13}$$

where $k_{x_R} = k_{xm}\cos\alpha - k_z\sin\alpha$ and the Green's function $G_{x_Rx_R}$ is related to xx-, xz-, and zz-components of the free-space dyadic Green's function by

$$G_{x_Rx_R} = G_{xx}\cos^2\alpha - 2G_{xz}\sin\alpha\cos\alpha + G_{zz}\sin^2\alpha\,. \tag{3.14}$$

With the chosen sinusoidal basis function to represent the current on the dipole, the integrand in (3.13) can be written explicitly in closed form. The resulting expression presents a number of polar singularities, thus the integral can be solved analytically using the residue theorem, following the steps described in Appendix B.1.

For small electrical dimensions of the delta gap, the unknown coefficient i_0 can be found as $i_0 = V_0/(Z_l + Z_{\text{in}})$. Once the current i_0 is found we can calculate the radiation pattern, by

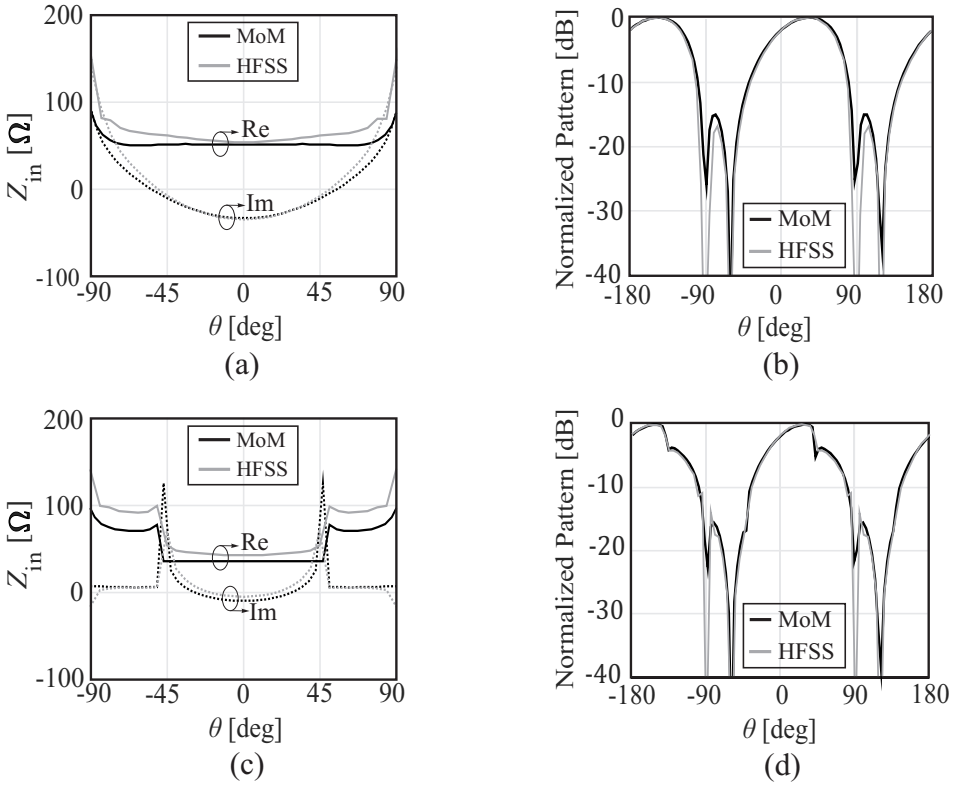

Figure 3.2: Active input impedance for an infinite array of dipoles in free space with a spacing between elements of (a) 0.5λ and (c) 0.6λ; E-plane active element pattern for (b) 0.5λ and (d) 0.6λ. The dipoles are tilted 30° and results of the MoM are compared with HFSS.

evaluating the expression in (3.4) only in the fundamental Floquet mode and calculating the integral in k_z with the residue theorem in the pole $k_{zm} = (k_0^2 - k_{xm}^2 - k_{ym}^2)^{1/2}$:

$$\boldsymbol{e}(\boldsymbol{r}) = \frac{jk_{z0}}{d_x d_y} \frac{e^{-jk_0 r}}{2\pi r} \boldsymbol{J}(k_{x0}, k_{y0}, k_{z0}) \boldsymbol{G}_{2D}(k_{x0}, k_{y0}) \tag{3.15}$$

where $\boldsymbol{G}_{2D}(k_x, k_y)$ is the two-dimensional spectral dyadic Green's function in free space expressed as

$$\boldsymbol{G}_{2D}(k_x, k_y) = -\frac{\zeta}{2k_0} \frac{k_0^2 - k_x^2}{\sqrt{k_0^2 - k_x^2 - k_y^2}} \tag{3.16}$$

As a numerical example, we consider an array of dipoles of length $l = 0.5\lambda$, width $w = 0.1\lambda$, rotated by $\alpha = 30°$. The port impedance is set to $Z_l = 50\ \Omega$. The active input impedance and the active element pattern in the E-plane, calculated with the proposed method, are shown in Fig. 3.2 and compared with the simulations using the commercial EM solver HFSS

[72], as a function of the scan angle. Two different periods are considered, $d_x = d_y = 0.5\lambda$ and $d_x = d_y = 0.6\lambda$. The discrepancy between the MoM and HFSS in terms of impedance is mainly due to the single basis function approximation we made for the current. Such hypothesis neglects the reactance stored in the feeding gap and the possibility for more general current distributions with respect to sinusoidal. However, the approximation is sufficient to properly represent the radiation patterns (Fig. 3.2(b) and (d)).
From the results in Fig. 3.2, it can be noted that the impedance is symmetric with respect to the scan angle, regardless of the periodicity. This result is consistent with the symmetry properties demonstrated in [35] for planar currents. A proof of the symmetry condition from the explicit expressions of the impedance is given in Appendix C, where we consider currents that can have vertical components. Despite the symmetry of the impedance, the active element patterns are not symmetric with respect to the broadside direction, even for periods of 0.5λ. Therefore, tilted dipole elements in free space do not satisfy the pattern symmetry condition stated in [35]. For periodicity higher than half wavelength, discontinuities occur in the active input impedance and the active element pattern, due to grating lobes entering the visible region [73].

3.2 Dipoles with Backing Reflector and Stacked Dipole Elements

3.2.1 Array of Dipoles with Backing Reflector

We now consider tilted dipoles with their center at a distance h from a backing reflector, as depicted in Fig. 3.3(a). By applying the image theorem as in Fig. 3.3(b), the active input impedance of the dipole can be written as the summation of the self impedance and the mutual impedance with its image: $Z_{\text{in}} = Z_{\text{self}} + Z_{\text{mutual}}$, where Z_{self} coincides with $Z_{\text{in,fs}}$ in (3.13), whereas Z_{mutual} can be calculated in a similar way by including a shift $2h$ along the z-axis and an inverse tilt of the image compared to the main dipole:

$$Z_{\text{mutual}} = \frac{-1}{2\pi d_x d_y} \sum_{m_x=-\infty}^{\infty} \sum_{m_y=-\infty}^{\infty} J_0^2\Big(\frac{k_{ym} w}{2}\Big) \int_{-\infty}^{\infty} B_l(k_{x_{Ri}}) B_l(-k_{x_R}) G_{x_R x_{Ri}}(k_{xm}, k_{ym}, k_z) e^{-jk_z 2h} dk_z \quad (3.17)$$

where $k_{x_{Ri}} = k_{xm}\cos\alpha + k_z \sin\alpha$ represents a wavenumber with inverse rotation compared to k_{x_R} and $G_{x_R x_{Ri}} = -G_{xx}\cos^2\alpha + G_{zz}\sin^2\alpha$. The radiated field is the summation of the

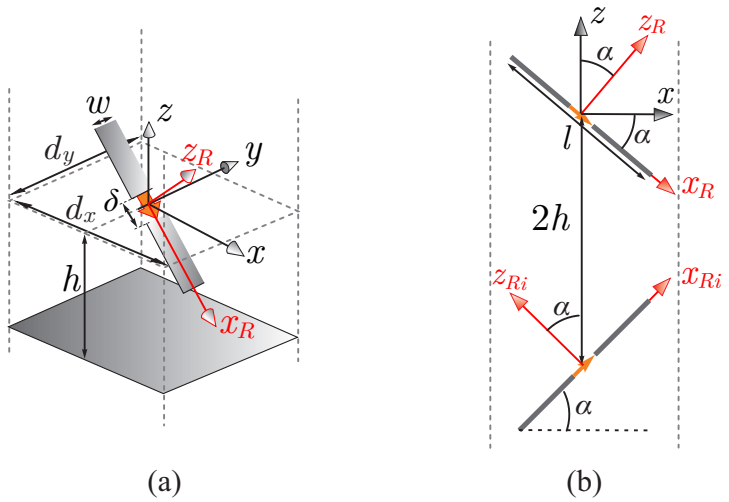

Figure 3.3: Unit cell of an infinite array of tilted dipoles in the presence of a backing reflector with the original and rotated reference systems: (a) three-dimensional view and (b) side view of the equivalent unit cell using the image theorem.

field radiated by the dipole and by its image:

$$\boldsymbol{e}(\boldsymbol{r}) = \frac{jk_{z0}}{d_x d_y}\frac{e^{-jk_0 r}}{2\pi r}\Big(\boldsymbol{J}(k_{x0},k_{y0},k_{z0}) \pm \boldsymbol{J}_{\text{image}}(k_{x0},k_{y0},k_{z0})\Big)\boldsymbol{G}(k_{x0},k_{y0}) \tag{3.18}$$

where the '+' sign refers to the z-component of the currents and the '$-$' sign refers to the x-component of the currents, as a consequence of the image theorem. The image current spectrum $\boldsymbol{J}_{\text{image}}$ is given by

$$\boldsymbol{J}_{\text{image}}(k_x,k_y,k_z) = i_0 J_0(k_y w/2) B_l(k_x\cos\alpha + k_z\sin\alpha) e^{-jk_z 2h}\hat{\boldsymbol{x}}_{Ri}\,. \tag{3.19}$$

As numerical example, we consider the same dipole geometry as in Sec. 3.1 and we set $h = 0.25\lambda$. The active input impedance and the active element pattern for an inter-element distance of 0.5λ and 0.6λ are plotted in Fig. 3.4, compared with HFSS. We can observe that the impedance is symmetric with respect to the scan angles, as for the free space case. Regardless of the inter-element distance, the active element pattern of an array of dipoles in the presence of a backing reflector is also symmetric with respect to broadside. This property can be explained with the fact that, as the dipole radiates the same power upwards and downwards, the power reflected by the ground plane is equal to the one radiated upwards, but in the specular direction. This result suggests using a more directive element to reduce the power reflected by the ground plane in the specular direction and to achieve asymmetry in the radiation.

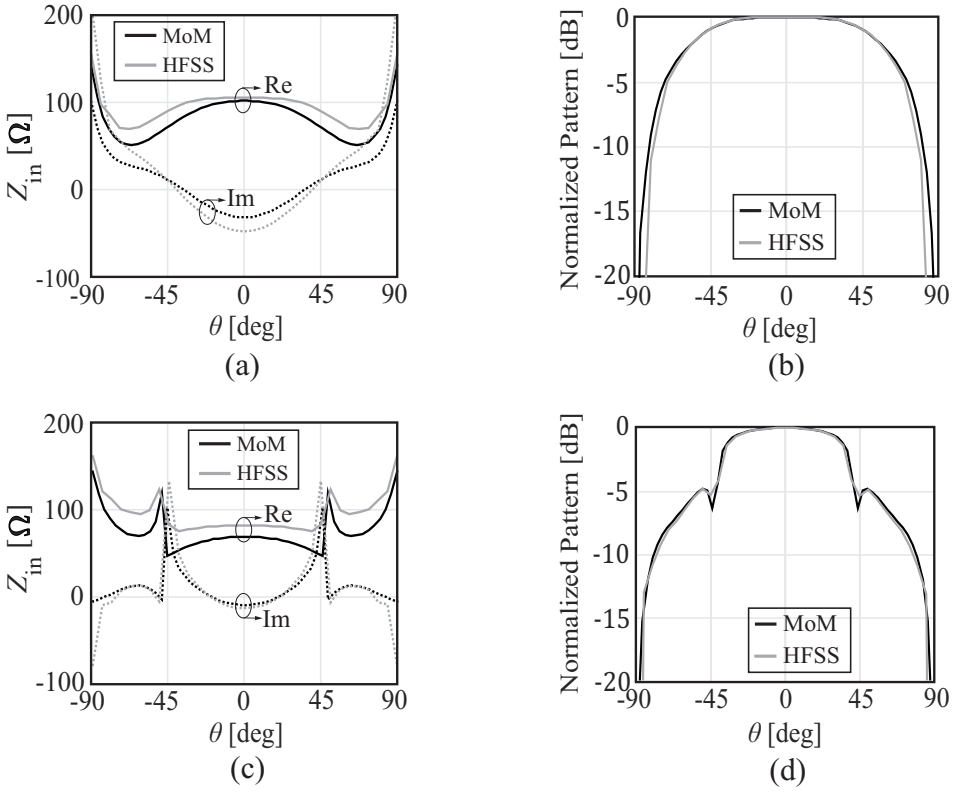

Figure 3.4: Active input impedance for an infinite array of dipoles in the presence of a backing reflector with a spacing between elements of (a) 0.5λ and (c) 0.6λ; E-plane active element pattern for (b) 0.5λ and (d) 0.6λ. The dipoles are tilted 30° and results of the MoM are compared with HFSS simulations.

3.2.2 Array of Stacked Dipoles with Backing Reflector

In this section, we study stacked dipoles in the presence of a backing reflector, as depicted in Fig. 3.5(a). The unit cell consists of an active dipole with a parasitic strip to increase directivity. The current distribution of the active dipole is the one shown in (3.10), while the one for the parasitic dipole has a similar expression with a different dipole length, l_p, and a phase shift in the z_R-direction:

$$J_p(k_x, k_y, k_z) = i_p J_0(k_y w/2) B_{l_p}(k_x \cos\alpha - k_z \sin\alpha) \cdot e^{jk_x d_z \sin\alpha} e^{jk_z d_z \cos\alpha} . \tag{3.20}$$

where i_p is the unknown coefficient indicating the amplitude of the current on the parasitic strip.

To simplify the notation, we number the basis functions with the indexes 1, 2 for the real dipoles and $1i$, $2i$ for their image, as shown in Fig. 3.5(b). To find the unknown weights for the currents on the active and passive dipoles (i_0 and i_p, respectively), we can solve the

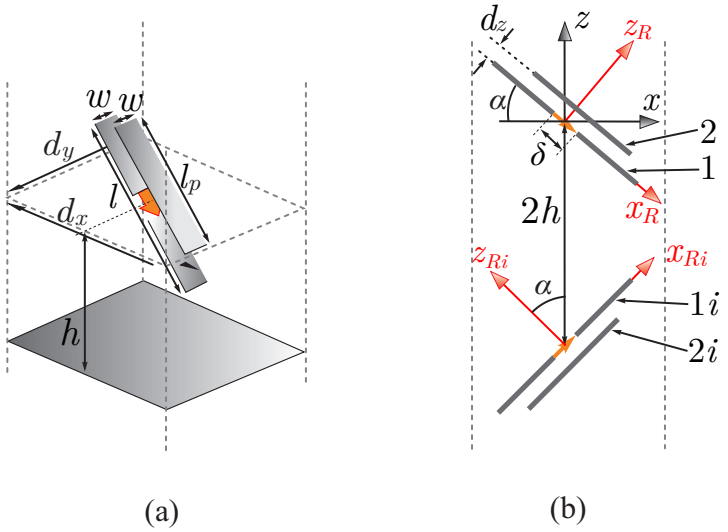

Figure 3.5: Unit cell of an infinite array of tilted dipoles in the presence of a backing reflector with the original and rotated reference systems: (a) three-dimensional view and (b) equivalent unit cell using the image theorem.

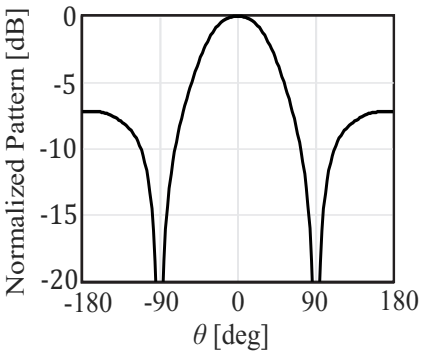

Figure 3.6: Active element pattern of a non-tilted stacked dipole.

following system of two linear equations:

$$\begin{bmatrix} i_0 \\ i_p \end{bmatrix} = \left(\begin{bmatrix} Z_l & 0 \\ 0 & 0 \end{bmatrix} + \begin{bmatrix} Z_{1,1}+Z_{1,1i} & Z_{1,2}+Z_{1,2i} \\ Z_{2,1}+Z_{2,1i} & Z_{2,2}+Z_{2,2i} \end{bmatrix} \right)^{-1} \cdot \begin{bmatrix} V_0 \\ 0 \end{bmatrix} \tag{3.21}$$

where the self and mutual impedance terms can be expressed very similarly to (3.13) and (3.17), by selecting the correspondent tilt and location of the basis functions (see Appendix B.2).

As an example, the geometrical parameters of the stacked dipole are set to $l = 0.5\lambda$, $l_p = 0.42\lambda$, $d_z = 0.07\lambda$, $w = 0.12\lambda$, $\delta = 0.1\lambda$, where λ is the wavelength at the calculation frequency. These dimensions are selected to increase the front-to-back ratio, compared

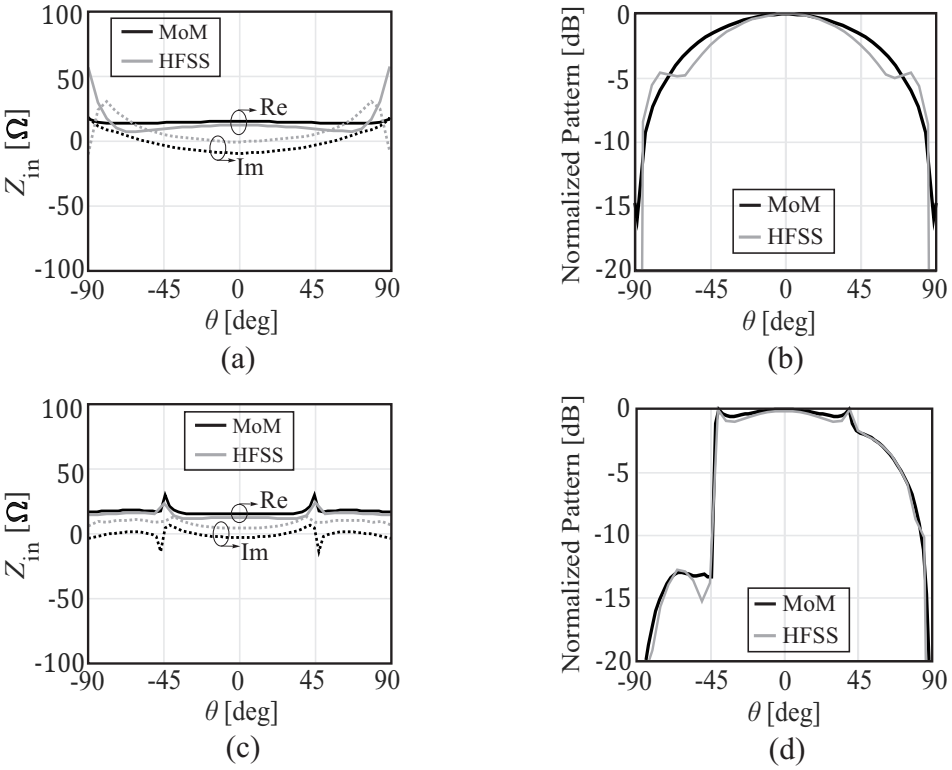

Figure 3.7: Active input impedance for an infinite array of stacked dipoles in the presence of a backing reflector with a spacing between elements of (a) 0.5λ and (c) 0.6λ; E-plane active element pattern for (b) 0.5λ and (d) 0.6λ. The dipoles are tilted 30° and results of the MoM are compared with HFSS simulations.

to a single dipole. To quantify the improvement in directivity, Fig. 3.6 shows the active element pattern of the non-tilted stacked dipole element in infinite array environment, in absence of the backing reflector. A front-to-back ratio of 7.2 dB is obtained.

Figure 3.7 reports the input impedance and the active element pattern for scanning in the E-plane, for the stacked dipole element tilted by $\alpha = 30°$, at distance $h = 0.25\lambda$ from the ground plane, and for inter-element distance of 0.5λ and 0.6λ. The input impedance for both inter-element distances is again symmetric, as expected. A larger discrepancy between the method described in this paper and HFSS can be observed in the input reactance and in the pattern for $d_x = 0.5\lambda$, mainly due to the fact that the dipoles in the unit cells are very close to each other and therefore, an entire-domain sinusoidal profile is not accurate enough to represent the current distribution of both dipoles and the coupling between neighboring elements. Nevertheless, the radiation patterns calculated with our method still show a fair agreement with HFSS.

As it can be seen in Fig. 3.7, the radiated pattern is symmetric for 0.5λ period, whereas

a non-symmetric active element pattern can be achieved for inter-element distance larger than half wavelength. Thus, by comparing the results in Fig. 3.7(d) and Fig. 3.4(d), it can be noted that the increased front-to-back ratio (or directivity) is a key property to realize non-symmetric patterns. The steep gain drop that can be observed in Fig. 3.7(d) at around $\theta_{\text{drop}} = -42°$, corresponds to the angle at which a grating lobe enters in the visible region, i.e.

$$\theta_{\text{drop}} = \sin^{-1}(1 - \lambda/d_x)\,. \tag{3.22}$$

The asymmetry can be further highlighted by analyzing the different contributions to the pattern from the active and parasitic dipoles. Figures 3.8(a) and (c) report the separate contributions to the radiated field from the active and the passive dipoles, for array period of 0.5λ and 0.6λ, respectively. The radiated field of the stacked dipole is

$$\boldsymbol{e}_{total}(\boldsymbol{r}) = \boldsymbol{e}_d(\boldsymbol{r}) + \boldsymbol{e}_p(\boldsymbol{r}), \tag{3.23}$$

where $\boldsymbol{e}_d(\boldsymbol{r})$ is the field radiated by the active dipole and its image, calculated as in (3.18), while $\boldsymbol{e}_p(\boldsymbol{r})$ is the field radiated by the passive dipole and its image.

Both fields are normalized to the maximum of the total pattern, also shown in the figure. It can be observed that the amplitudes of the individual contributions are higher than their sum, which implies a partial cancellation of the radiated fields from two elements. This is also confirmed in Fig. 3.8(b) and (d), where the phase difference between the two radiated electric fields from active and parasitic dipoles is between 160 to 230 degrees. Such values are also typical of superdirective arrays [74, 75], where higher directivity is obtained with arrays of closely spaced elements, that have very large and oppositely directed currents. It is important to remark that such configurations can lead to high Ohmic losses when targeting realistic design, due to the high current intensity. Nevertheless, efficiency aspects are not addressed in this work, as we only assume perfect electric conductors as metal.

By comparing the results for $d_x = d_y = 0.5\lambda_0$ and $d_x = d_y = 0.6\lambda_0$, it appears that for half wavelength spacing in Fig. 3.8(a), although the pattern due to the passive dipoles is non-symmetric, when summing the fields radiated by the active and passive dipoles perfect symmetry is restored in the total pattern. This can be interpreted by noting that, since the period is 0.5λ, only a single radiating Floquet mode is supported by the structure. The aperture field due to this mode tends to be uniform in amplitude in the unit cell, providing a wide and symmetric radiation pattern. For period of 0.6λ in Fig. 3.8(c), a higher order Floquet wave enters the visible region, thus the field distribution on the unit

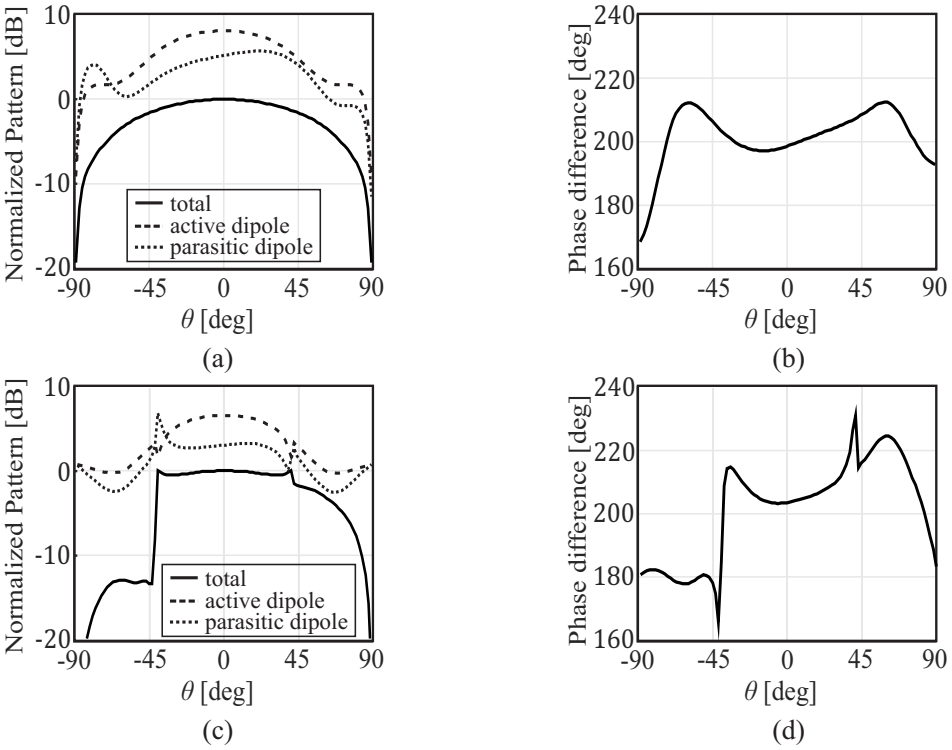

Figure 3.8: Active element pattern of array of tilted stacked dipoles with backing reflector tilted by $\alpha = 30°$, with separate contribution from active dipoles and parasitic ones: (a) $d_x = d_y = 0.5\lambda$ and (c) $d_x = d_y = 0.6\lambda$; phase difference between fields radiated by active and passive dipoles: (b) $d_x = d_y = 0.5\lambda$ and (d) $d_x = d_y = 0.6\lambda$.

cell aperture supports an additional mode associated with radiation towards a different direction. Under this condition, the currents on the active and passive dipoles can produce cancellations that suppress the gain in certain angular regions. Indeed, the phase difference between the field radiated by the active and passive dipoles in Fig. 3.8(d) is close to 180° for angles between $-45°$ and $-90°$.

3.2.3 Parametric Analysis

A parametric analysis on the radiation pattern of the tilted stacked dipole array is carried out to determine the parameters that affect the power radiated in specific directions. The considered geometrical variables are the inter-element spacing (d_x, d_y) and the inclination angle of the dipoles (α). Figures 3.9(a) and (b) show the active element patterns when varying the inter-element distance and the tilt angle, respectively. All patterns are normalized to the broadside value for the maximum unit cell size, i.e. $d_x = d_y = 0.65\lambda$. Due to the relation in (3.22), the array period can be used in a design phase as a parameter

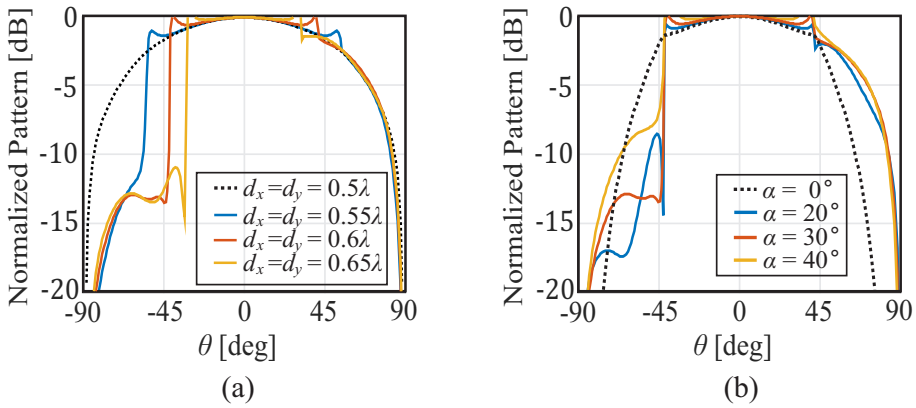

Figure 3.9: Active element pattern for an infinite array of stacked dipoles (a) tilted 30° for different spacings d_x, d_y; (b) with an inter-element distance of 0.6λ for different tilt angles α.

to select the angle at which the pattern drop-off occurs, as shown in Fig. 3.9(a). When increasing the array unit cell dimensions, the active element pattern becomes more and more directive, with a redistribution of radiated power from the low-gain regions ($\theta < -\theta_{\text{drop}}$) to the rest of the field of view. From Fig. 3.9(b), it is apparent that the tilt angle is a convenient parameter to shape the gain levels in the suppressed angular region. As a result, the combination of the two parameters (d_x and α) can be conveniently used to effectively realize angular filtering by mean of array of stacked dipoles or patches. For comparison, Fig. 3.9(b) also shows the active element pattern when the elements are not tilted, to highlight how the tilt does not change the overall radiated power, but allows to redistribute it in the field of view by increasing the gain for positive scan angles while reducing it for negative scan angles. The active pattern for non-tilted dipoles does not present a null when grating lobes entering in the visible region, but only a discontinuity in derivative, which is a known property of the scan impedance in dipole arrays scanning in the E-plane [73].

3.2.4 Grating Lobe and Polarization Analysis

Since the asymmetry of the radiation pattern is achieved only for inter-element distances higher than half wavelength, a grating lobe analysis is reported in this section. For example, Fig. 3.10 shows the grating lobe diagram for the array of tilted stacked dipoles, when the period is 0.6λ. To clarify the relation between grating lobes and the active element pattern, we also plot a color map of the active element pattern as a function of the scan directions (k_{x0},k_{y0}) in the circle with radius k_0 centered in the origin, representing the visible region. It

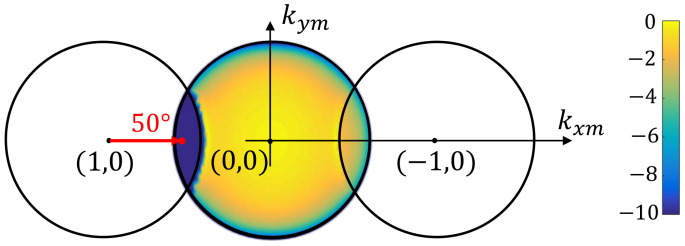

Figure 3.10: Grating lobe diagram for a stacked dipole array with inter-element distance of 0.6λ, tilted by $\alpha = 30°$. The grating lobe circles correspondent to the Floquet modes (m_x,m_y) equal to $(-1, 0)$, $(0, 0)$ and $(0, 1)$ are represented and the active element pattern is mapped in the visible region.

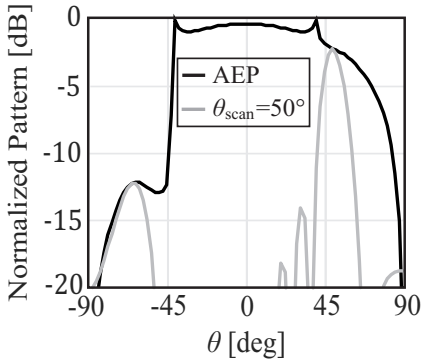

Figure 3.11: Active element pattern (AEP) of an array of stacked dipoles with inter-element distance 0.6λ and array pattern calculated by windowing technique for 10 elements, when scanning to 50°. Elements are tilted by $\alpha = 30°$.

is evident that, as the circles associated with the Floquet modes overlap, grating lobes can enter the visible region when scanning. For example, when the array scans to $\theta_{\text{scan}} = 50°$, the Floquet mode (m_x, m_y) equal to $(-1, 0)$ is within the visible region. However, this higher order Floquet wave corresponds to a direction for which the active element pattern is lower than −12 dB. To clarify this aspect, a pattern cut for $\phi = 0°$ is shown in Fig. 3.11, including the active element pattern as well as the array pattern for 10×10 elements, calculated with a windowing technique [76, 77]. It can be noted that the grating lobe points at −65° but it is weighted by the element pattern, thus it remains −12 dB below the maximum. As a consequence, the gain of the main beam does not sensibly decrease with respect to the ideal $\cos\theta$ profile.

Figure 3.12 shows u-v cross-polarized patterns of the unit cell shown in Fig. 3.5, for element tilt of $\alpha = 0°$ and $\alpha = 30°$. In the E-plane, the cross-pol is not affected by the tilt, since both the x- and the z- components of the current radiate co-polar fields. However, in the

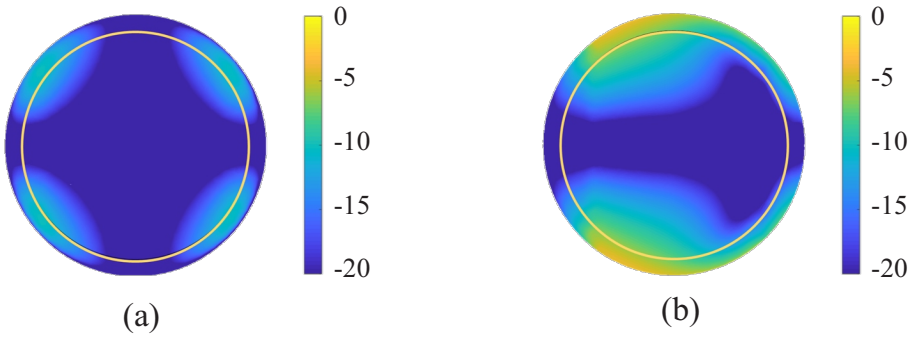

Figure 3.12: Cross-polarized u-v pattern of an infinite array of stacked dipoles spaced $0.6\lambda_0$ for (a) $\alpha = 0°$ and (b) $\alpha = 30°$. The yellow circles represent the scanning angle of 60°.

H-plane or in diagonal planes, the X-pol increases due to the tilting. Within a scan range up to $\theta = 60°$ (indicated with a yellow inner circle in the plot), the worst X-pol is -6 dB for the tilted element, while it is -10 dB for the non-tilted one.

3.3 Finite Linear Array Analysis

To investigate the radiation properties of arrays comprising a finite number of elements, a spectral MoM for finite linear array of tilted stacked dipoles is also derived. The method analyzes arrays of dipoles with arbitrarily tilt in the presence of a backing reflector. For efficient analysis of large arrays in terms of radiation patterns, we make the same approximation as for the previous infinite array analysis, considering only a single sinusoidal entire-domain basis function for the longitudinal current distribution on each dipole. However, the method can use piecewise linear (PWL) sub-domain basis functions along the dipoles' axis, if a more accurate estimation of the input impedance is desired.
The geometry under analysis is depicted in Fig. 3.13, which shows the original array with the backing reflector and the equivalent problem obtained by applying the image theorem. The array consists in N_x stacked dipole elements in the presence of the ground plane, thus leading to $4N_x$ basis functions for the active and passive dipoles and their images. The mutual impedances are computed in different ways, depending on the pair of basis and test functions to be evaluated.

3.3.1 Mutual Impedance Computation

Let us consider any pair of parallel dipoles, for example oriented along $\hat{\boldsymbol{x}}_R$, indicated with the indexes n and n', respectively. The dipoles are centered in the points (x_R, y, z_R) equal

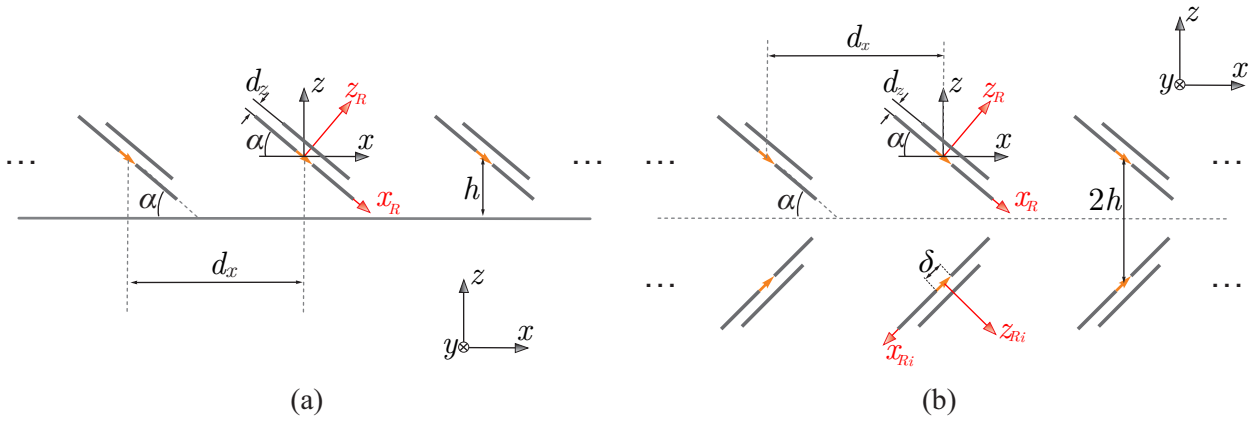

Figure 3.13: Linear array of skewed stacked dipoles (a) above and infinite ground plane and (b) with its images after applying the image theorem.

to $(x_{Rn}, 0, z_{Rn})$ and $(x_{Rn'}, 0, z_{Rn'})$, respectively. The general expression for the self and mutual impedance can be written as a double spectral integral:

$$Z_{nn'} = -\frac{1}{2\pi}\int_{-\infty}^{\infty} B_{l_{n'}}(k_{x_R}) B_{l_n}(-k_{x_R}) D_{nn'}(k_{x_R}) e^{-jk_{x_R}(x_{Rn}-x_{Rn'})} dk_{x_R} \tag{3.24}$$

where l_n and $l_{n'}$ are the length of the n-th and n'-th dipoles, respectively, and the function $D_{nn'}$ is given by

$$D_{nn'}(k_{x_R}) = \frac{1}{2\pi}\int_{-\infty}^{\infty} J_0(k_y w/2) G_{2D,x_R x_R}(k_{x_R}, k_y) e^{-j\sqrt{k_0^2 - k_{x_R}^2 - k_y^2}|z_{Rn}-z_{Rn'}|} dk_y \,. \tag{3.25}$$

The expressions in (3.24) and (3.25) are obtained by considering Galerkin projection for the x_R-oriented distribution, while assuming point matching for the y- and z_R-variables. This choice is made so that, when computing the self impedance, for which $z_{Rn} = z_{Rn'}$, the integral in (3.25) can be solved rigorously in closed form as done in [70], thus only a single spectral integral in the variable k_{x_R} remains to be evaluated (see Appendix D.1). When the distance between dipoles is much larger than the dipole width ($|z_{Rn} - z_{Rn'}| \gg w$), (3.25) can also be approximately solved analytically, as shown in [78] (see Appendix D.1). For distances $|z_{Rn} - z_{Rn'}|$ in the order of w, we solve numerically the double integral, by pretabulating the function $D_{nn'}$ for a set of k_{x_R} points and using a cubic interpolation to fit the function through these points.

Alternatively, one can use the closed form expressions for the self and mutual impedance from [74] and [79], which assume infinitely thin dipoles. These expressions are accurate

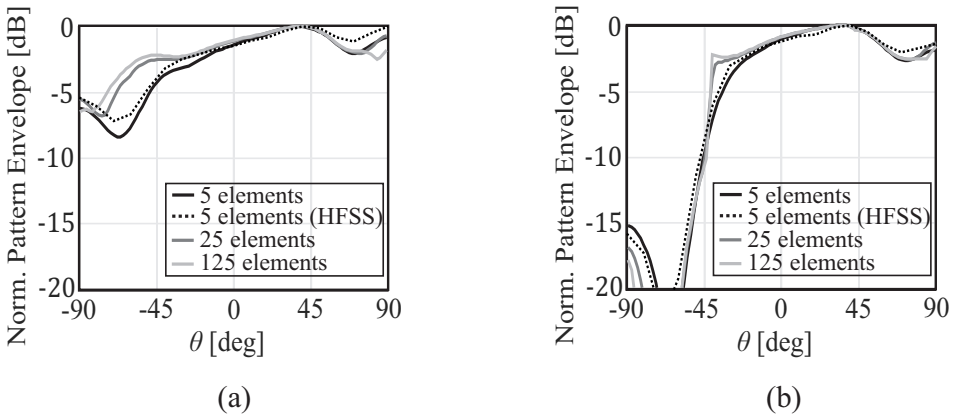

Figure 3.14: Pattern envelope as a function of the number of elements for a linear array of stacked dipoles in the presence of a backing reflector. The inclination angle is $\alpha = 30°$ and the distance between elements is (a) $d_x = 0.5\lambda$ and (b) $d_x = 0.6\lambda$.

for sufficiently large distance between dipoles and for very small dipole width. However, when the dipole width and the distances are in the order of $\lambda/10$, the expressions in (3.24) and (3.25) provide better accuracy, since they account for the transverse distribution of the current on the strips (see Appendix D.2).

The mutual impedance between dipoles that are not parallel (any real dipole with any image) is calculated analytically using the method described in [80], which is valid for skewed dipoles with arbitrary length and distance (see Appendix D.3).

Moreover, one can note that, since we assume that the tilt angle is equal for all the elements, the resulting MoM matrix is a block Toeplitz matrix, thus only a reduced set of the impedance terms needs to be calculated.

3.3.2 Radiation Properties

Based on the efficient MoM solution described in the previous section, a parametric analysis on the radiation pattern of the finite array is carried out, varying the inter-element distance d_x, the angle of inclination α and the number of elements in the array N_x. The geometrical dimensions for the stacked dipole element are the same as in Sec. 3.2.2.

Figure 3.14 reports the normalized envelop of the array radiation pattern as a function of the scan angle, for two different array periods and for various array sizes. The envelope of a 5 elements linear array simulated with HFSS is also included to verify the MoM solution. It is apparent that, when the distance between elements is half wavelength (Fig. 3.14(a)), a small pattern asymmetry is obtained for small arrays, but such asymmetry tends to

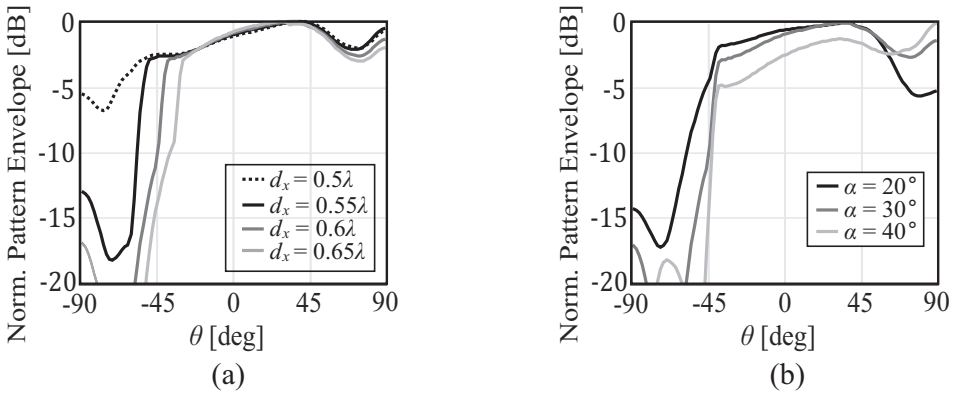

Figure 3.15: Active element pattern of a linear array of 25 stacked dipoles (a) tilted 30° for different spacings d_x; (b) with an inter-element distance of 0.6λ for different tilt angles α.

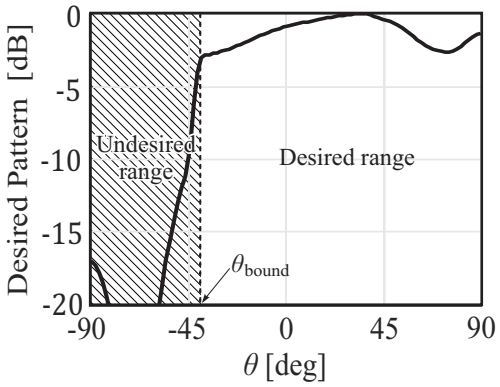

Figure 3.16: Definition of desired and undesired angular ranges, bounded by the direction θ_{bound}.

disappear when increasing the number of elements. This observation is in line with infinite array results. The curves in Fig. 3.14(b) exhibit a very different behavior for array periods larger than $\lambda/2$, for which the asymmetry remains nearly constant and independent on the number of elements. We can also note that, since the array is one dimensional and located on an infinite ground plane, the gain for positive scan angles does not follow the $\cos\theta$ typical of doubly-periodic array, thus it does not drop to 0 even for scanning close to 90°. This behavior is typical of linear arrays, where a proper phase shift between the elements can still produce high gain in the end-fire direction [74].

Figure 3.15(a) shows the normalized E-plane pattern for an array of 25 elements with different periods and inclination angle of $\alpha = 30°$. Figure 3.15(b) presents similar patterns when the period is fixed as $d_x = 0.6\lambda$ and different inclination angles are considered. Similar conclusions as for the infinite array case can be made, by observing that angular position of the gain drop can be controlled with the array period. Unlike the infinite

array case, even for the period $d_x = 0.5\lambda$, a 25-element linear array can achieve a certain degree of asymmetry. From Fig. 3.15(b), the tilt angle mainly modifies the gain levels in low-radiation angular region, while also influencing the pattern shape for wide positive angles.

Figures 3.9(a) or 3.15(a) also illustrate the frequency dependence of the proposed concept. For a given array spacing, changing the frequency causes a shift of the angle at which the gain drops. To quantify the effect of this shift on the performance and to provide guidelines for array designs, we define in the next section a figure of merit to assess the asymmetry.

3.3.3 Design Guidelines

To provide guidelines for the design of arrays with a desired pattern shape, a more extensive parametric analysis is given in this section. We can imagine to divide the field of view in two angular regions, as in Fig. 3.16: the 'desired range' refers to the angles for which a high and stable gain is wished for, whereas the 'undesired range' is where suppression of gain is intended. These two regions are limited by the angle θ_{bound}. To quantify the asymmetry of the pattern, we define a figure of merit (A) that we refer to as an asymmetry factor:

$$A(\theta_{\text{bound}}) = 1 - \frac{P(-90^\circ < \theta < \theta_{\text{bound}})}{P(\theta_{\text{bound}} < \theta < 90^\circ)} \frac{90^\circ - \theta_{\text{bound}}}{\theta_{\text{bound}} + 90^\circ} \tag{3.26}$$

where $P(\theta_1 < \theta < \theta_2)$ is the power contained between the angles θ_1 and θ_2. The ratio between the angular regions of the desired and undesired ranges $(90^\circ - \theta_{\text{bound}})/(\theta_{\text{bound}} + 90^\circ)$ has been included in (3.26) to compensate for the decrease in power ratio when θ_{bound} is farther away from broadside. To clarify this aspect, let us consider an ideal radiation pattern, equal to 1 in the desired range and 0.1 in the undesired range. If we calculate the figure of merit A removing the ratio $(90^\circ - \theta_{\text{bound}})/(\theta_{\text{bound}} + 90^\circ)$, the resulting values will depend on θ_{bound}: e.g., $A(-80^\circ) = 1 - (0.1 \times 10^\circ)/(1 \times 170^\circ) = 0.994$, $A(-45^\circ) = 1 - (0.1 \times 45^\circ)/(1 \times 135^\circ) = 0.967$, $A(0^\circ) = 1 - (0.1 \times 90^\circ)/(1 \times 90^\circ) = 0.9$. On the other hand, adding the term $(90^\circ - \theta_{\text{bound}})/(\theta_{\text{bound}} + 90^\circ)$ gives the same asymmetry factor in all cases ($A(-80^\circ) = A(-45^\circ) = A(0^\circ) = 0.9$), which depends only on the values of the radiation pattern in the desired and undesired regions.

Figure 3.17 shows a map of the asymmetry (normalized to the maximum) for different θ_{bound} (-10°, -20°, -30° and -40°) while varying the inter-element distance and the inclination angle. An array of 25 elements is considered. Depending on the specified θ_{bound}, the optimal configuration to achieve maximum asymmetry occurs for different d_x and α.

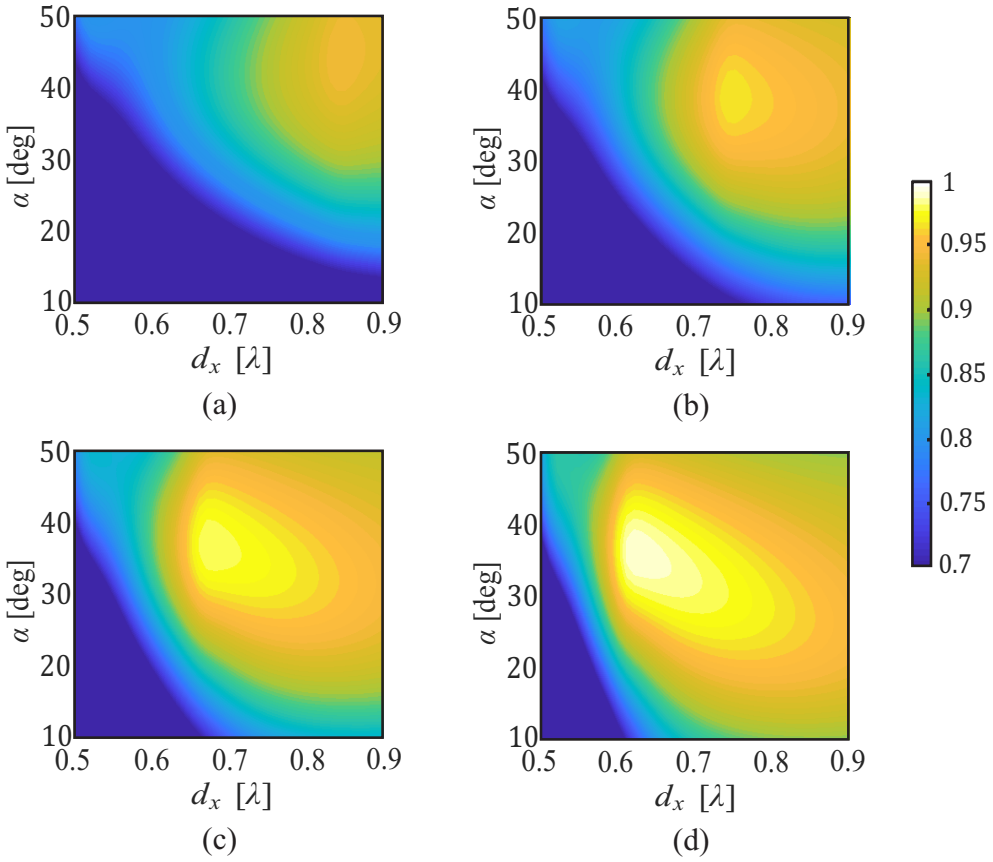

Figure 3.17: Asymmetry of the radiation pattern in dB varying the inclination angle and inter-element distance for θ_{bound} equal to (a) $-10°$, (b) $-20°$, (c) $-30°$ and (d) $-40°$.

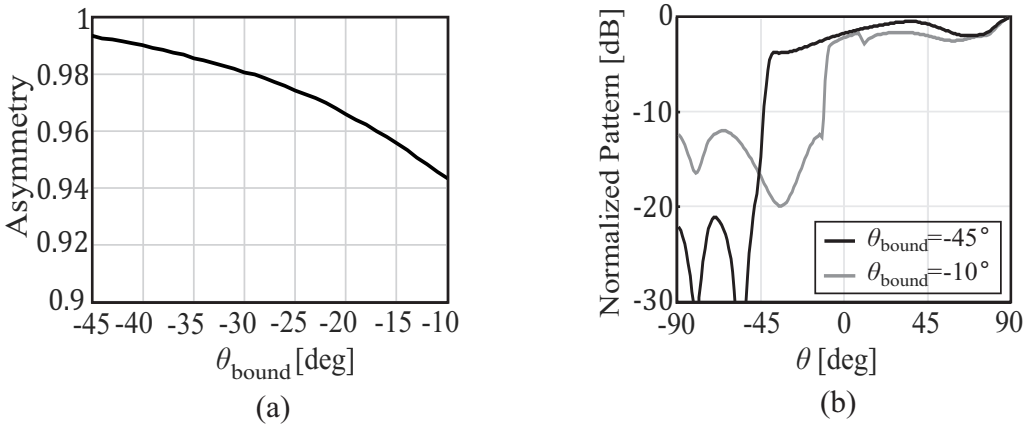

Figure 3.18: (a) Maximum value of the asymmetry factor when varying θ_{bound} and (b) normalized array pattern envelopes for $\theta_{\text{bound}} = -45°$ and $\theta_{\text{bound}} = -10°$.

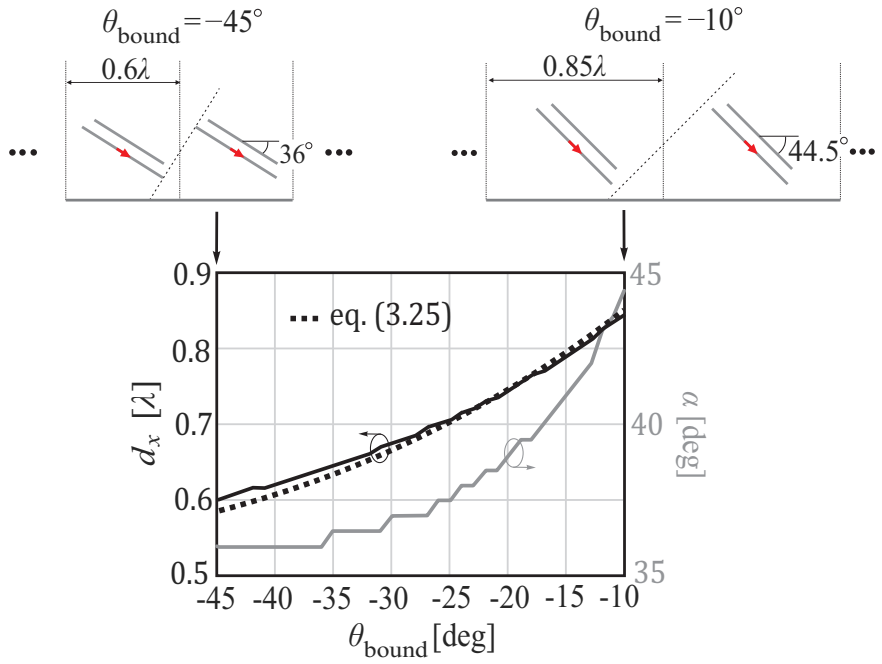

Figure 3.19: Inter-element distance and inclination angle corresponding to maximum asymmetry for different θ_{bound}.

Figure 3.18(a) shows the maximum of the asymmetry while varying θ_{bound}. The decreasing values can be explained by observing the array pattern envelopes for $\theta_{\text{bound}} = -45°$ and $\theta_{\text{bound}} = -10°$, in Fig. 3.18(b). The side lobes in the undesired region are higher for larger periods, which explain the decrease in the asymmetry factor.

The values of inclination angle and inter-element spacing correspondent to the maxima of the asymmetry factor are plotted versus θ_{bound} in Fig. 3.19. The value of d_x that yields the maximum increases with θ_{bound} and also corresponds to the value that gives $\theta_{\text{drop}} = \theta_{\text{bound}}$ calculated from (3.22). The tilt angle that gives maximum asymmetry is also changing with θ_{bound}. An interpretation of this behavior can be related to the mutual blockage effects between array elements that limits the maximum tilt angle for small periods, as depicted in the inset of Fig. 3.19.

3.4 Conclusions

We presented an analysis of infinite and finite arrays with tilted elements, with particular focus on their radiation characteristics. A periodic method of moments was developed to analyze different dipole geometries through analytical expressions. It was shown that

skewed stacked dipole elements, with front-to-back ratio higher than one, can be used to achieve non-symmetric radiation when used in combination with a backing reflector, for inter-element spacings larger than half wavelength. The dependence of the active element pattern on the inclination of the elements and the array period was discussed. These two parameters can be varied to control the pattern profile, thus the proposed elements can be effectively employed to implement pattern shaping.

Finite linear arrays of stacked dipoles were also investigated. The analysis was based on a efficient MoM approach, based on entire domain basis functions, where several mutual coupling terms were computed analytically. The finite array analysis allowed to highlight the dependence of the pattern asymmetry on the number of elements, besides the spacing and tilt angle.

Chapter 4

Angular Filtering Array: Prototype

This chapter presents a design of a linear array of tilted dipoles to achieve radiation patterns with asymmetric angular filtering characteristics. To realize the asymmetric radiation, the dipole elements are spaced by a distance larger than half a wavelength, thus allowing for grating lobes to occur in the visible region. Moreover, the dipoles are loaded with artificial dielectrics to increase the front-to-back ratio and consequently to enable higher gain in certain desired angular regions. Based on the design, a linear array with 10 elements is manufactured and tested. The measured results show the ability of such an array to achieve stable gain from broadside up to 90° scanning, while implementing a stop-band angular filter for negative scanning angles.

4.1 Unit Cell Design

In Chapter 3, the guidelines to design an array with asymmetric radiation properties were discussed. The main unit cell under analysis consisted in an idealized element with infinitely thin flat strip dipoles, fed with a delta-gap excitation, as shown in Fig. 4.1(a). In this section, we propose a realistic implementation of the element, based on PCB technology.

4.1.1 Single Dipole Element with Parasitic Loading

To enable a simple realization of the flat strip dipole element, we first consider an equivalent isolated element where the active dipole and the parasitic strip are printed on a vertically oriented thin dielectric slab. Figure 4.2(a) shows the considered structure with the characteristic geometrical parameters. The dimensions of the elements are chosen as: $l = 0.41\lambda_0$, $l_p = 0.37\lambda_0$, $w = 0.05\lambda_0$, $\delta = 0.01\lambda_0$ and $d_z = 0.7\lambda_0$, where λ_0 is the wavelength at 12 GHz.

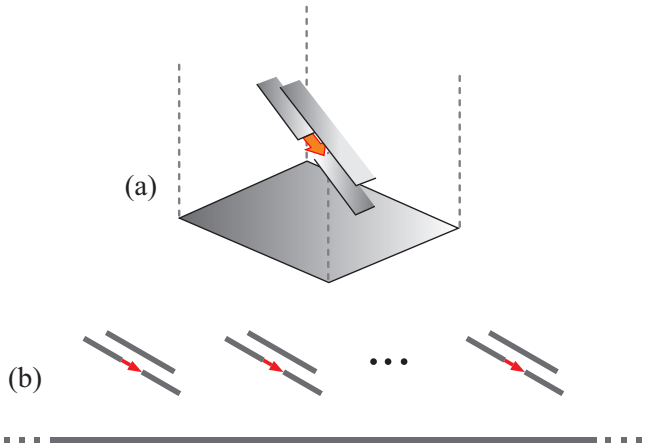

Figure 4.1: Array of titled stacked dipole elements, in the presence of an infinite ground plane: (a) three-dimensional view of the unit cell and (b) side view of the array.

Table 4.1: Geometrical Parameter of Element in Fig. 4.3, with Respect to the Wavelength λ_0 at 12 GHz.

l	w	δ	l_{ADL}	w_{ADL}	s
$0.434\lambda_0$	$0.05\lambda_0$	$0.05\lambda_0$	$0.212\lambda_0$	$0.0336\lambda_0$	$0.01\lambda_0$

The dielectric slab selected for the design is Rogers RO4530 TM with relative dielectric constant $\varepsilon_r = 3.66$ and thickness $t = 101\,\mathrm{m}$. The dimensions are optimized so that the directivity of the element is maximized. The simulated E-plane pattern of a the single element in free space is reported in Fig. 4.2(b), at 12 GHz, exhibiting a front-to-back ratio of 12 dB. Figure 4.2(c) depicts the simulated reflection coefficient of the element, showing a rather narrow bandwidth of only 2% centered at 12 GHz, normalized to a low impedance of 10 Ω.

To enhance the front-to-back ratio of the element as well as the bandwidth, a solution consisting of a tilted dipole element loaded with 3 layers of artificial dielectric (AD) is proposed in Fig. 4.3(a). This element is also printed on a vertical PCB with a dielectric with the same relative permittivity and thickness as for the stacked dipole solution ($\varepsilon_r = 3.66$, $t = 101\,\mathrm{m}$). The dimensions, reported in Table 4.1, were tuned to enhance the directivity of the element. The single element E-plane pattern at 12 GHz and the reflection coefficient are shown in Fig. 4.3(b) and (c), respectively. The dipole loaded with artificial dielectric has a back lobe with −20 dB level and a bandwidth of 6%, with respect to the normalization impedance of 30 Ω.

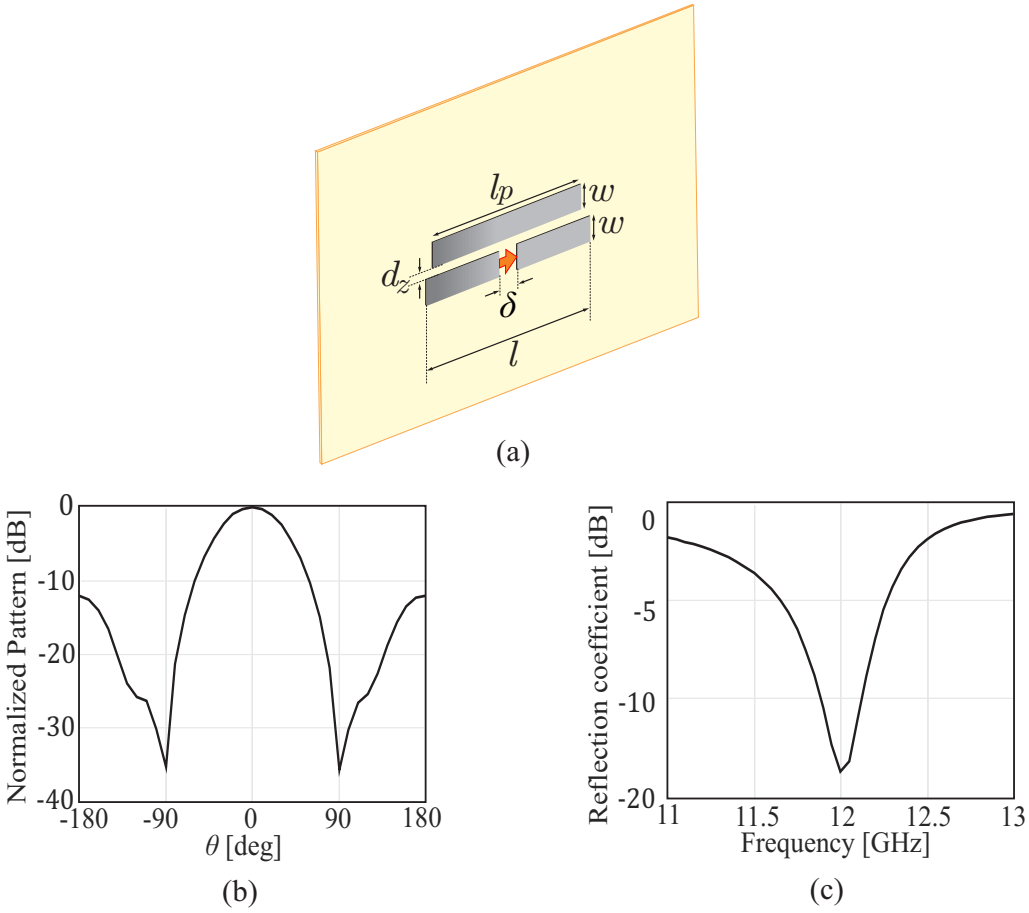

Figure 4.2: (a) Single element of a stacked dipole printed on a PCB, (b) E-plane pattern and (c) reflection coefficient of the single element described in (a).

4.1.2 Infinite Array of Dipoles Loaded with Artificial Dielectrics

We now consider the element in Fig. 4.3(a), tilted by an angle α and embedded in an infinite linear array environment, in the presence of a backing reflector. The resulting unit cell is depicted in Fig. 4.4(a). The distance between the center of the dipole and the infinite ground plane is $h_{\text{gp}} = 0.25\lambda_0$ and the total height of the dielectric is $h = 0.7\lambda_0$.

To describe the angular filtering function, let us imagine to divide the angular region between $-90°$ and $90°$ in two portions, one desired, where high gain is wished for, and one undesired, where gain suppression is targeted (Fig. 4(b)). If the angle bounding these two regions is referred to as θ_{drop}, from the study done in [81], we can derive an optimal inter-element spacing and inclination angle of the elements to achieve a desired θ_{drop}. For example, the choice of $\theta_{\text{drop}} = -20°$ results in an optimal period of $d_x = 0.75\lambda_0$ and an optimal inclination angle of $\alpha = 40°$. Figure 4.4(b) reports the simulated active element

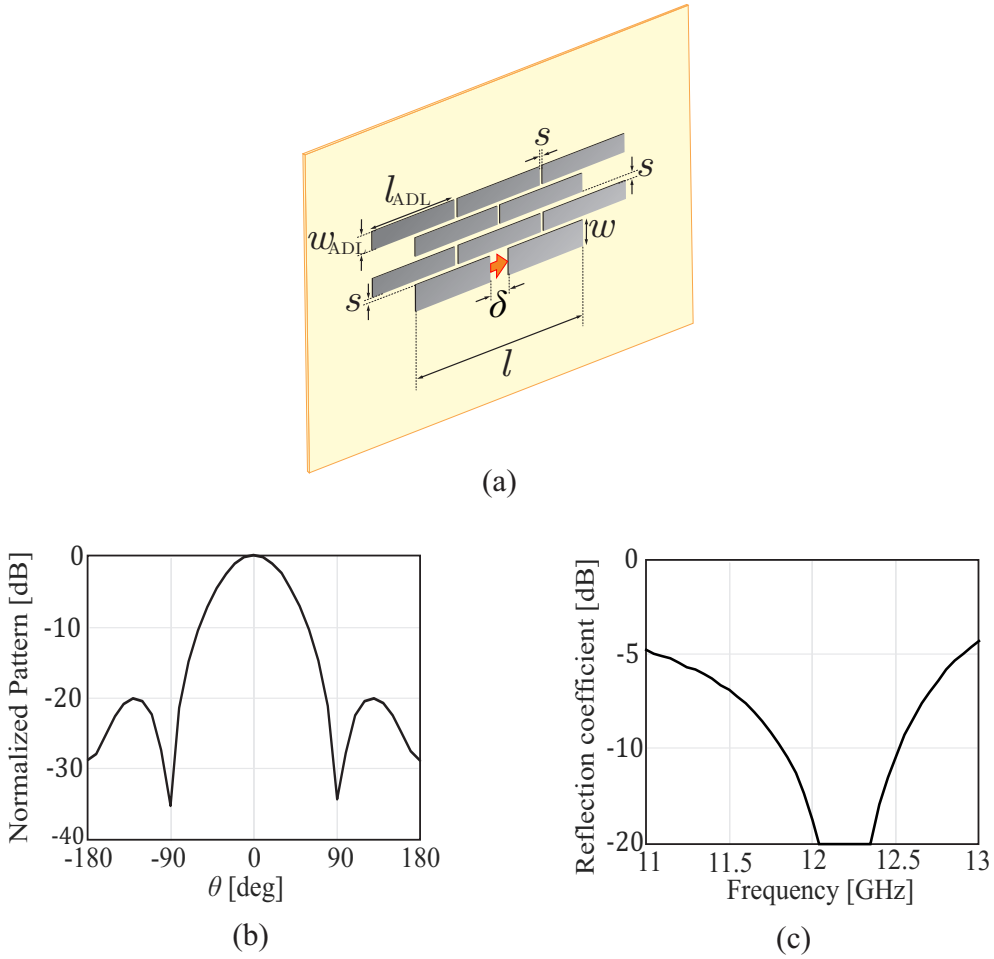

Figure 4.3: (a) Single element of a dipole loaded with artificial dielectric layer printed on a PCB, and its (b) single element E-plane pattern and (c) reflection coefficient.

pattern in the E-plane at 12 GHz. The radiation pattern shows a clear drop in gain in the range $-90° < \theta < -30°$, a roll-off region centered around the target value $\theta_{\text{drop}} = -20°$, and and almost constant value for angles between 0° and 90°. The active reflection coefficient at 12 GHz and the active input impedance are shown in Fig. 4.4(c) and (d), respectively, as a function of the scan angle. It can be noted that the impedance is almost constant with scan angle, which is a consequence of the low mutual coupling between the elements. Indeed, the large interelement spacing ($0.75\lambda_0$) yields low coupling, thus the active input impedance is close to the passive input impedance and hardly dependent on the scan angle.

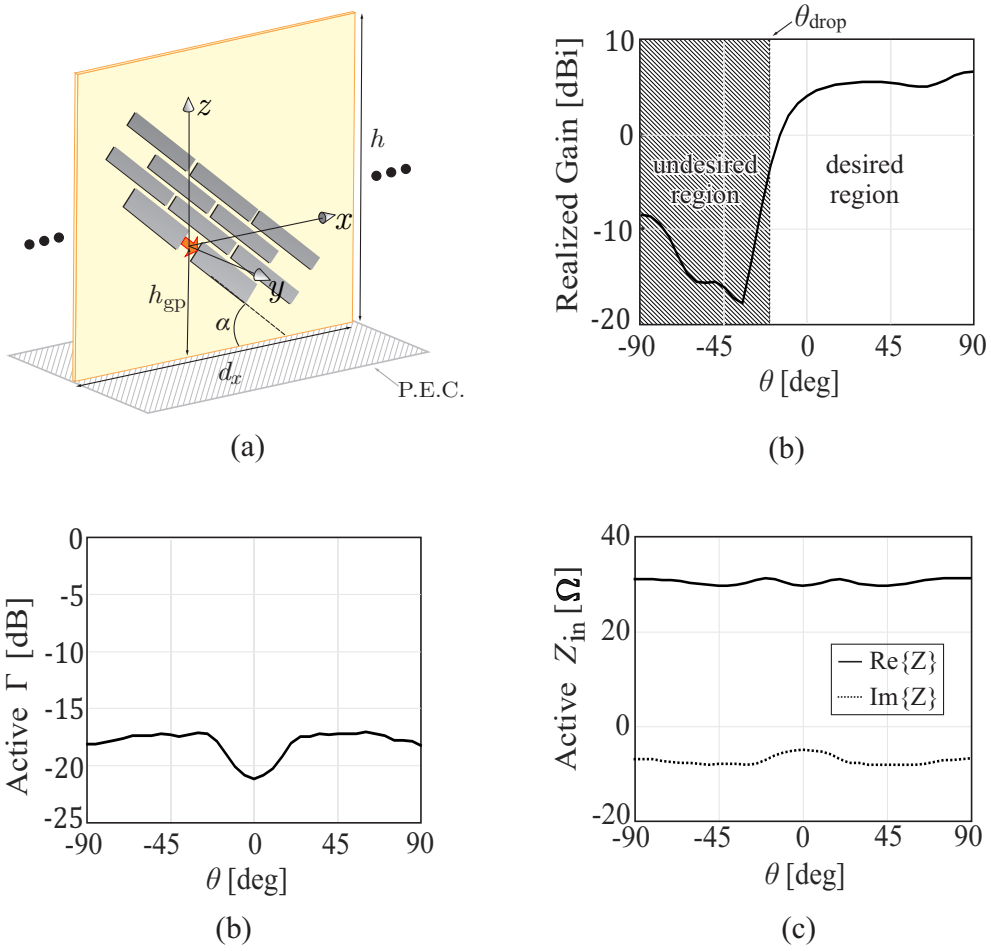

Figure 4.4: (a) Infinite one-dimensional array unit cell of a tilted dipole with artificial dielectric loading, in the presence of a backing reflector; (b) *E*-plane realized gain active element pattern, (c) active reflection coefficient and (d) active input impedance, versus scan angle.

4.1.3 Feed Design

The last step of the unit cell design consists in replacing the ideal delta-gap feed with a realistic feeding structure. We employ a microstrip feeding line with a Marchand balun to avoid the excitation of common mode currents. A two quarter-wave section transmission line is used to transform the 30 Ω impedance at the antenna terminals up to 50 Ω at the coaxial connector input. For the sake of simple realization, the horizontal ground plane is replaced by a vertical ground plane printed on the same PCB as the dipole and the feeding lines (see Fig. 4.5(a)). The parameters of the feed structure are illustrated in Fig. 4.5(b) and Fig. 4.5(c) and their values can be found in Table 4.2.

Figure 4.6(a) shows the simulated active element pattern, comparing directivity and real-

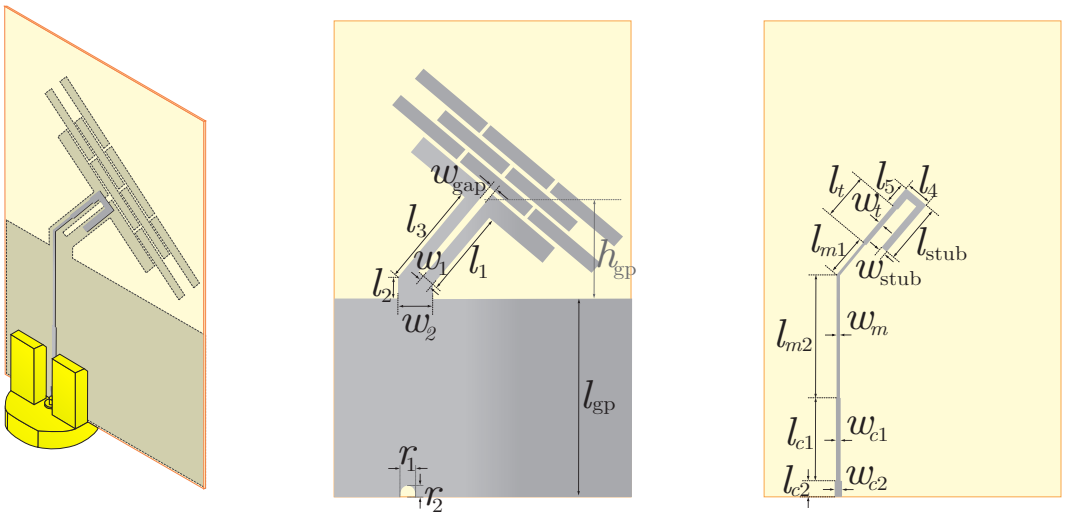

Figure 4.5: (a) 3D view of the array element with an SMA connector, (b) front and (c) back of the unit cell design with the radiating element, the feeding lines with a Marchand balun and a vertical ground plane.

Table 4.2: Geometrical Parameter of the Feed Structure (in mm)

w_{gap}	l_1	l_2	l_3	l_{gp}	w_1	w_2	l_{stub}
0.4	6.55	1.39	5.5	12.5	0.8	2.21	3.85

l_t	l_{m1}	l_{m2}	l_4	l_5	l_{c1}	l_{c2}	w_{stub}	w_t	w_m	w_{c1}	w_{c2}	r_1	r_2
3	2.6	14.04	1.65	1.35	5.25	1	0.45	0.3	0.18	0.3	0.6	1.02	0.75

ized gain. The simulation includes the feeding lines and the connector and accounts for the material losses, both metal and dielectric. The difference between directivity and gain is about 0.8 dB, which corresponds to a simulated efficiency of 83%. We can observe that gain levels in the undesired region are about -15 dB below the maximum gain, similarly to the previous results for the ideal feed. Figure 4.6(b) reports the active input impedance at 12 GHz, versus the scan angle. The impedance is well matched to 50 Ω and marginally varying with the scan angle.

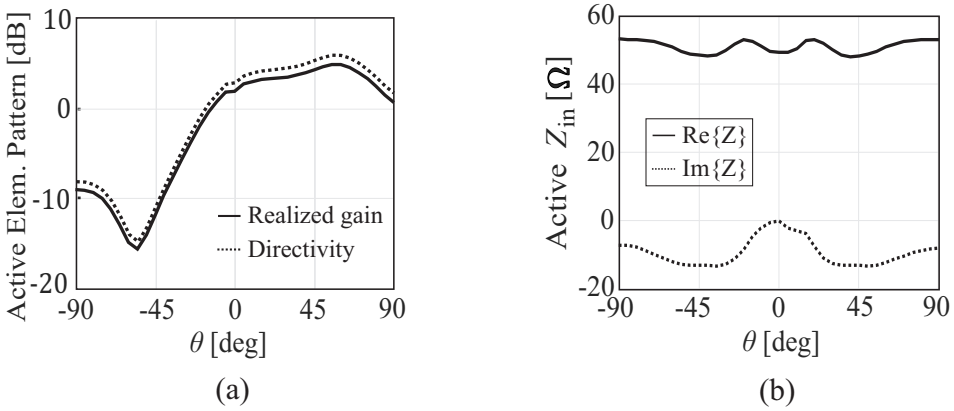

Figure 4.6: (a) E-plane radiation pattern and (b) input impedance while varying the scanning angle of the unit cell shown in Fig. 4.5(a).

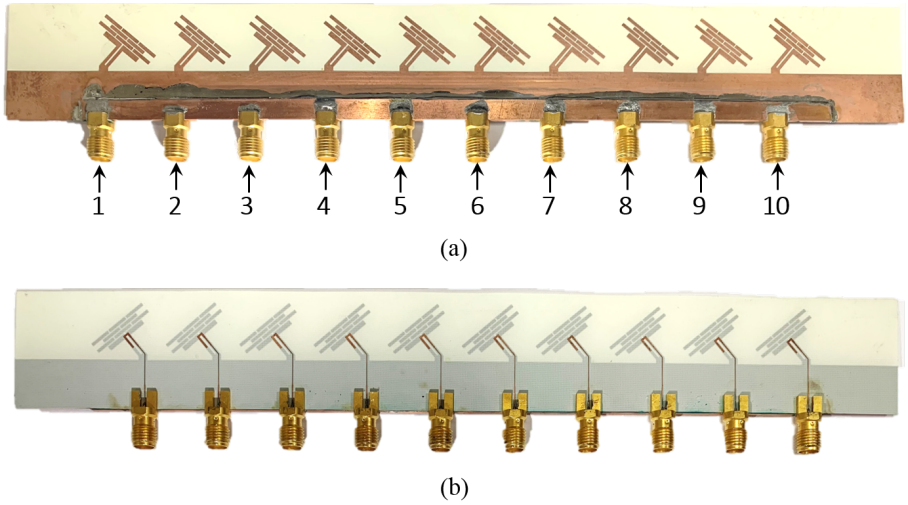

Figure 4.7: Photo of the 10-element linear array prototype: (a) front and (b) back side.

4.2 Array Prototype

Based on the unit cell design presented in the previous section, a finite linear array comprising 10 elements was manufactured (see Fig. 4.7). A subset of the array S-parameters was measured, i.e. the coupling coefficients of the elements with index 1, 5 and 10 with all the others. This allows to compute the active reflection coefficient of one central element (element 5) and the two edge elements (1 and 10) for different scan angles. The results are shown in Fig. 4.8. Simulations of the finite array are also reported in the same figure for comparison. The elements show a matching bandwidth of about 10%, which is almost constant when scanning.

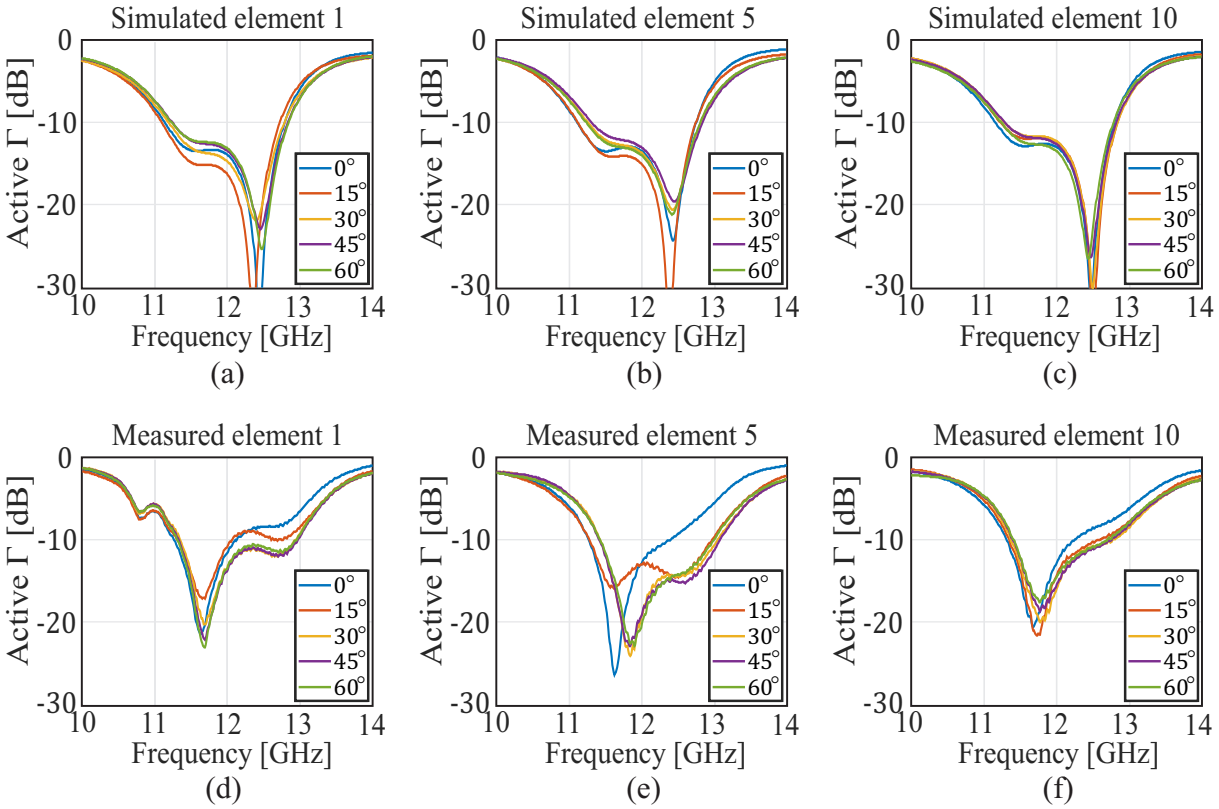

Figure 4.8: Simulated and measured active reflection coefficient for (a) and (b) element 1, (c) and (d) element 5, and (e) and (f) element 10.

The measured gain active element patterns in the E-plane are reported in Fig. 4.9, for a few array elements, at a frequency of 12 GHz. Because of truncation effects in the finite array, the gain patterns differ for each element. For example, element 1 displays a lower level side-lobe pointing at $-90°$, compared to other elements. All measured radiation patterns closely resemble the active element pattern simulated with the infinite array approximation, also shown in Fig. 4.9. Larger discrepancies occur at angles close to $\pm 90°$. This is due to some reflections from the plastic frame holding the antenna, used for the measurements.

The H-plane gain pattern of the central element of the array is shown in Fig. 4.10, comparing simulation with measurements. Also the cross-polarized component is shown in the figure. In fact, in the E-plane, the cross-pol is not affected by the tilt of the dipoles nor by the feeding structure, since both the planar and vertical components of the current radiate co-polar fields. However, in the H-plane, the cross-polar component increases for angles away from broadside, due to the tilting and the radiating currents.

By summing the measured active elements patterns with the proper phases, we can also estimate the total array patterns. The resulting gain patterns are shown in Fig. 4.11,

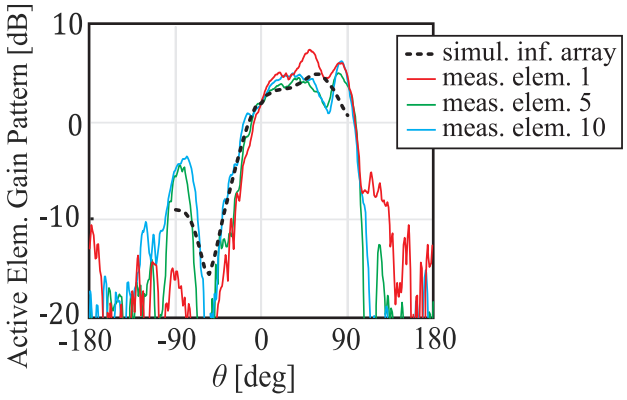

Figure 4.9: Active element pattern (gain) of three elements of the array, compared with infinite array simulations.

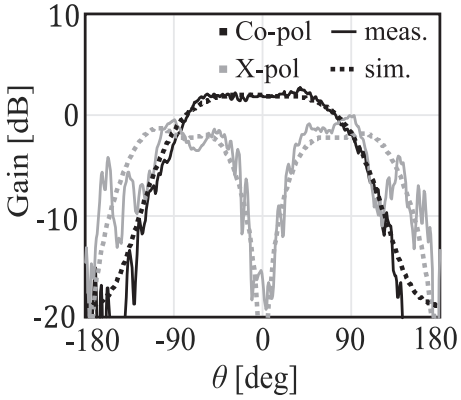

Figure 4.10: Co-polar and cross-polar H-plane gain pattern of the element 5 of the array, compared with simulations.

compared with simulations. When scanning to 20°, the grating lobe entering in the visible region can be observed at −90°, but its level remains −10 dB below the maximum, because it is weighted by the filtering function of the element pattern.

The frequency dependence of the radiation patterns is highlighted in Fig. 4.12, where the normalized active element pattern of the central element of the array is shown as a function of the angle and the frequency. The patterns remain stable over a variation of about 2 GHz centered at 12 GHz.

4.3 Conclusions

We presented the design of a linear array of dipoles with asymmetric radiation properties. The array elements consist of tilted dipoles with parasitic artificial dielectric layers to

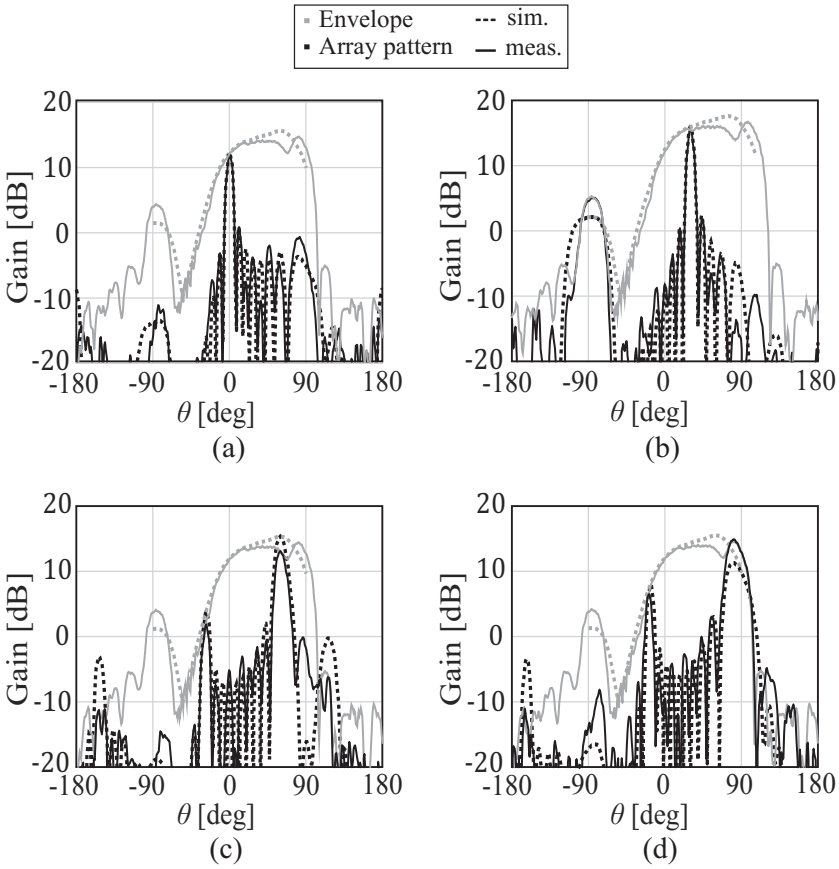

Figure 4.11: Measured and simulated array gain patterns for different scan angles: Scan to (a) $\theta = 0°$, (b) $\theta = 20°$, (c) $\theta = 60°$, (d) $\theta = 90°$.

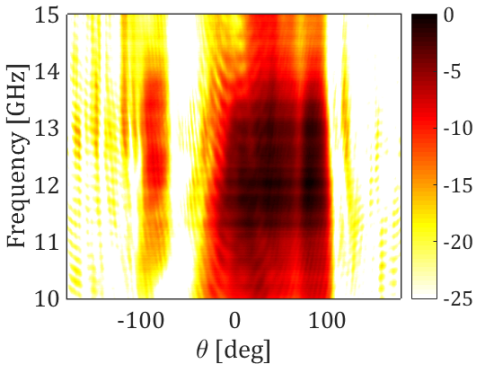

Figure 4.12: Color map of normalized active element patter of element 5 at different frequencies.

enhance their gain. The pattern of such an element can be designed to exhibit a high-gain desired region for angles in the range $\theta_{\text{drop}} < \theta < 90°$ and a low-gain undesired region for $-90° < \theta < \theta_{\text{drop}}$. The angle θ_{drop} can be controlled by the inter-element distance, while

the difference in gain between the desire and undesired regions can be optimized by the tilt angle of the elements. A prototype array based on this concept was presented, showing a good comparison between simulated and measured characteristics.

Chapter 5

Analysis of a 24 GHz Additive Manufactured Antenna

In this chapter, an antenna for a 3D configuration of a miniaturized Frequency Modulated Continuous Wave (FMCW) radar working at 24 GHz is presented, based on the concept described in [82]. The antenna, manufactured using the Stereolithography (SLA) process, consists of a dipole embedded in a polymer slab. A 10.3% bandwidth centered at 22.9 GHz is achieved. The results of the characterization of the polymer material and of the metallic paste used during the fabrication process are discussed. The matching and the radiation patterns of the antenna are measured. The fabrication process for high frequencies appears to be prone to systematic errors. A good agreement between simulations and measurements is achieved after including the deviations found in the geometry of the fabricated antenna. The challenges related to the use of this fabrication process for the manufacture of high frequency RF antennas and components are also discussed.

5.1 Antenna Design

The first step to assess the suitability of Additive Manufacturing (AM) technology for 24 GHz integrated antenna designs, was to design the antenna depicted in Fig. 5.1. The antenna element consists of a half-wavelength dipole operating at a frequency of $f_0 = 24$ GHz enclosed between two dielectric slabs of thickness $t_1 = t_2 = 0.5$ mm. The dielectric constant and loss tangent of the polymer ($\varepsilon_r = 2.74$, $\tan\delta_{@24GHz} = 0.015$) were characterized experimentally and are presented in Sec. 5.2.
The antenna is fed by a 50 Ω co-planar waveguide (CPW) line, excited by an SMA connector (also reported in Fig. 5.1). Since the input impedance of the dipole is approximately 100 Ω,

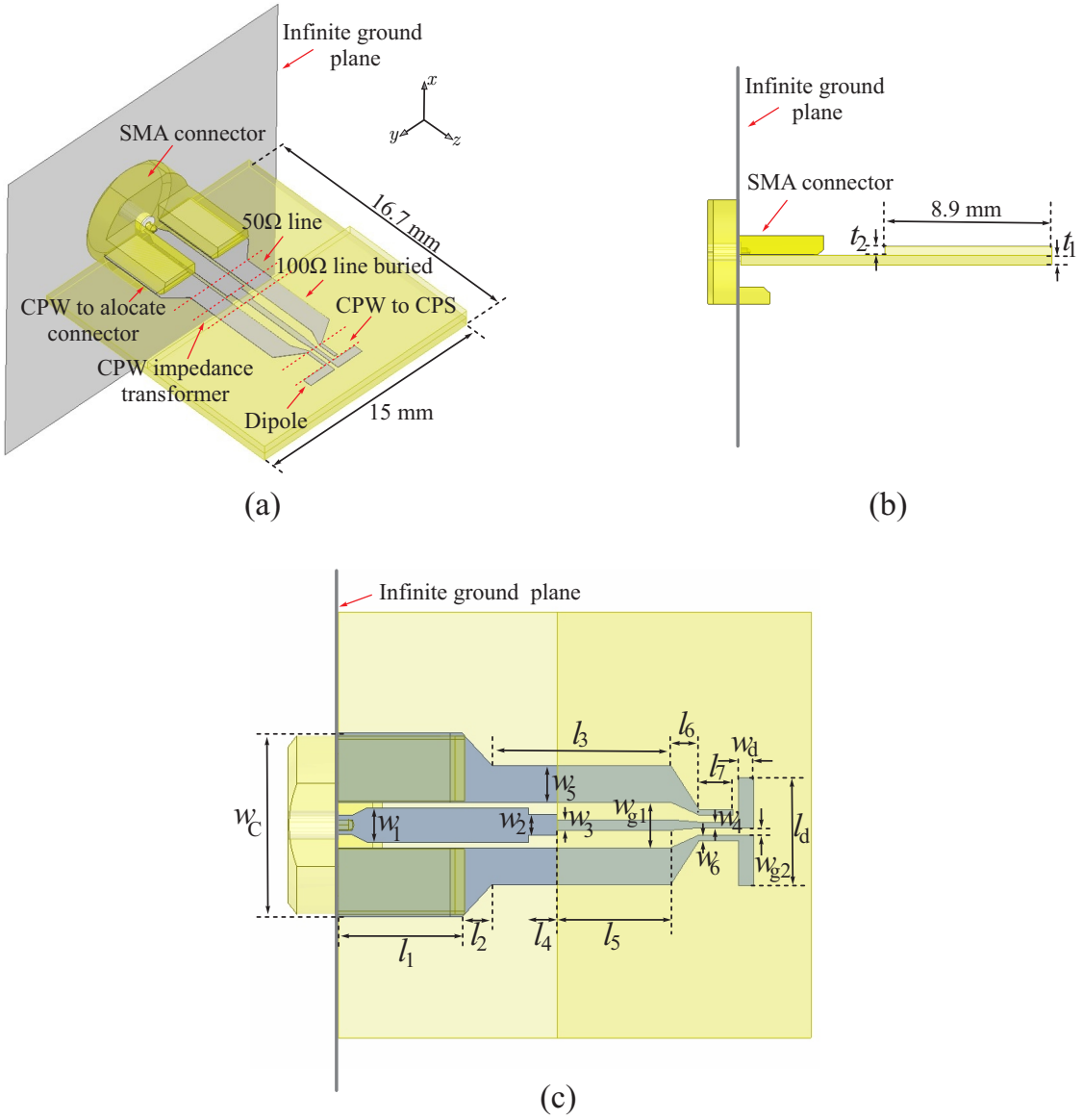

Figure 5.1: (a) 3D view, (b) side view of the simulated antenna including the SMA connector and the ground plane and (c) top view with its geometrical parameters.

a quarter wavelength transformer is implemented to achieve good impedance matching (with $S_{11} < -10$ dB in the operating frequency range). The input line and the transformer are printed over a polymer slab, whereas the last sections of transmission line and the dipole are embedded between two polymer slabs. Therefore, in the line section buried in the dielectric, the central conductor of the CPW is reduced in size, from w_2 to w_3 (see Fig. 5.1(c) and Table 5.1), to keep the same characteristic impedance. A CPW to co-planar strip (CPS) line transition is included in the design to connect the feeding line to the

Table 5.1: Geometrical parameters of the designed antenna (in mm)

w_1	w_2	w_3	w_4	w_5	w_6	w_c	w_{g1}	w_{g2}	w_d
1.122	0.62	0.37	0.2	1.3	0.2	6.35	1.7	0.25	0.5

l_d	l_1	l_2	l_3	l_4	l_5	l_6	l_7	t_1	t_2	t_m
3.6	4.55	1.05	6.3	1	4	1.6	1.2	0.5	0.5	0.100

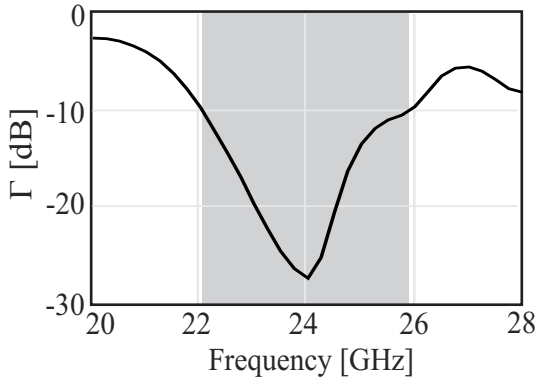

Figure 5.2: Reflection coefficient of the designed antenna with the values shown in Fig. 5.1(c).

dipole. In the considered application, the antenna will be directly connected to the output of the power amplifier of the radar chip and will be thus differentially fed. Therefore, a balun was not included in the design. To avoid back radiation, an infinite ground plane in the xy-plane is included in the simulations and placed at the beginning of the input line (see Figs. 5.1(b) and 5.1(c)). Because of the poor metal conductivity ($\sigma = 2.3 \times 10^6$ S/m, see Sec.

The reflection coefficient is shown in Fig. 5.2. The central operating frequency of the antenna is at 24 GHz with an impedance bandwidth ($\Gamma < -10$ dB) of 16.7%. Figure 5.3 (a) shows the E- and H-plane normalized polar radiation patterns for the central frequency and Fig. 5.3 (b) shows the maximum gain and directivity in the E-plane at broadside for different frequencies. It can be noted that the E-plane is asymmetric because of the asymmetry due to the CPW to CPS transformation. The maximum gain achieved at 24 GHz is 7.6 dB and its directivity is 8.7 dB, resulting in an efficiency of 77%.

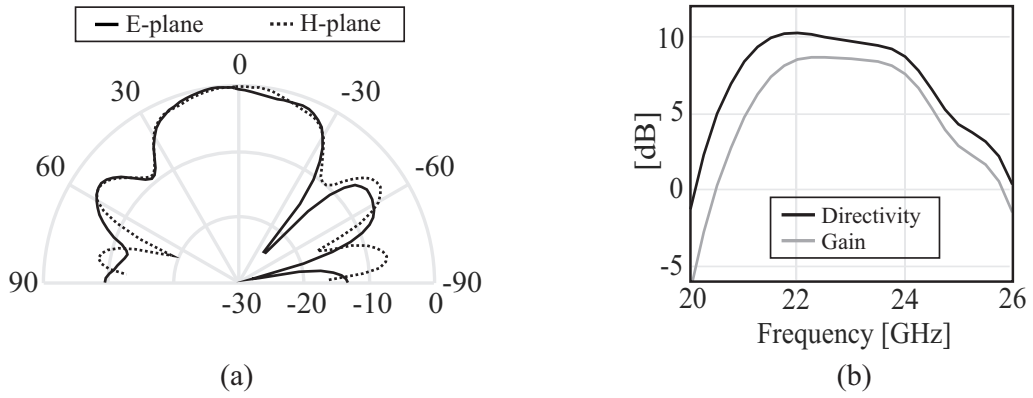

Figure 5.3: (a) E- and H- plane normalized radiation patterns at 24 GHz and (b) maximum gain and directivity as a function of frequency of the designed antenna.

5.2 Characterization of the Materials

Samples of the dielectric material with and without metallic lines were printed with a commercial 3D printer, the RapidShape S60 mini [83], to characterize the polymer and the metal paste used in the fabrication process. The 3D printer uses a Digital Light Processing (DLP) technology, a process similar to Stereolithography (SLA). A LED light source is incorporated in the RapidShape S60 mini, together with a HD resolution DLP projector, to photo cure liquid resin in layers of 50 µm. Figure 5.4 shows an illustration of the printer used in the process. The polymer chosen for manufacturing is a high temperature photopolymer resin containing urethane dimethacrylate (UDMA), Bis-EMA-4 (SR540), 2 wt-% photo-initiator Irgacure 819, and 0.017 wt-% of a blue light-blocking dye; and the metal paste is a silver electron ink containing micro-sized silver flakes from the VFP family [84].

The characterization of the polymer is performed with a cavity resonator [85] at X and Ka-band for several polymer samples of dimensions 60mm x 60mm and thickness 1 mm. The Keysight 85072A split cylinder resonator [85] measures relative permittivity and loss tangent of thin films. The resonator cavity is separated into two halves and the samples are loaded in the gap between this two cylinder halves. The real part of the permittivity, ε', and loss tangent, tanδ, are calculated from the sample thickness, cylinder length and the S-parameters measured with the cavity resonator.

The measured permittivity and dielectric loss tangent (tanδ) are shown in Fig. 5.5 (a) and (b), respectively. To verify the measurements, a control material (rexolite) is used and its measurements are also included in Fig. 5.5, agreeing with the nominal values [86]. In

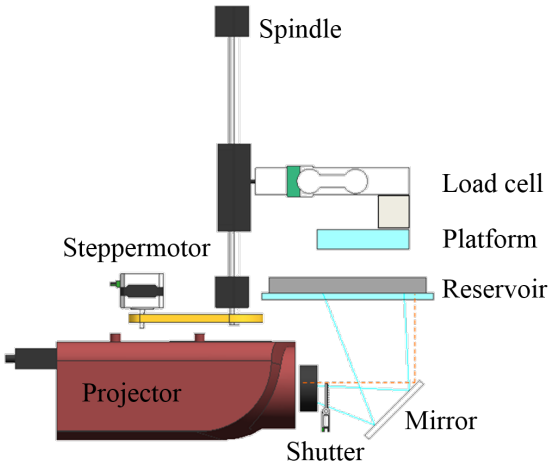

Figure 5.4: Illustration of the 3D printer using Digital Light Processing technology.

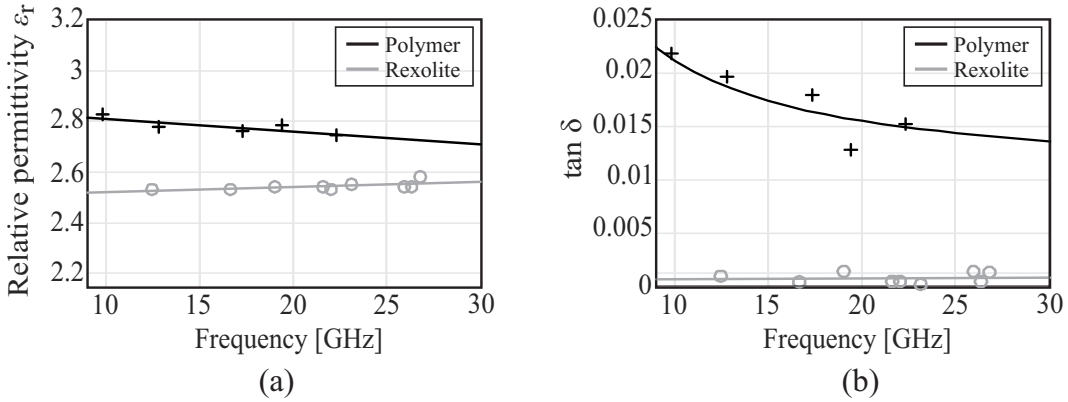

Figure 5.5: (a) Measured permittivity and (b) tanδ of the polymer used to manufacture the antenna.

general, the tanδ can be defined as [87]:

$$\tan\delta = \frac{\omega\varepsilon'' + \sigma}{\omega\varepsilon'} \tag{5.1}$$

where ω is the angular frequency, σ is the conductivity of the material, and ε' and ε'' are the real and imaginary part of the relative permittivity of the material, respectively. For dielectric materials typically used in microwave applications, the conductivity is low and the loss is dominated by the imaginary part of the of the permittivity. The result is an almost constant tanδ as a function of frequency (see the rexolite curve in Fig. 5.5 (b)). For the polymer used in the current design, instead, the tanδ shows an inversely proportional variation as a function of frequency, indicating that the loss is dominated by

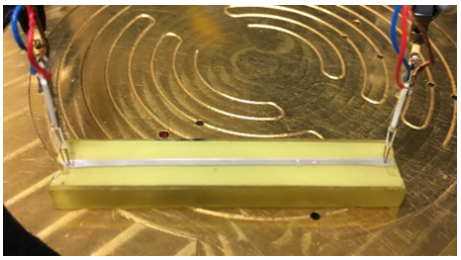

Figure 5.6: Kelvin 4-wire setup with a microstrip transmission line as a subject.

the conductivity of the material. The measured data were fitted using Eq. (5.1) and the corresponding conductivity and imaginary part of the dielectric constant are 0.017 S/m and 0.0305, respectively. The permittivity of the polymer at 24 GHz has been estimated as 2.74 with a tanδ of 0.015.

To characterize the conductivity of the metal paste, a Kelvin 4-wire resistance measurement is performed [88]. This method determines the resistivity ρ of the considered sample measuring the current flowing and the voltage dropping across the sample (see Fig.5.6). This measurement is done with four-point probe (two pair of clip wires) so that the wire resistance and the contact resistance of this probes can be neglected, being the measured voltage the one due to the sample itself. The jaw halves in the Kelvin clips (each pair of wires) are insulated from each other at the joint point, only contacting at the tips where they clasp the wire or terminal of the sample being measured. Thus, the current measured with one of the wires does not go through the other paired wire. This way, the process will not create any error-inducing voltage drop along their length. Knowing the resistance of the material one can find the conductivity by using the following expression:

$$\sigma = \frac{1}{\rho} = \frac{l}{R_{\text{subject}} A} \tag{5.2}$$

where l is the length of the line, R_{subject} is the resistance of the sample measured with the Kelvin measurement equipment, and A is the area of the cross-section of the line. To obtain a more accurate result of the conductivity of the metal paste used to fabricate the antenna, line samples with lengths 5.7 cm and 2.8 cm and metal thickness of 50 µm and 100 µm were measured. The average measured conductivity considering all the samples is approximately 2.3×10^6 S/m , which is approximately 4% of copper conductivity.

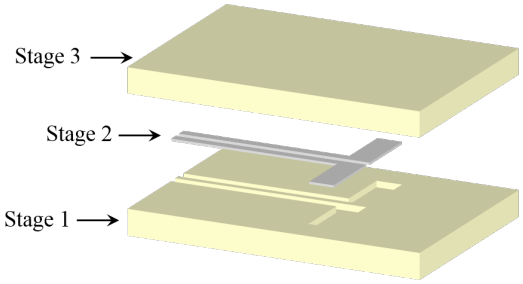

Figure 5.7: Fabrication process: the polymer is printed containing superficial channels (stage 1); then the metal paste is located in the channels and cured (stage 2); finally, a top layer of polymer is printed (stage 3).

5.3 Manufacturing and Experimental Validation

The described antenna is manufactured with the RapidShape S60 mini printer. The overall antenna is printed in 3 different phases (see Fig. 5.7): first the lower part of the polymer is printed, containing superficial channels in the shape of the antenna to locate the metal tracks. The antenna is then removed from the 3D printer to fill the channels with metal paste using the squeegee method. Once the metal is placed in the polymer's printed channels, the antenna is warmed in an oven at 130° for 30 minutes to cure the metal paste. Lastly, the second layer of polymer is printed over the radiating element.

A photograph of the prototype is shown in Fig. 5.8. The geometrical parameters of the antenna were measured using a microscope and are reported in Table 5.2. The measurements resulted in a deviation of about 100 μm in the line width compared to the designed parameters (Table 5.1), while for the line length very small discrepancies were found. A large circular metal plane of radius 10 cm was soldered to the connector to prevent reflections (see Fig. 5.8). It can also be noted a warping on the antenna caused by the difference in temperature suffered while curing the metal paste. Figure 5.9 shows the measured reflection coefficient in comparison with the simulated one with the nominal and measured geometries. A good agreement between the measured and simulated reflection coefficient is achieved when the measured geometrical parameters are used. The simulated antenna design has a bandwidth of 13% centered at 23.25 GHz, while the measured antenna bandwidth is 10.3% centered at 22.9 GHz. Comparing these results with the nominal ones of Section II, it can be noted a 5% frequency shift (from 24 GHz to 22.9 GHz) and a reduction of the bandwidth (from 16.7% to 10.3%).

The antenna radiation pattern is characterized in a near-field cylindrical scanning measurements set-up. The E- and H-plane normalized radiation patterns are shown in Fig.

Table 5.2: Measured geometrical parameters of the fabricated antenna (in mm)

w_1	w_2	w_6	w_{g1}	w_d	l_d	l_3	l_4	l_5	l_7
1.2	0.72	0.185	1.61	0.56	3.8	6.3	0.99	4	1.21

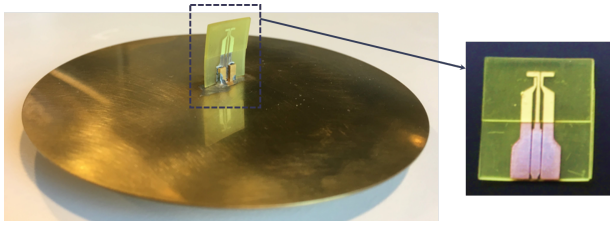

Figure 5.8: Photograph of the fabricated prototype.

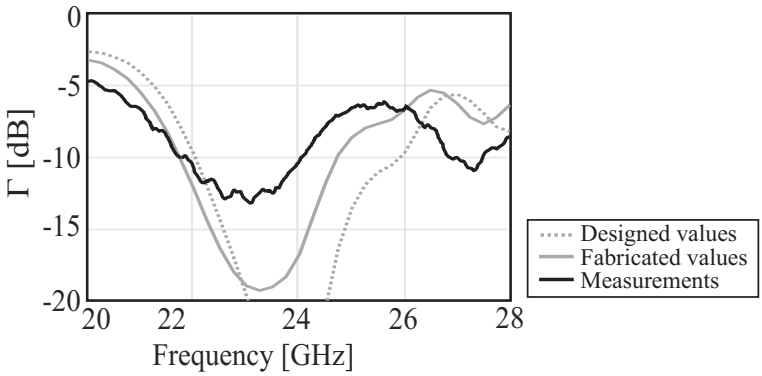

Figure 5.9: Measured (dotted line) reflection coefficient and simulated (solid line) reflection coefficient using the measured dimensions of the fabricated antenna.

5.10 for the frequencies of 22 and 23 GHz and compared to the simulated antenna with the measured geometrical parameters and to the simulated antenna with a finite ground plane as the one attached to the fabricated antenna. A good agreement is achieved in terms of shape of the measured and simulated patterns. The small oscillations in the measured radiation patterns are due to the finiteness of the ground plane (these oscillations are also visible in the simulated antenna patterns with the finite ground plane). Some discrepancies can be noticed in the side lobe level. Figure 5.11 shows the simulated gain curve for frequencies from 20 to 24 GHz and the measured gain at 22 and 23 GHz. The maximum gain measured at 22 GHz is of 8.025 dB and 7.62 dB at 23 GHz, while the simulated gain (using the measured geometrical parameters) at 22 GHz is of 9.2 dB and 8.66 dB at 23 GHz. Therefore, a difference in gain between measurements and simulations of about 1 dB at 22 and 23 GHz was observed. The metal roughness is measured for different samples (trans-

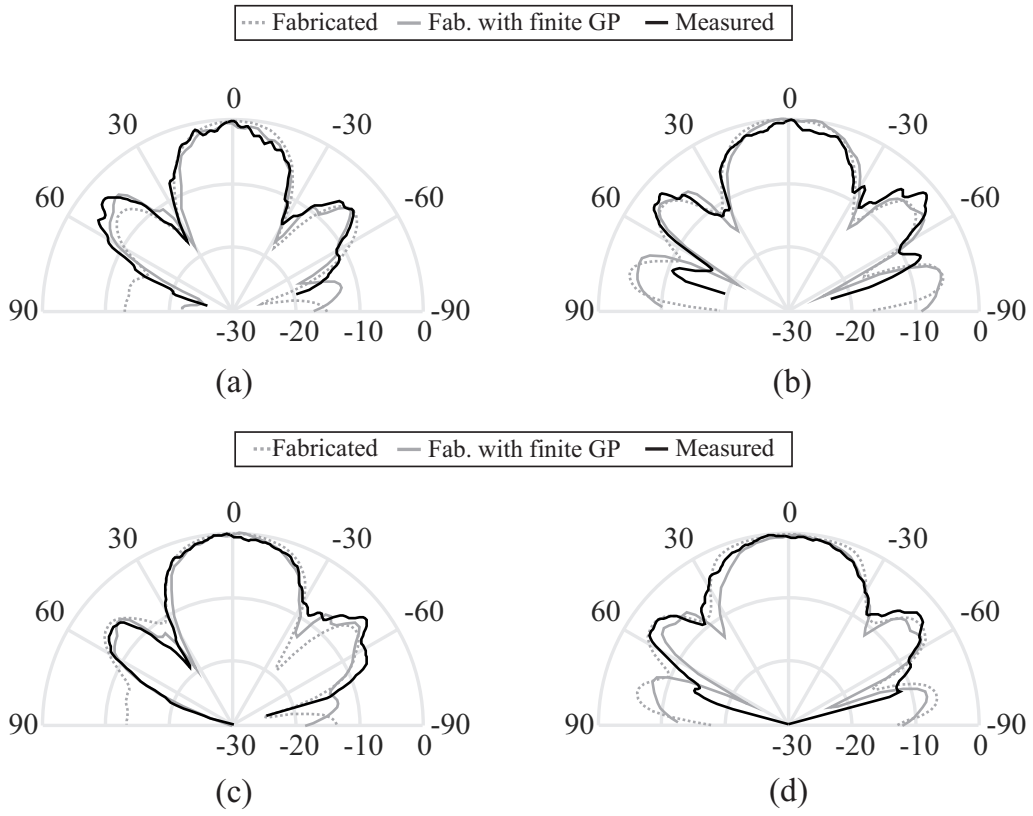

Figure 5.10: Measured (black solid line), simulated with the nominal geometrical parameters (grey solid line) and simulated with the varied geometrical parameters (grey dotted line) radiation patterns: (a) E- and (b) H-plane at 22 GHz; and (c) E- and (d) H-plane at 23 GHz.

mission lines and the dipole antenna) resulting in an average metal roughness of 2 µm. After including this surface roughness in the simulation, it did not result in a significant reduction (around 0.2 dB) in the gain. Knowing the directivity and gain of the simulated antenna with the varied geometrical dimensions and the prototype we can calculate the efficiency of the antenna. Table 5.3 shows the simulated (with the preliminary design and the design considering the geometry dimensions measured) and measured efficiency of the antenna.

Moreover, one can note that the gain values obtained for both simulations and measurements are higher than what expected from a half-wavelength dipole in the presence of backing reflector ($\approx$ 5 dB). The higher gain value is due to the large distance between the dipole and the backing reflector of around $1.75\lambda_d$, where λ_d is the wavelength at 22 GHz inside the dielectric. If we use the image theorem to replace the backing reflector with the image dipole, the two dipoles are at $3.5\lambda_d$ and radiate in phase towards broadside with

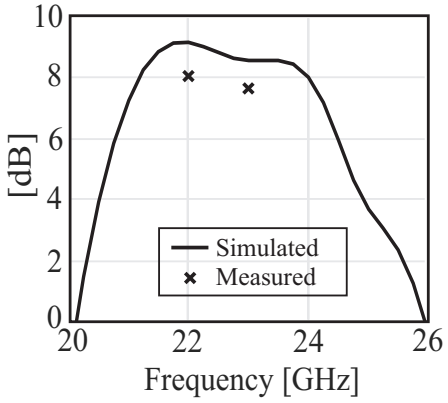

Figure 5.11: Simulated and measured realized gain of the dipole antenna.

Table 5.3: Simulated and measured efficiency

	22 GHz	23 GHz
Designed	83%	79%
Fabricated	74%	78%
Measured	51%	61%

up to 8 dB directivity. The dielectric slab is $1.1\lambda_d$ wide and also contributes to radiation, yielding a higher directivity than the dipole alone. To support this reasoning, the dipole was simulated in the presence of the dielectric slab and the backing reflector, but without the feeding structure, as shown in Fig. 5.12(a). The simulated magnitude of the electric field for the main planes are presented in Fig. 5.12(b) and (c). It can be seen that both the dielectric and ground plane contribute to generate directive radiation at broadside. From simulations, a directivity of more than 10 dB is obtained.

Overall, current mixed-material additive manufacturing methods originally proposed for low frequency electronics, seem to be less suitable for high frequency antennas. The low conductivity of the metal paste and the high losses of the polymer must be improved in order to compete with the standard manufacturing processes. A 3D printer combining metal and polymer would allow for a better control of the temperature variation, limiting warping effects as observed in this work.

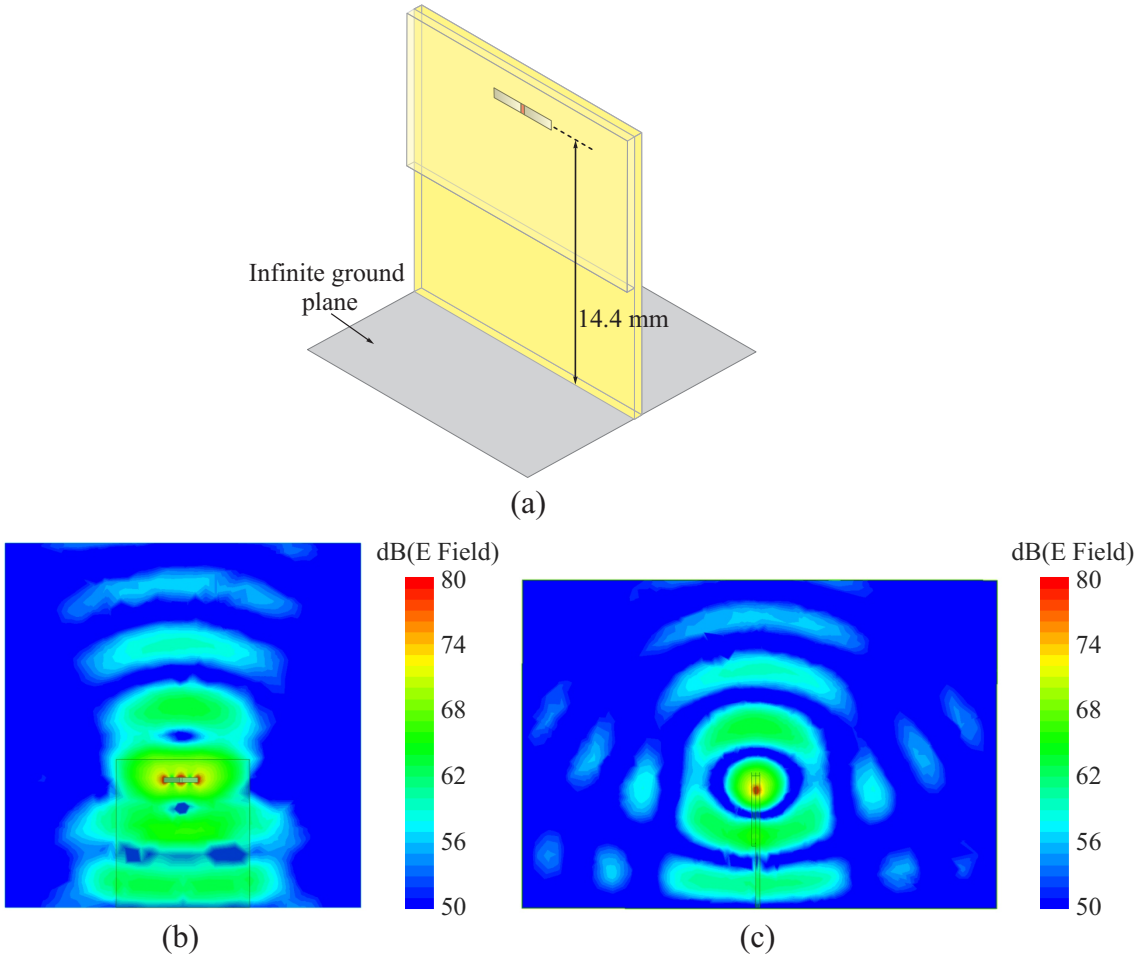

Figure 5.12: (a) Simulated structure with a dipole with an ideal feed and dielectric slabs in the presence of a backing reflector. (b) *E*-plane and (c) *H*-plane of the simulated magnitude of the electric field.

5.4 Conclusions

In this work a 24 GHz antenna design based on TNO additive manufacturing technology for a miniaturized FMCW radar is presented. The dipole antenna is fully embedded in dielectric, of relative permittivity 2.74 and tanδ of 0.015, printed using SLA technique. The dipole is combined with a transmission line integrating an impedance transformer to match the SMA connector impedance. The metal traces are realised with silver electron ink containing micro-sized silver flakes cured in the oven. The results of the characterization of the polymer material and metal paste used in the manufacturing process are presented. The fabricated antenna exhibits a slight frequency shift and reduction of the bandwidth compared to the designed antenna, due to errors in the geometrical parameters of the an-

tenna, as measured with a microscope. The operating frequency band of the manufactured antenna is center at 22.9 GHz and the bandwidth is 10.3%. A good agreement between the simulated and measured radiation patterns in the principle planes at 22 GHz and 23 GHz is achieved, particularly for the main lobe, while small discrepancies were observed in the side lobe level. The antenna efficiency is relatively low due to the high losses of the polymer and of the conductive paste used to realise the metal traces.

Chapter 6

Conclusions and Recommendations

This dissertation described the research work carried out over a period of four years (from September 2015 to September 2019) at Delft University of Technology, in Delft, Netherlands, and at TNO Defence, Safety and Security, in The Hague, Netherlands.
The project dealt with theoretical and practical aspects of frequency selective surfaces and array antenna with asymmetric radiation patterns, covering both analysis and design. These aspects are nowadays of particular interest in the field of military radar and communication systems, because when operating in complex platforms the avoidance of interferences is needed, and can benefit from the implementation of frequency and angular filtering functions.
In this chapter, we summarize the conclusions and the most significant results of the research. In addition, several prototype demonstrators have been developed during the project to validate the studies on the frequency and angular selectivity, and to assess the performance of novel manufacturing techniques.

6.1 Analysis of Frequency Selective Surfaces to Reject Higher Harmonics

To improve the filtering selectivity in phased array antennas, an equivalent circuit model has been derived to represent a Frequency Selective Surface with harmonic rejection properties. As an example, a third order Chebyshev bandpass filter was considered consisting of parallel capacitances and inductances separated by series inductances that can be replaced by short transmission lines. The parallel capacitances and inductances are implemented with metallic square patches and metallic grid, respectively, and the transmission line

sections are represented by dielectric slabs separating the metal layers. A good representation is achieved with the equivalent circuit since the periodicity of the unit cell is much smaller than the wavelength and the behavior of each later can be represented as a shunt impedance with respect to a plane-wave propagation. The designed FSS has been manufactured and the rejection of higher order harmonics was achieved up to three time the working frequency. The fabricated FSS has been tested in the proximity of a connected array antenna consisted of dipoles, where it is shown that within the FSS bandwidth the antenna maintains the same response as the one of the antenna alone, while outside the FSS bandwidth a good isolation was achieved.

6.2 Analysis of Antenna Arrays to Achieve Asymmetric Radiation Properties

In order to find design parameters for phased array antennas to achieve a non-symmetric field of view, a spectral method of moments was developed to study periodic antennas with tilted elements, specifically its impedance and radiation properties. The MoM analyzed tilted dipoles and tilted stacked dipoles in free space and with a backing reflector. For the case of infinite array of tilted dipoles a symmetric active input impedance and radiation pattern are achieved regardless the periodicity of the antenna array. This results can be explained with the fact that, as the dipole radiates the same power upwards and downwards, the same power radiated upwards will be radiated in the opposite direction for the case in free space and in the specular direction for the case with a backing reflector. This result suggested using a more directive element to reduce the power going to undesired directions. For the case of infinite array of stacked dipoles, an asymmetric radiation pattern is achieved in the presence of a backing reflector when the array is under-sampled, while the symmetry of the active input impedance remain the same as for the case of free space.

A parametric analysis on the radiation pattern was carried out to determine the parameters affecting the power radiated in specific directions. It is concluded that the periodicity of the antenna array determines the angle at which the power drop-off occurs, being able to calculate this angle using the expression corresponding to the grating lobe entering the visible region, and the tilt angle of the elements shapes the gain levels in the suppressed angular region.

A spectral method of moment was also developed to investigate the radiation properties of linear arrays comprising a finite number of tilted elements. A parametric analysis is carried out obtaining similar results as for the periodic MoM. To provide guidelines for the design

of arrays with a desired pattern shape, a figure of merit was defined that we referred to as an asymmetry factor depending on the angle at which the drop in gain is chosen. The best values of periodicity and tilt of the elements for the maximum asymmetry possible were collected in a figure to be the guideline for the design of these type of arrays.

6.2.1 Experimental Validation of a Linear Array with Angular Filtering Properties

A linear array of 10 tilted elements was fabricated to prove the theory derived previously. The array consists of tilted dipoles loaded with artificial dielectric layers to improve the directivity of the element as well as the bandwidth. The values of the periodicity and tilt of the elements is chosen from the guideline figure to achieve the maximum asymmetry possible. A realistic feeding structure is design consisting of a microstrip feed with a Marchand balun to avoid the excitation of common mode currents. A good comparison between the simulated and measured linear array characteristics was achieved.

6.3 Analysis of an Additive Manufactured Antenna

To investigate the posibility of using additive manufacturing technologies for the fabrication of phased array antennas working at high frequencies, an antenna dipole was designed and fabricated with a 3D-printer. The dipole antenna if fully embedded in dielectric and the metal traces are realize with a silver paste. The characterization of the polymer and metal material used are found to be significantly lossy for high frequencies and with poor conductivity, respectively. A deviation in the geometrical parameters is also found compared to the simulated ones. Nevertheless, a good agreement of the radiation pattern for different frequencies is achieved, while the efficiency of the measured antenna is reduced due to losses of the polymer and the low conductivity of the metal. Overall, current mixed-material additive manufacturing methods originally proposed for low frequency electronics, seems to be less suitable for high frequency antennas. To achieve a better control in the fabrication process, a 3D printer combining metal and polymer would be useful.

6.4 Future Outlooks

Some important benefits of the spectral method of moment to study tilted elements have been highlighted and demonstrated in this thesis. Possible future research directions that can motivate further developments of the concept, are enlisted below:

- A further step to include filtering properties to phased array antennas would be the design of the FSS together with the phased array. This way, having a combined analytical solution, the distance between the FSS and the array antenna could be reduced, achieving a more compact solution.

- The spectral method of moments was developed for elements in free space or in the presence of a backing reflector. As a future work, the insertion of stratified media in the MoM would allow us to have a more realistic scenario with elements printed on or embedded in a dielectric stratification.

- The study done in this thesis is for single polarized arrays and 1D finite linear arrays. A dual polarization and a 2D array for tilted dipoles could be studied, addressing the issues of 2D scanning and polarization purity.

- A generalization of the study performed in this thesis could be done including other commonly used antenna elements (e.g. patches) and artificial dielectric layers on top of the elements. This would allow to get a better understanding on how the non-symmetric field of view is achieved and how the radiation characteristics of the elements affects this asymmetry.

- A extra degree of freedom could be added in the design including a non uniform tilt of the elements, using different tilt angles for the elements across the array. This solution could provide more degrees of freedom in the optimization of the array to achieve a desired radiation performance.

- The potential advantages of using additive manufacturing methods to fabricate tilted antennas would allow us to design 3D structures that could not be fabricate with standard technologies. In order to make this possible, AM technologies must evolve providing better material properties and manufacturing accuracy.

6.5 Impact of the Research

The work described in this thesis has led to a number of journal and conference publications (listed on p. 117 of this dissertation). The research has been funded by TNO because of its potential in the improvement of phased array performance for a variety of applications. Moreover, the work described in Chapter 5 was awarded with the *Best Innovative Paper Prize* at the 39th ESA Antenna Workshop on Multibeam and Reconfigurable Antennas for Space Applications, in Noordwijk, Netherlands.

Appendix A

Fourier Transform of the Current Profile

The aim of this appendix is to derive the current expression of a dipole projected in the (xyz)-reference system.
Considering the expression in (3.5), an axis transformation is needed in order to express the current in the (xyz)-reference system. This transformation is represented graphically in Fig. A.1 and can be written as follows:

$$\begin{aligned} x &= x_R \cos\alpha + z_R \sin\alpha \\ z &= -x_R \sin\alpha + z_R \cos\alpha \end{aligned} \tag{A.1}$$

Its inverse transformation will be then

$$\begin{aligned} \begin{pmatrix} x \\ z \end{pmatrix} = \begin{pmatrix} \cos\alpha & \sin\alpha \\ -\sin\alpha & \cos\alpha \end{pmatrix} \cdot \begin{pmatrix} x_R \\ z_R \end{pmatrix} \Rightarrow \begin{pmatrix} x_R \\ z_R \end{pmatrix} &= \begin{pmatrix} \cos\alpha & \sin\alpha \\ -\sin\alpha & \cos\alpha \end{pmatrix}^{-1} \cdot \begin{pmatrix} x \\ z \end{pmatrix} \\ &= \frac{1}{cos^2\alpha + \sin^2\alpha} \begin{pmatrix} \cos\alpha & -\sin\alpha \\ \sin\alpha & \cos\alpha \end{pmatrix} \cdot \begin{pmatrix} x \\ z \end{pmatrix} \end{aligned} \tag{A.2}$$

giving the expressions shown in (3.8). If the current is oriented along the unit vector $\hat{\boldsymbol{x}}_R$, the vector can be projected as

$$\hat{\boldsymbol{x}}_R = \hat{\boldsymbol{x}} \cos\alpha - \hat{\boldsymbol{z}} \sin\alpha \tag{A.3}$$

The three-dimensional Fourier transform of the current in (3.10), using the axis transfor-

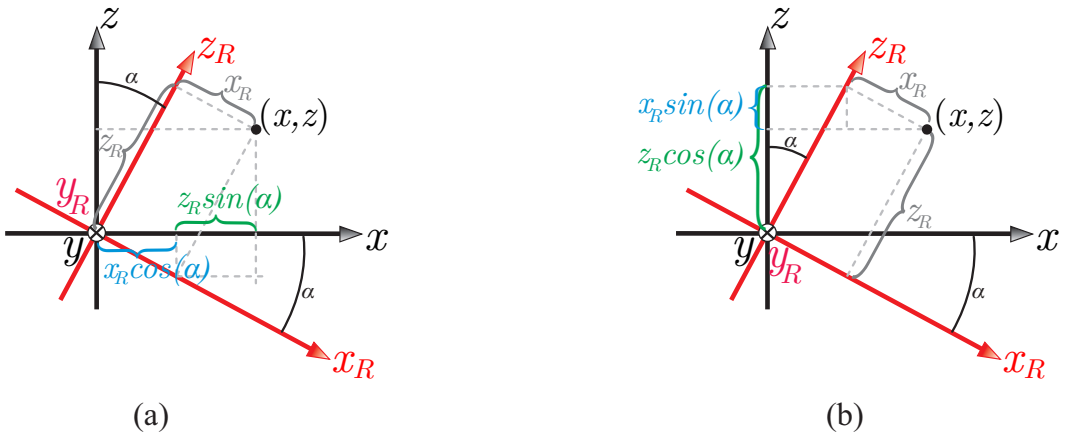

Figure A.1: Representation of the axes rotation and (a) x-axis and (b) z-axis transformation.

mation, can be written as

$$J(k_x,k_y,k_z)=\iiint_V j(x,y,z)e^{jk_x x}e^{jk_y y}e^{jk_z z}dxdydz = \\ i_0\iiint_V b_l(x\cos\alpha - z\sin\alpha)e(y)\delta(x\sin\alpha + z\cos\alpha)\cdot e^{jk_x x}e^{jk_y y}e^{jk_z z}dxdydz \quad (A.4)$$

where V is a volume containing the entire dipole. The integral along y yields the Bessel function of zeroth order. Therefore, the Fourier transform is expressed as a double integral along x and y:

$$J(k_x,k_y,k_z) \;=\; i_0 J_0\Big(\frac{k_y w}{2}\Big)\iint_A b_l(x\cos\alpha - z\sin\alpha)\cdot\delta(x\sin\alpha + z\cos\alpha)e^{jk_x x}e^{jk_z z}dxdz \quad (A.5)$$

where A is the surface of the dipole. We can apply the following change of variables

$$\begin{aligned} x' &= x\cos\alpha - z\sin\alpha \\ z' &= x\sin\alpha + z\cos\alpha \end{aligned} \quad (A.6)$$

As we are working with a change of variable when evaluating a multiple integral of a function over a region within its domain, the Jacobian determinant must be included as a multiplicative factor within the integral. In our case the Jacobian of the transformation equals unity:

$$\det\begin{vmatrix} \frac{dx'}{dx} & \frac{dx'}{dz} \\ \frac{dz'}{dx} & \frac{dz'}{dz} \end{vmatrix} = \det\begin{vmatrix} \cos\alpha & -\sin\alpha \\ \sin\alpha & \cos\alpha \end{vmatrix} = 1\,. \quad (A.7)$$

The expression in (A.5) becomes

$$J(k_x, k_y, k_z) = i_0 J_0\Big(\frac{k_{ym} w}{2}\Big) \iint\limits_A b_l(x')\delta(z') \cdot e^{j(k_x \cos\alpha - k_z \sin\alpha)x'} e^{j(k_x \sin\alpha + k_z \cos\alpha)z'} dx' dz' \,. \tag{A.8}$$

Closing the integral in x' and z' we can find the final expression for the spectral current:

$$J(k_x, k_y, k_z) = i_0 J_0\Big(\frac{k_{ym} w}{2}\Big) B_l(k_x \cos\alpha - k_z \sin\alpha) \,. \tag{A.9}$$

For the case where we are in the presence of a backing reflector, the image dipole will be rotated same angle but in the opposite direction. Following the same steps as we did before, the dipole current distribution rotated an angle $-\alpha$ from the original (xyz)-coordinate system can be written as:

$$j_-(x_{R^-}, y_{R^-}, z_{R^-})\hat{\boldsymbol{x}}_{R^-} = i_0 b_l(x_{R^-}) e(y_{R^-}) \delta(z_{R^-}) \hat{\boldsymbol{x}}_{R^-} \tag{A.10}$$

where $x_{R^-} = x\cos\alpha + z\sin\alpha$, $y_{R^-} = y$, $z_{R^-} = -x\sin\alpha + z\cos\alpha$ and $\hat{\boldsymbol{x}}_{R^-} = \hat{\boldsymbol{x}}\cos\alpha + \hat{\boldsymbol{z}}\sin\alpha$. The Fourier transform of (A.10) with the axes rotation will be

$$J_-(k_x, k_y, k_z) = i_0 J_0\Big(\frac{k_{ym} w}{2}\Big) B_l(k_x \cos\alpha + k_z \sin\alpha) \,. \tag{A.11}$$

Appendix B

Closed-Form Solution of the Active Input Impedance

This appendix presents the steps followed to express the active input impedance in closed form for the case of a tilted dipole in free space and in the presence of a backing reflector, and the mutual impedance in closed form between two skewed tilted dipoles with different lengths.

B.1 Closed Form of the Active Input Impedance of Tilted Dipoles

The active input impedance of a dipole in free space is shown in Eq. (3.13). This expression contains a spectral integral in the k_z-variable:

$$I = \int_{-\infty}^{\infty} B_l^2(k_{x_R}) G_{x_R x_R}(k_{xm}, k_{ym}, k_z) dk_z, \tag{B.1}$$

where $k_{x_R} = k_{xm}\cos\alpha - k_z \sin\alpha$.
The argument of the integral comprises a product between the spectral-domain piece-wise sinusoidal distributions defined in Eq. (3.11). When writing explicitly this product, we obtain, after a few algebraic steps:

$$B_l^2(k_{x_R}) = \Big(\frac{2k_0}{\sin(k_0 l/2)}\Big)^2 \frac{A_1 + A_2(k_{xm}, k_z) + A_3(k_{xm}, k_z)}{(k_0^2 - k_{x_R}^2)^2} \tag{B.2}$$

where

$$\begin{aligned} A_1 &= \frac{1}{2} + \cos^2(k_0 l/2) \\ A_2(k_{xm}, k_z) &= \frac{e^{jk_{x_R} l}}{4} - \cos(k_0 l/2) e^{jk_{x_R} l/2} \\ A_3(k_{xm}, k_z) &= \frac{e^{-jk_{x_R} l}}{4} - \cos(k_0 l/2) e^{-jk_{x_R} l/2}\,. \end{aligned} \tag{B.3}$$

The components of the free-space dyadic spectral Green's function used in Eq. (B.1) can be expressed as

$$\begin{aligned} G_{xx}^{ej}(k_x, k_y, k_z) &= j\frac{\zeta}{k_0}\frac{k_0^2 - k_x^2}{k_0^2 - k_x^2 - k_y^2 - k_z^2} \\ G_{xz}^{ej}(k_x, k_y, k_z) &= j\frac{\zeta}{k_0}\frac{-k_x k_z}{k_0^2 - k_x^2 - k_y^2 - k_z^2} \\ G_{zz}^{ej}(k_x, k_y, k_z) &= j\frac{\zeta}{k_0}\frac{k_0^2 - k_z^2}{k_0^2 - k_x^2 - k_y^2 - k_z^2} \end{aligned} \tag{B.4}$$

The summation of all the components in the definition $G_{x_R x_R} = G_{xx}\cos^2\alpha - 2G_{xz}\sin\alpha\cos\alpha + G_{zz}\sin^2\alpha$ leads to

$$G_{x_R x_R}(k_{xm}, k_{ym}, k_z) = j\frac{\zeta_0}{k_0}\frac{k_0^2 - (k_{xm}\cos\alpha - k_z\sin\alpha)^2}{k_0^2 - k_{xm}^2 - k_{ym}^2 - k_z^2} \tag{B.5}$$

By combining Eq. (B.2) and Eq. (B.5) we can write the integral as

$$I = j\frac{\zeta_0}{k_0}\Big(\frac{2k_0}{\sin(k_0 l/2)}\Big)^2 \int_{-\infty}^{\infty} \frac{1}{k_0^2 - k_{xm}^2 - k_{ym}^2 - k_z^2} \cdot \frac{A_1 + A_2(k_{xm}, k_z) + A_3(k_{xm}, k_z)}{k_0^2 - (k_{xm}\cos\alpha - k_z\sin\alpha)^2} dk_z \tag{B.6}$$

The integrand in Eq. (B.6) contains four poles

$$\begin{aligned} k_{zp1} &= k_{xm}\cot\alpha + k_0\csc\alpha \\ k_{zp2} &= k_{xm}\cot\alpha - k_0\csc\alpha \\ k_{zp3} &= -\sqrt{k_0^2 - k_{xm}^2 - k_{ym}^2} \\ k_{zp4} &= \sqrt{k_0^2 - k_{xm}^2 - k_{ym}^2}\,. \end{aligned} \tag{B.7}$$

The location of these poles in the complex plane can change depending on the Floquet mode indexes, the scan angles and the tilt of the dipoles. For instance, when considering the fundamental Floquet mode ($m_x = m_y = 0$) and scanning to broadside with a tilt of

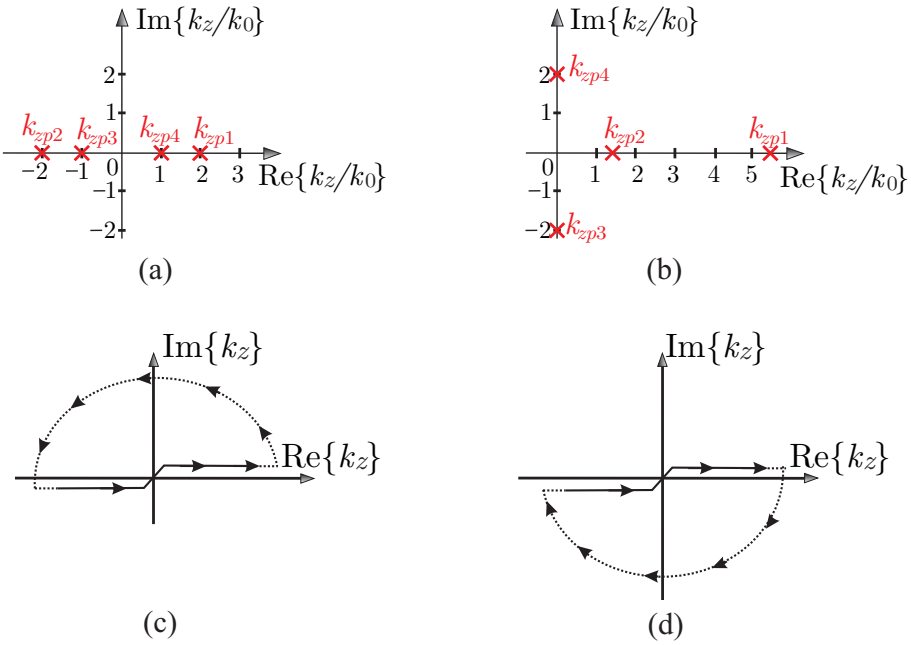

Figure B.1: Locations of the poles scanning at broadside with a tilt of $\alpha = 30°$ considering (a) the fundamental Floquet mode and (b) the mode $m_x = -1, m_y = 0$; and the deformation paths used depending on the convergence of the contributions: (c) upwards and (d) downwards.

$\alpha = 30°$, the poles are located on the real axis as shown in Fig. B.1(a). For the mode $m_x = -1, m_y = 0$ the poles move in the configuration depicted in Fig. B.1(b).
The integral in Eq. (B.6) can be then written in terms of the polar singularities as

$$I = j\frac{\zeta_0}{k_0}\left(\frac{2k_0}{\sin(k_0 l/2)}\right)^2 \cdot \int_{-\infty}^{\infty} (A_1 + A_2(k_{xm}, k_z) + A_3(k_{xm}, k_z)) \prod_{i=1}^{4} \frac{1}{k_z - k_{zpi}} dk_z \,. \tag{B.8}$$

By using the Cauchy theorem, the residue theorem can be applied. To ensure convergence, the integral can be split in three contributions: the path can be deformed at infinity as in Fig. B.1(c) for the terms A_1 and A_2, whereas the deformation in Fig. B.1(d) is considered for A_3. For each of the three contributions, the result of the integral can be obtained as the sum of the residues correspondent to the polar singularities that are enclosed in the pertaining deformation path.
When we are in the presence of a backing reflector the impedance expression will be $Z_{\text{in}} = Z_{\text{self}} + Z_{\text{mutual}}$, where Z_{self} coincides with $Z_{\text{in,fs}}$ in Eq. (3.13), whereas Z_{mutual} can be calculated in a similar way by including a shift $2h$ along the z-axis and an inverse tilt of the image compared to the main dipole as shown in Eq. (3.17). Expression (3.17) contains a spectral integral in the k_z-variable as in the case before:

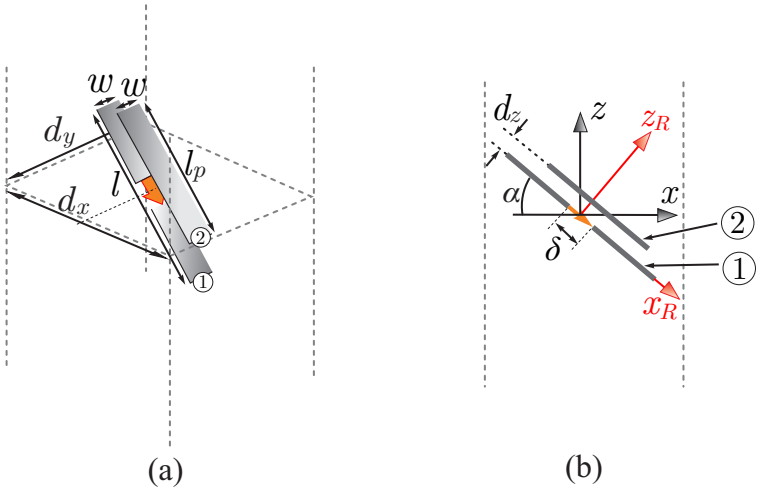

Figure B.2: (a) 3D view and (b) front view of a pair of tilted stacked dipoles.

$$I = \int_{-\infty}^{\infty} B_l(k_{x_{Ri}}) B_l(-k_{x_R}) G_{x_R x_{Ri}}(k_{xm}, k_{ym}, k_z) e^{-jk_z 2h} dk_z, \tag{B.9}$$

where $k_{x_{Ri}} = k_{xm}\cos\alpha + k_z \sin\alpha$ and $G_{x_R x_{Ri}} = -G_{xx}\cos^2\alpha + G_{zz}\sin^2\alpha$.
In this case, as the expression has a negative exponential there will not be a problem with convergence and the residue theorem can be applied directly. The close form expression of Z_{mutual} can be written as

$$Z_{\text{mutual}} = \frac{\zeta}{k_0}\frac{1}{d_x d_y}\frac{1}{2k_{zm}} \sum_{m_x=-\infty}^{\infty} \sum_{m_y=-\infty}^{\infty} J_0^2\Big(\frac{k_{ym} w}{2}\Big) B_l(k_{x_{Ri}}) B_l(-k_{x_R})(-(k_0^2 - k_{xm}^2)\cos^2\alpha + (k_0^2 - k_{zm}^2)\sin^2\alpha) e^{-jk_{zm}2h} \tag{B.10}$$

where $k_{zm} = -\sqrt{k_0^2 - k_{xm}^2 - k_{ym}^2}$.

B.2 Closed Form of the Active Input Impedance of Two Skewed Dipoles

The active input impedance of a pair of tilted stacked dipoles in free space can we written as the summation of the self impedance and the mutual impedance between the pair of dipoles: $Z_1 = Z_{11} + Z_{12}$ and $Z_2 = Z_{22} + Z_{21}$, being Z_1 the active input impedance of dipole

1 and Z_2 the one of dipole 2 (see Fig. B.2). The close form expression of the self impedance can be calculated as in the section above, while the mutual impedance between the pair can be calculated following the steps in Chapter 3 and expressed as:

$$Z_{12,\text{fs}} = \frac{-1}{2\pi d_x d_y} \sum_{m_x=-\infty}^{\infty} \sum_{m_y=-\infty}^{\infty} J_0^2\Big(\frac{k_{ym} w}{2}\Big) \int_{-\infty}^{\infty} B_l(k_{x_R}) B_{l_p}(k_{x_R}) e^{jk_{xm} d_z \sin\alpha} e^{jk_z d_z \cos\alpha} G_{x_R x_R}(k_{xm}, k_{ym}, k_z) dk_z \tag{B.11}$$

$$Z_{21,\text{fs}} = \frac{-1}{2\pi d_x d_y} \sum_{m_x=-\infty}^{\infty} \sum_{m_y=-\infty}^{\infty} J_0^2\Big(\frac{k_{ym} w}{2}\Big) \int_{-\infty}^{\infty} B_l(k_{x_R}) B_{l_p}(k_{x_R}) e^{-jk_{xm} d_z \sin\alpha} e^{-jk_z d_z \cos\alpha} G_{x_R x_R}(k_{xm}, k_{ym}, k_z) dk_z \tag{B.12}$$

where

$$B_{l_p}(k) = \frac{2k_0(\cos(kl_p/2) - \cos(k_0 l_p/2))}{(k_0^2 - k^2)\sin(k_0 l_p/2)}. \tag{B.13}$$

Following similar steps as in section B.1 we can calculate the close form of the mutual impedance between a pair of stacked dipoles. The expressions in Eq. (B.24) and Eq. (B.12) contain a spectral integral in the k_z-variable:

$$I_{Z12} = \int_{-\infty}^{\infty} B_l(k_{x_R}) B_{l_p}(k_{x_R}) e^{jk_{xm} d_z \sin\alpha} e^{jk_z d_z \cos\alpha} G_{x_R x_R}(k_{xm}, k_{ym}, k_z) dk_z, \tag{B.14}$$

$$I_{Z21} = \int_{-\infty}^{\infty} B_l(k_{x_R}) B_{l_p}(k_{x_R}) e^{-jk_{xm} d_z \sin\alpha} e^{-jk_z d_z \cos\alpha} G_{x_R x_R}(k_{xm}, k_{ym}, k_z) dk_z, \tag{B.15}$$

where $k_{x_R} = k_{xm}\cos\alpha - k_z \sin\alpha$.

The product between the spectral-domain piece-wise sinusoidal distributions and the exponentials can be written explicitly after a few algebraic steps:

$$B_l(k_{x_R}) B_{l_p}(k_{x_R}) = \frac{2k_0}{\sin(k_0 l/2)} \frac{2k_0}{\sin(k_0 l_p/2)} \frac{A_{Z_{12}}(k_{xm}, k_z)}{(k_0^2 - k_{x_R}^2)^2} e^{jk_x d_z \sin\alpha} e^{jk_z d_z \cos\alpha} \tag{B.16}$$

$$B_l(k_{x_R}) B_{l_p}(k_{x_R}) = \frac{2k_0}{\sin(k_0 l/2)} \frac{2k_0}{\sin(k_0 l_p/2)} \frac{A_{Z_{21}}(k_{xm}, k_z)}{(k_0^2 - k_{x_R}^2)^2} e^{-jk_x d_z \sin\alpha} e^{-jk_z d_z \cos\alpha} \tag{B.17}$$

where

$$A_{Z_{12}}(k_{xm},k_z)=A_{Z_{21}}(k_{xm},k_z)= \frac{e^{jk_{x_R}(l-l_p)/2}+e^{-jk_{x_R}(l-l_p)/2}}{4}+\frac{e^{jk_{x_R}(l+l_p)/2}+e^{-jk_{x_R}(l+l_p)/2}}{4}-\cos(k_0l/2)\frac{e^{jk_{x_R}l_p/2}+e^{-jk_{x_R}l_p/2}}{2} -\cos(k_0l_p/2)\frac{e^{jk_{x_R}l/2}+e^{-jk_{x_R}l/2}}{2}+\cos(k_0l/2)\cos(k_0l_p/2) \quad \text{(B.18)}$$

By combining Eq. (B.16) and (B.17) with Eq. (B.5) we can write the integrals as

$$I_{Z12}=j\frac{\zeta_0}{k_0}\frac{4k_0^2e^{jk_{xm}d_z\sin\alpha}}{\sin(k_0l/2)\sin(k_0l_p/2)}\int_{-\infty}^{\infty}\frac{1}{k_0^2-k_{xm}^2-k_{ym}^2-k_z^2}\cdot\frac{A_{Z_{12}}(k_{xm},k_z)e^{jk_zd_z\cos\alpha}}{k_0^2-(k_{xm}\cos\alpha-k_z\sin\alpha)^2}dk_z \quad \text{(B.19)}$$

$$I_{Z21}=j\frac{\zeta_0}{k_0}\frac{4k_0^2e^{-jk_{xm}d_z\sin\alpha}}{\sin(k_0l/2)\sin(k_0l_p/2)}\int_{-\infty}^{\infty}\frac{1}{k_0^2-k_{xm}^2-k_{ym}^2-k_z^2}\cdot\frac{A_{Z_{21}}(k_{xm},k_z)e^{-jk_zd_z\cos\alpha}}{k_0^2-(k_{xm}\cos\alpha-k_z\sin\alpha)^2}dk_z \quad \text{(B.20)}$$

The poles contained in the integrand of Eq. (B.19) and Eq. (B.20) are the same found for the active input impedance in Appendix B.1 (see Eq. (B.7)). Therefore, the integrands can be then written in terms of polar singularities as

$$I_{Z12}=j\frac{\zeta_0}{k_0}\frac{4k_0^2e^{jk_{xm}d_z\sin\alpha}}{\sin(k_0l/2)\sin(k_0l_p/2)}\cdot\int_{-\infty}^{\infty}A_{Z_{12}}(k_{xm},k_z)e^{jk_zd_z\cos\alpha}\prod_{i=1}^{4}\frac{1}{k_z-k_{zpi}}dk_z\,, \quad \text{(B.21)}$$

$$I_{Z21}=j\frac{\zeta_0}{k_0}\frac{4k_0^2e^{jk_{xm}d_z\sin\alpha}}{\sin(k_0l/2)\sin(k_0l_p/2)}\cdot\int_{-\infty}^{\infty}A_{Z_{21}}(k_{xm},k_z)e^{-jk_zd_z\cos\alpha}\prod_{i=1}^{4}\frac{1}{k_z-k_{zpi}}dk_z\,. \quad \text{(B.22)}$$

By using the Cauchy theorem, the residue can be applied. To ensure convergence, the integral can be split in three different contributions: the first contribution contains the constant terms of $A_{Z_{12}}$, $\cos(k_0l/2)\cos(k_0l_p/2)$, while the other contributions contain the rest of terms that converge using the deformation paths shown in Fig. B.1(c) and Fig. B.1(d). Unlike for the case in section B.1, the terms of $A_{Z_{12}}$ depend on the sign of the

argument of the exponential $e^{\pm jk_z d_z \cos\alpha}$, the distance d_z between the dipoles, the tilt of elements α and the length of the dipoles l and l_p, and cannot be directly classified in one of the deformations paths mentioned above.

Choosing an specific case: $l = 0.5\lambda$, $l_p = 0.42\lambda$, $\alpha = 30°$ and $d_z = 0.07\lambda$, the terms will be divided as follow

$$\begin{aligned} T_1 &= \cos(k_0 l/2)\cos(k_0 l_p/2) \\ T_2 &= \frac{e^{jk_{x_R}(l-l_p)/2} + e^{-jk_{x_R}(l-l_p)/2}}{4} + \frac{e^{jk_{x_R}(l+l_p)/2}}{4} - \cos(k_0 l/2)\frac{e^{jk_{x_R} l_p/2}}{2} - \cos(k_0 l_p/2)\frac{e^{jk_{x_R} l/2}}{2} \\ T_3 &= \frac{e^{-jk_{x_R}(l+l_p)/2}}{4} - \cos(k_0 l/2)\frac{e^{-jk_{x_R} l_p/2}}{2} - \cos(k_0 l_p/2)\frac{e^{-jk_{x_R} l/2}}{2} \end{aligned} \tag{B.23}$$

For Z_{21}, where the sign of the exponential is negative ($e^{-jk_z d_z \cos\alpha}$), T_1 and T_2 will converge using the deformation path of B.1(d), while T_3 will converge with the path shown in Fig. B.1(c). The convergence of these terms while calculating Z_{12} will be inverted, since the sign of the exponential $e^{jk_z d_z \cos\alpha}$ is positive.

When we are in the presence of a backing reflector the impedance expression of Z_{12} will be $Z_{12} = Z_{\text{self}} + Z_{\text{mutual}}$, where Z_{self} coincides with $Z_{12,fs}$ in Eq. (B.24), whereas Z_{mutual} can be calculated in a similar way by including a shift $2h$ along the z-axis and an inverse tilt of the image compared to the main dipole:

$$\begin{aligned} Z_{1,2\text{im}} = \frac{-1}{2\pi d_x d_y} \sum_{m_x=-\infty}^{\infty} \sum_{m_y=-\infty}^{\infty} J_0^2\Big(\frac{k_{ym} w}{2}\Big) \\ \int_{-\infty}^{\infty} B_l(-k_{x_R}) B_{l_p}(k_{x_{Ri}}) e^{jk_{xm} d_z \sin\alpha} e^{-jk_z d_z \cos\alpha} e^{-jk_z 2h} G_{x_R x_{Ri}}(k_{xm}, k_{ym}, k_z) dk_z \end{aligned} \tag{B.24}$$

where $k_{x_{Ri}} = k_{xm}\cos\alpha + k_z \sin\alpha$ and $G_{x_R x_{Ri}} = -G_{xx}\cos^2\alpha + G_{zz}\sin^2\alpha$.

Following the same steps for Z_{mutual} in section B.1, the close form expression of $Z_{1,2\text{im}}$ can be written as

$$Z_{1,2\text{im}} = \frac{\zeta}{k_0}\frac{1}{d_x d_y}\frac{1}{2k_{zm}}\sum_{m_x=-\infty}^{\infty}\sum_{m_y=-\infty}^{\infty} J_0^2\Big(\frac{k_{ym}w}{2}\Big)B_l(-k_{x_R})B_{l_p}(k_{x_{Ri}})\cdot$$

$$e^{jk_{xm}d_z\sin\alpha}e^{-jk_{zm}d_z\cos\alpha}(-(k_0^2-k_{xm}^2)\cos^2\alpha+(k_0^2-k_{zm}^2)\sin^2\alpha)e^{-jk_{zm}2h} \quad \text{(B.25)}$$

where $k_{zm} = -\sqrt{k_0^2 - k_{xm}^2 - k_{ym}^2}$.
Applying the same steps for Z_{21}, the expression in the presence of a backing reflector will be then $Z_{21} = Z_{12,fs} + Z_{2,1\text{im}}$, where

$$Z_{2,1\text{im}} = \frac{\zeta}{k_0}\frac{1}{d_x d_y}\frac{1}{2k_{zm}}\sum_{m_x=-\infty}^{\infty}\sum_{m_y=-\infty}^{\infty} J_0^2\Big(\frac{k_{ym}w}{2}\Big)B_l(k_{x_{Ri}})B_{l_p}(-k_{x_R})\cdot$$

$$e^{-jk_{xm}d_z\sin\alpha}e^{-jk_{zm}d_z\cos\alpha}(-(k_0^2-k_{xm}^2)\cos^2\alpha+(k_0^2-k_{zm}^2)\sin^2\alpha)e^{-jk_{zm}2h} \quad \text{(B.26)}$$

Appendix C

Symmetry Properties of the Impedance

In this appendix, a proof of the symmetry property of the active input impedance is reported. To simplify the problem, we consider the expression in (3.13), associated with an infinite tilted dipole array in free space. However, the same steps can be followed for all other cases.
If we consider only the fundamental Floquet mode in (3.13) and scan to $\theta = \theta_0$, the active input impedance is

$$Z_{\text{in,fs}}\big|_{m_x=m_y=0,\theta=\theta_0} = \frac{-1}{2\pi d_x d_y} j\frac{\zeta_0}{k_0} J_0^2\Big(\frac{k_{y0}w}{2}\Big)\cdot \int_{-\infty}^{\infty} B_l^2(k_{x0}\cos\alpha - k_z\sin\alpha)\frac{k_0^2-(k_{x0}\cos\alpha-k_z\sin\alpha)^2}{k_0^2-k_{x0}^2-k_{y0}^2-k_z^2}dk_z\,. \quad \text{(C.1)}$$

When scanning in the specular direction $\theta = -\theta_0$, k_{x0} and k_{y0} change sign and, if we apply the change of variable $k_z = -k_z'$, we obtain

$$Z_{\text{in,fs}}\big|_{m_x=m_y=0,\theta=-\theta_0} = \frac{-1}{2\pi d_x d_y} j\frac{\zeta_0}{k_0} J_0^2\Big(-\frac{k_{y0}w}{2}\Big)\cdot \int_{-\infty}^{\infty} B_l^2(k_z'\sin\alpha - k_{x0}\cos\alpha)\frac{k_0^2-(k_z'\sin\alpha-k_{x0}\cos\alpha)^2}{k_0^2-k_{x0}^2-k_z'^2}dk_z'\,. \quad \text{(C.2)}$$

It is then evident that the expressions in (C.1) and (C.2) are identical, since the current spectrum is an even function, i.e. $B_l(k) = B_l(-k)$ and $J_0(k) = J_0(-k)$. Similar steps can

be followed to demonstrate the impedance symmetry for the higher order modes. In this case, the scan impedance for $\theta = \theta_0$ is

$$Z_{\text{in,fs}}\big|_{\theta=\theta_0} = \frac{-1}{2\pi d_x d_y} j\frac{\zeta_0}{k_0} \sum_{m_x=-\infty}^{\infty} \sum_{m_y=-\infty}^{\infty} J_0^2\left(\frac{(k_{y0}-\frac{2\pi m_y}{d_y})w}{2}\right) \int_{-\infty}^{\infty} B_l^2\Big(\Big(k_{x0}-\tfrac{2\pi m_x}{d_x}\Big)\cos\alpha - k_z\sin\alpha\Big) \cdot \frac{k_0^2-\left(\left(k_{x0}-\frac{2\pi m_x}{d_x}\right)\cos\alpha - k_z\sin\alpha\right)^2}{k_0^2-\left(k_{x0}-\frac{2\pi m_x}{d_x}\right)^2-\left(k_{y0}-\frac{2\pi m_y}{d_y}\right)^2-k_z^2} dk_z\,. \quad \text{(C.3)}$$

It is easy to observe that for $\theta = -\theta_0$, by applying the change of variable $k_z = -k_z'$, $m_x = -m_x'$ and $m_y = -m_y'$ we obtain the same expression for the impedance: $Z_{\text{in,fs}}\big|_{\theta=\theta_0} = Z_{\text{in,fs}}\big|_{\theta=-\theta_0}$.

Appendix D

Mutual Impedances Calculations

In this appendix, the approaches taken to calculate the self of mutual impedances of tilted dipoles are explained.

D.1 Close Form of $D_{nn'}(k_{x_R})$

Expression in (3.24) contains a double integral in k_{x_R} and k_y. In order to reduce the computational time, the numerator $D_{nn'}(k_{x_R})$ can be solved in closed form noting that the integral in k_y only depends on the distance between the elements in the Z_R direction.
In the case when $|z_{Rn} - z_{Rn'}| = 0$ and using Eq. (3.16), the expression in (3.25) reduces to

$$D_{nn'}(k_{x_R}) = -\frac{\zeta_0}{2k_0}\frac{1}{2\pi}\int_{-\infty}^{\infty} J_0(k_y w/2)\frac{k_0^2 - k_{x_R}^2}{\sqrt{k_0^2 - k_{x_R}^2 - k_y^2}}dk_y\,. \tag{D.1}$$

where k_0 is the wave number in free space and ζ_0 is free space characteristic impedance. The spectral integral in Eq. (D.1) can be performed analytically by addressing the identity [89]:

$$\int_{-\infty}^{\infty} \frac{J_0(k_y w/2)}{\sqrt{k_0^2 - k_{x_R}^2 - k_y^2}}dk_y = \pi J_0\Big(\frac{w_d}{4}\sqrt{k_0^2 - k_x^2}\Big)H_0^{(2)}\Big(\frac{w_d}{4}\sqrt{k_0^2 - k_x^2}\Big) \tag{D.2}$$

where $H_0^{(2)}$ is the Henkel funtion of the second type and zeroth order. Using expression (D.2) in (D.1), the numerator $D_{nn'}(k_{x_R})$ when $|z_{Rn} - z_{Rn'}| = 0$ can be expressed as

$$D_{nn'}(k_{x_R}) = -\frac{\zeta_0}{4k_0}(k_0^2 - k_{x_R}^2)\Big(\frac{w_d}{4}\sqrt{k_0^2 - k_{x_R}^2}\Big)H_0^{(2)}\Big(\frac{w_d}{4}\sqrt{k_0^2 - k_{x_R}^2}\Big)\,. \tag{D.3}$$

In the case when $|z_{Rn} - z_{Rn'}| \gg w$ Eq. (3.25) reduces to

$$D_{nn'}(k_{x_R}) = -\frac{1}{2\pi}\frac{\zeta_0}{2k_0}(k_0^2 - k_{x_R}^2)\int_{-\infty}^{\infty}\frac{J_0(k_y w/2)e^{-j\sqrt{k_0-k_{x_R}^2-k_y^2}|z_{Rn}-z_{Rn'}|}}{\sqrt{k_0^2-k_{x_R}^2-k_y^2}}dk_y$$
$$\approx -\frac{\zeta_0}{4k_0}(k_0^2 - k_{x_R}^2)H_0^{(2)}\Big(\sqrt{k_0^2-k_{x_R}^2}|z_{Rn}-z_{Rn'}|\Big) \quad \text{(D.4)}$$

D.2 Mutual Impedance Between Dipoles Sufficiently Distant

As mentioned in Chapter 3, the mutual impedance between dipoles tilted the same arbitrary angle can be calculated from [74] and [79] when the distance between the elements is sufficient, e.g. distances larger than 0.25λ. Both approaches contain sine and cosine integrals that can become computationally heavy. For that reason, when implementing these expressions, a method can be used to reduce the computational time of the code [90, 91]. The sine and cosine integral can be written as Taylor series as follows

$$Si(x) = \sum_{n=0}^{\infty}\frac{(-1)^n x^{2n+1}}{(2n+1)(2n+1)!} \quad \text{(D.5)}$$

$$Ci(x) = \gamma + \ln x + \sum_{n=1}^{\infty}\frac{(-1)^n x^{2n}}{(2n)(2n)!} \quad \text{(D.6)}$$

where γ is the Euler's constant.
For small arguments of x, these expressions converge fast. However, for too large values of x do not keep the same condition and the asymptotic series of sine and cosine integral are used instead

$$Si(x) = \frac{\pi}{2} - \frac{\cos x}{x}\Big(1 - \frac{2!}{x^2} + \frac{4!}{x^4} - \frac{6!}{x^6}\cdots\Big) - \frac{\sin x}{x}\Big(\frac{1}{x} - \frac{3!}{x^3} + \frac{5!}{x^5} - \frac{7!}{x^7}\cdots\Big) \quad \text{(D.7)}$$

$$Ci(x) = \frac{\sin x}{x}\Big(1 - \frac{2!}{x^2} + \frac{4!}{x^4} - \frac{6!}{x^6}\cdots\Big) - \frac{\cos x}{x}\Big(\frac{1}{x} - \frac{3!}{x^3} + \frac{5!}{x^5} - \frac{7!}{x^7}\cdots\Big). \quad \text{(D.8)}$$

D.3 Mutual Impedance Between non-Parallel Dipoles

In cases when dipoles tilted by an arbitraty angle are in the presence of a backing reflector, can be represented using the image theorem as real dipoles and virtual dipoles or images.

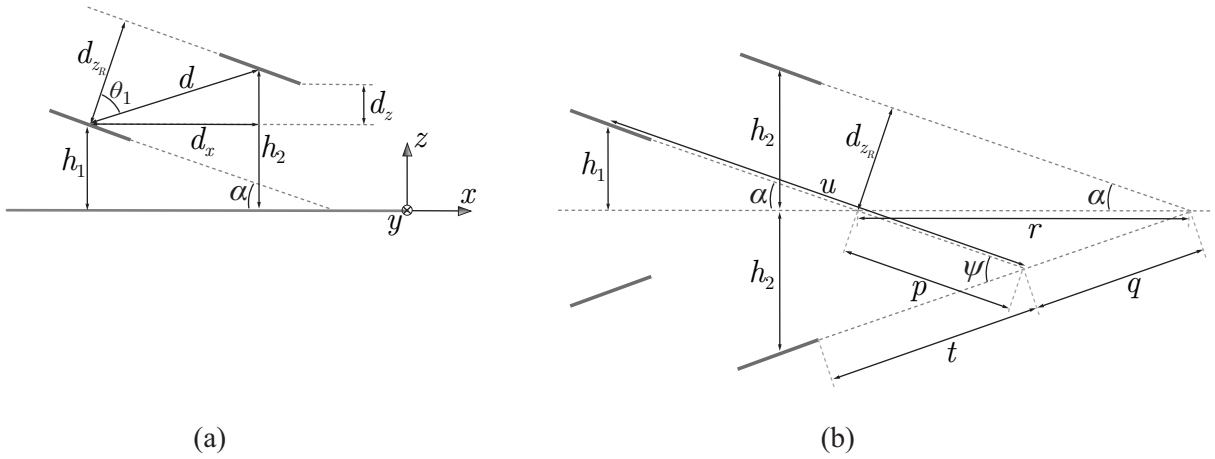

Figure D.1: Two dipoles above a ground plane: (a) original system and (b) equivalent system with dipole images.

In order to be able to use the method of moments, the mutual impedance between dipoles and their images must be calculated. Since the dipoles and their images are skewed with respect to each other, the numerical method described in the appendix sections D.1 and D.2 cannot be used. The mutual impedance between two dipoles of arbitrary length placed at an angle can be calculated analytically using the method described in [80]. Note that in [80] the reference system is defined in terms of z and t. In order to avoid confusion with the original xz-reference system in which the dipoles will be placed, the name of the z-axis in [80] will be changed to the u-axis.

Consider two dipoles above a ground plane as shown in Fig. D.1(a). The original problem is expressed as the equivalent problem shown in Fig. D.1(b).

We decide the location of the dipoles in the xz-reference system, where the ground plane is in the xy-plane and z is oriented normal to the ground plane, as shown in Fig. D.1(a). Therefore h_1, h_2, α and d_x are known. From Fig. D.1(a) d_z can be calculated as $d_z = h_2 - h_1$. The distance between the dipoles, d, can be found using the Pythagorean theorem, $d = \sqrt{d_x^2 + d_z^2}$; and d_{z_R} is found to be $d_{z_R} = \cos(\theta_1)d$, where $\theta_1 = 90 - \alpha - \arctan(\frac{d_z}{d_x})$.

The u- and t-coordinates can be found from Fig. D.1(b). First the length r is found as $r = \frac{d_{z_R}}{\sin\alpha}$. Using the law of sines the lengths of p and q can be found to be $p = q = r\frac{\sin\alpha}{\sin(180° - 2\alpha)}$. From here it can be seen that $u = \frac{h}{\sin\alpha} + p$ and $t = \frac{h_2}{\sin\alpha} - q$, where the angle between the u- and t-axes $\psi = -2\alpha$.

Performing all these steps leads to the final expressions for the u- and t-coordinates and

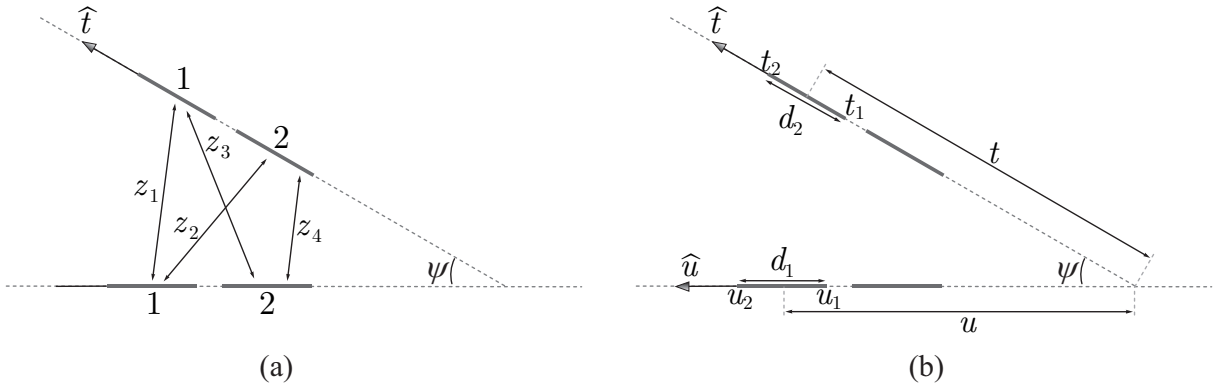

Figure D.2: Two dipoles, both split into monopoles, placed at an angle ψ: (a) mutual impedances Z_1, Z_2, Z_3 and Z_4, and (b) ut-coordinates and monopole dimensions.

the angle ψ as functions of known terms:

$$u = \frac{h}{\sin\alpha} + \frac{\cos(90-\alpha-\arctan(\frac{h_2-h_1}{d_x})\sqrt{d_x^2+(h_2-h_1)^2}}{\sin\alpha}\frac{\sin\alpha}{\sin(180°-2\alpha)} \tag{D.9}$$

$$t = \frac{h_2}{\sin\alpha} - \frac{\cos(90-\alpha-\arctan(\frac{h_2-h_1}{d_x})\sqrt{d_x^2+(h_2-h_1)^2}}{\sin\alpha}\frac{\sin\alpha}{\sin(180°-2\alpha)} \tag{D.10}$$

$$\psi = -2\alpha \tag{D.11}$$

To calculate the mutual impedance between two dipoles, they are divided in two monopoles, as shown in Fig. D.2(a). The mutual impedance between the two dipoles is the sum of the mutual impedance between the monopoles:

$$Z_{mutual} = Z_1 + Z_2 + Z_3 + Z_4 \tag{D.12}$$

where Z_1, Z_2, Z_3 and Z_4 are the mutual impedances between the monopoles, defined as shown in figure D.2(b).
The mutual impedance between two monopoles can be calculated as in [80]:

$$Z_{ij} = (-1)^{i+j}B\left(e^{\gamma t_n}\left(F_{i1} - e^{-\gamma u_m}G_{12} + e^{\gamma u_m}G_{22}\right) - e^{-\gamma t_n}\left(F_{i2} - e^{-\gamma u_m}G_{11} + e^{\gamma u_m}G_{21}\right)\right) \tag{D.13}$$

$$B = \frac{\eta}{16\pi\sinh(\gamma d_1)\sinh(\gamma d_2)} \tag{D.14}$$

where $\gamma = jk_0$, $m = 2/i$ and $n = 2/j$. The functions F_{ik} and G_{kl} are defined as:

$$F_{ik} = 2\sinh(\gamma d_1)e^{(-1)^k u_i\cos(\psi)}E(R_i + (-1)^k\cos(\psi) - (-1)^k t) \tag{D.15}$$

$$G_{kl} = 2E(R_2 + (-1)^k u_2 + (-1)^l t) + 2E(R_1 + (-1)^k u_1 + (-1)^l t) \tag{D.16}$$

R_i is defined as the distance between u_i and the point along d_2 under consideration. The functions E are defined as:

$$E(\alpha) = \int_{\alpha_1}^{\alpha_2} \frac{e^{-\gamma w} dw}{w} \tag{D.17}$$

where α is a function of t, $\alpha_1 = \alpha(t_1)$ and $\alpha_2 = \alpha(t_2)$. For example, if F_{11} is considered it can be seen that the argument of the E-function is equal to $R_1 - \cos(\psi) + t$. The limits α_1 and α_2 from Eq. (D.17) are then:

$$\alpha_1 = \sqrt{(u_1 - t_1 \cos(\psi))^2 + (t_1 \sin(\psi))^2} - \cos(\psi) + t_1 \tag{D.18a}$$

$$\alpha_2 = \sqrt{(u_1 - t_2 \cos(\psi))^2 + (t_2 \sin(\psi))^2} - \cos(\psi) + t_2 \tag{D.18b}$$

Bibliography

[1] A. Abbaspour-Tamijani, J. Rizk and G. Rebeiz, "Integration of filters and microstrip antennas," *Proc. IEEE Antennas Propag. Soc. Int. Symp.*, 2002, pp. 874-877, vol. 2.

[2] T. Le Nadan, J. P. Coupez and C. Person, "Optimization and miniaturization of a filter/antenna multi-function module using a composite ceramic-foam substrate," *IEEE MTT-S Int. Microw. Symp. Digest.*, Anaheim, CA, USA, 1999, pp. 219-222 vol. 1.

[3] L. Cifola, G. Gerini, S. van den Berg and F. van de Water, "Design of an active array filtenna for radar applications," *2014 IEEE Antennas and Propagation Society International Symposium*, Memphis, TN, 2014, pp. 1644-1645.

[4] L. Cifola, G. Gerini, S. van den Berg and F. van de Water, "S-band active array filtenna with enhanced X-band spurious interference suppression," *2014 8th European Conference on Antennas and Propagation*, The Hague, 2014, pp. 737-740.

[5] L. Cifola, D. Cavallo, G. Gerini, and A. Morini, "Compact design of a planar filtering antenna array including a frequency selective common-mode rejection module," *Proc. IEEE Int. Symp. Antennas Propag.*, Chicago, IL, USA, July 8-14, 2012.

[6] F. Bayatpur and K. Sarabandi, "Miniaturized FSS and patch antenna array coupling for angle-independent, high-order spatial filtering," *IEEE Microw. Wireless Compon. Lett.*, vol. 20, no. 2, pp. 7981, Feb. 2010.

[7] B. A. Munk, *Frequency Selective Surfaces: Theory and Design.* New York: Wiley-Interscience, 2000.

[8] S. Monni, A. Neto, G. Gerini, F. Nennie, and A. G. Tijhuis, "Frequency selective surface to prevent interference between radar and SATCOM antennas," *IEEE Antennas Propag. Lett.,* vol. 8, pp. 220-223, Apr. 2009.

[9] M. Al-Joumayly and N. Behdad, "A generalized method for synthesizing low-profile, band-pass frequency selective surfaces with non-resonant constituting elements," *IEEE Trans. Antennas Propag.*, vol. 58, no. 12, pp. 4033-4041, Dec. 2010.

[10] L. B. Withbourn and R. C. Compton, "Equivalent-circuit formulas for metal grid reflectors at a dielectric boundary," *Appl. Opt.*, vol. 24, no. 2, pp. 217-220, Jan. 1985.

[11] S. Momeni Hasan Abadi, M. Li, and N. Behdad, "Harmonic-suppressed miniaturized-element frequency selective surfaces with higher order bandpass responses," *IEEE Trans. Antennas Propag.*, vol. 62, no. 5, pp. 2562-2571, May 2014.

[12] M. Gao, S. M. A. Momeni Hasan Abadi and N. Behdad, "A dual-band, inductively coupled miniaturized-element frequency selective surface with higher order bandpass response," *IEEE Trans. Antennas Propag.*, vol. 64, no. 8, pp. 3729-3734, Aug. 2016.

[13] G. H. Knittel, "Choosing the number of faces of a phased-array antenna for hemispherical scan coverage," *IEEE Trans. Antennas Propag.*, vol. 13, no. 6, pp. 878-882, Nov. 1965.

[14] J. L. Kmentzo, "An analytical approach to the coverage of a hemisphere by N planar phased arrays," *IEEE Trans. Antennas Propag.*, vol. 15, no. 3, pp. 367-371, May 1967.

[15] P. K. Bondyopadhyay, "The cellular scanning concept and its applications," *Proceedings of 2000 Antenna Applications Conference*, Allerton Park, Il, pp. 134-141, Sep. 2000.

[16] R. J. Bolt, D. Cavallo, G. Gerini, D. Deurloo, R. Grooters, A. Neto, and G. Toso, "Characterization of a dual-polarized connected-dipole array for Ku-band mobile terminals," *IEEE Trans. Antennas Propag.*, vol. 64, no. 2, pp. 591-598, Feb. 2016.

[17] A. Catalani, F. Di Paolo, M. Migliorelli, L. Russo, G. Toso, and P. Angeletti, "Ku band hemispherical fully electronic antenna for aircraft in flight entertainment," *Int. J. Antennas Propag.*, vol. 2009, Article ID 230650, pp. 1-7, Mar. 2009.

[18] V. Jamnejad, J. Huang, B. Levitt, T. Pham, and R. Cesarone, "Array antennas for JPL/NASA Deep Space Network," *Proc. IEEE Aerospace Conference*, Big Sky, MT, USA, 2002, pp. 911-921.

[19] H. Steyskal, A. Hessel, and J. Shmoys, "On the gain-versus-scan tradeoffs and the phase gradient synthesis for a cylindrical dome antenna," *IEEE Trans. Antennas Propag.*, vol. TAP-27, no. 6, pp. 825-831, Nov. 1979.

[20] H. Kawahara, H. Deguchi, M. Tsuji, and H. Shigesawa, "Design of rotational dielectric dome with linear array feed for wide-angle multibeam antenna applications," *Electron. Commun. Jpn., Electron.*, vol. 90, no. 5, pp. 49-57, May 2007.

[21] J. Stangel and P. Valentino, "Phased array fed lens antenna," *Patent, US3755815A*, 1971.

[22] A. Benini, E. Martini, S. Monni, M. Viganò, F. Silvestri, E. Gandini, G. Gerini, G. Toso, and S. Maci, "Phase-gradient meta-dome for increasing grating-lobe-free scan-range in phased arrays," *IEEE Trans. Antennas Propag.*, vol. 66, no. 5, pp. 3973-3982, May 2018.

[23] M. Selvanayagam and G. V. Eleftheriades, "Circuit modeling of Huygens surfaces," *IEEE Antennas Wireless Propag. Lett.*, vol. 12, pp. 1642-1645, 2013.

[24] C. Pfeiffer and A. Grbic, "Metamaterial Huygens' surfaces: Tailoring wave fronts with reflectionless sheets," *Phys. Rev. Lett.*, vol. 110, no. 9, p. 197-401, May 2013.

[25] A. Benini, E. Martini, S. Monni, M. C. Viganò, F, Silvestri, E. Gandini, G. Gerini, G. Tosso, and S. Maci, "Phase-Gradient Meta-Dome for Increasing Grating-Lobe-Free Scan Range in Phased Arrays," *IEEE Trans. Antennas Propag.*, vol. 66, no. 8, pp. 3973-3982, Aug. 2018.

[26] E. Magill and H. Wheeler, "Wide-angle impedance matching of a planar array antenna by a dielectric sheet," *IEEE Trans. Antennas Propag.*, vol. 14, no. 1, pp. 49-53, Jan. 1966.

[27] Chao-Chun Chen, "Wideband wide-angle impedance matching and polarization characteristics of circular waveguide phased arrays," *IEEE Trans. Antennas Propag.*, vol. 22, no. 3, pp. 414-418, May 1974.

[28] T. R. Cameron and G. V. Eleftheriades, "Analysis and characterization of a wide-angle impedance matching metasurface for dipole phased arrays," *IEEE Trans. Antennas Propag.*, vol. 63, no. 9, pp. 3928-3938, Sept. 2015.

[29] W. H. Syed, D. Cavallo, H. T. Shivamurthy, and A. Neto, "Wideband, wide-scan planar array of connected slots loaded with artificial dielectric superstrates," *IEEE Trans. Antennas Propag.*, vol. 64, no. 2, pp. 543-553, Feb. 2016.

[30] D. Cavallo, W.H. Syed, and A. Neto, "Connected-slot array with artificial dielectrics: A 6 to 15 GHz dual-pol wide-scan prototype," *IEEE Trans. Antennas Propag.*, vol. 66, no. 6, pp. 3201-3206, Jun. 2018.

[31] F. Tiezzi, S. Vaccaro, D. Llorens, C. Dominguez, and M. Fajardo, "Applications of hybrid phased array antennas for mobile satellite broadband communication user terminals," *34th ESA Antenna Workshop*, Noordwijk, The Netherlands, 3-5 Oct. 2012.

[32] F. Tiezzi, S. Vaccaro, D. Llorens, C. Dominguez, and M. Fajardo, "Ku-band hybrid phased array antennas for mobile satellite communication systems," *7th Eur. Conf. Antennas Propag.*, Gothenburg, Sweden, April 8-12, 2013.

[33] F. Tiezzi, D. Llorens, C. Dominguez, and M. Fajardo, "A compact Ku-band transmit/receive low-profile antenna for broadband mobile satellite communications," *4th Eur. Conf. Antennas Propag.*, pp. 1-4, Barcelona, Spain, 2010.

[34] J. Biosca, D. Llorens, and M. C. Viganó, "Side-lobe reduction with overlapped beamforming network for Ku-band hybrid antenna array," *10th Eur. Conf. Antennas Propag.*, pp. 1-5, Davos, 2016.

[35] A. K. Bhattacharyya, "Active element pattern symmetry for asymmetrical element arrays," *IEEE Antennas Wireless Propag. Lett.*, vol. 6, pp. 275-278, 2007.

[36] H. Steyskal, "On the merit of asymmetric phased array elements," *IEEE Antennas Wireless Propag. Lett.*, vol. 61, no. 7, pp. 3519-3524, Jul. 2013.

[37] R. Hyneman, "A technique for the synthesis of line-source antenna patterns having specified sidelobe behavior," *IEEE Trans. Antennas Propag.*, vol. 16, no. 4, pp. 430-435, Jul. 1968.

[38] R. Elliott, "Design of line source antennas for narrow beamwidth and asymmetric low sidelobes," *IEEE Trans. Antennas Propag.*, vol. 23, no. 1, pp. 100-107, Jan. 1975.

[39] L. Shafai, "Scan gain enhancement in phased arrays by element pattern synthesis," *Proc. IEEE 7th Int. Conf. Antennas Propagation*, Apr. 1991, vol.2, pp. 914-917.

[40] C. Sletten, P. Blacksmith, and G. Forbes, "New method of antennas array synthesis applied to generation of double-step patterns," *IRE Trans. Antennas Propagation*, vol. 5, no. 4, pp. 369-373, Oct. 1957.

[41] A. H. Hussein, H. H. Abdullah, A. M. Salem, S. Khamis, and M. Nasr, "Optimum design of linear antenna arrays using a hybrid MoM/GA algorithm," *IEEE Antennas Wireless Propag. Lett.*, vol. 10, pp. 1232-1235, 2011.

[42] D. Hua, W. Wu, and D. Fang, "Linear array synthesis to obtain broadside and endfire beam patterns using element-level pattern diversity," *IEEE Trans. Antennas Propag.*, vol. 65, no. 6, pp. 2992-3004, Jun. 2017.

[43] P. Franchi and R. Mailloux, "Theoretical and experimental study of metal grid angular filters for sidelobe suppression," *IEEE Trans. Antennas Propag.*, vol. 31, no. 3, pp. 445-450, May 1983.

[44] Y. J. Lee, S. H. Jeong, W. S. Park, J. S. Yun, and S. I. Jeon, "Multilayer spatial angular filter with airgap tuners to suppress grating lobes of 4×1 array antenna," *Electronics Lett.*, vol. 39, no. 1, pp. 15-17, Jan. 2003.

[45] D. Blanco, N. Llombart, and E. Rajo-Iglesias, "On the use of leaky wave phased arrays for the reduction of the grating lobe level," *IEEE Trans. Antennas Propag.*, vol. 62, no. 4, pp. 1789-1795, Apr.2014.

[46] P. Burghignoli, F. Frezza, A. Galli, and G. Schettini, "Synthesis of broad-beam patterns through leaky-wave antennas with rectilinear geometry," *IEEE Antennas Wireless Propag. Lett.*, vol. 2, pp. 136-139, 2003.

[47] A. J. Martinez-Ros, J. L. Gómez-Tornero and G. Goussetis, "Multifunctional angular bandpass filter SIW leaky-wave antenna," *IEEE Antennas Wireless Propag. Lett.*, vol. 16, pp. 936-939, 2017.

[48] C. Menudieret al., "Innovative materials and fabrication process to develop new RF components and concepts," *11th Eur. Conf. Antennas Propag.*, 2017.

[49] A. Kanso et al., "Inkjet printing of Coplanar Wire-Patch antenna on a flexible substrate," *15th International Symposium on Antenna Technology and Applied Electromagnetics*, Toulouse, pp. 1-4, 2012.

[50] M. van der Vorst and J. Gumpinger, "Applicability of 3D printing techniques for compact Ku-band medium/high-gain antennas," *10th Eur. Conf. Antennas Propag.*, Davos, pp. 1-4, 2016.

[51] G. Addamo et al., "3-D Printing of High-Performance Feed Horns From Ku- to V-Bands," *IEEE Antennas Wireless Propag. Lett.*, vol. 17, no. 11, pp. 2036-2040, Nov. 2018.

[52] M. Ahmadloo and P. Mousavi, "A novel integrated dielectric-and-conductive ink 3D printing technique for fabrication of microwave devices," *IEEE MTT-S International Microwave Symposium Digest*, Seattle, WA, pp. 1-3, 2013.

[53] S. Zhang, W. Whittow and J. C. Vardaxoglou, "Additively manufactured artificial materials with metallic meta-atoms," *IET Microwaves, Antennas & Propagation*, vol. 11, no. 14, pp. 1955-1961, 19 11 2017.

[54] D. Filonov, S. Kolen, A. Shmidt, Y. Shacham-Diamand, A. Boag, P. Ginzburg, "Volumetric 3D-Printed Antennas, Manufactured via Selective Polymer Metallization," *Physica Status Solidi (RRL) - Rapid Research Letters*, vol. 13, issue 6, 2019.

[55] "Touch sensor precision 3D printed on Nano Dimensions DragonFly Pro", https://www.nano-di.com/blog/the-ultimate-additive-manufacturing-for-electronics-use-case-round-up

[56] M. I. M. Ghazali, S. Karuppuswami, A. Kaur and P. Chahal, "3-D Printed Air Substrates for the Design and Fabrication of RF Components", *IEEE Trans. on Components, Packaging and Manufacturing Technology*, vol. 7, no. 6, pp. 982-989, June 2017.

[57] M. I. M. Ghazali, S. Karuppuswami, S. Mondal, A. Kaur and P. Chahal, "Embedded Actives Using Additive Manufacturing For High Density RF Circuits and Systems", *IEEE Trans. on Components, Packaging and Manufacturing Technology*, 2019.

[58] J. Kimionis, M. Isakov, B. S. Koh, A. Georgiadis and M. M. Tentzeris, "3D-Printed Origami Packaging With Inkjet-Printed Antennas for RF Harvesting Sensors", *IEEE Trans. on Microwave Theory and Techniques*, vol. 63, no. 12, pp. 4521-4532, Dec. 2015.

[59] C. Yepes, E. Gandini, R. van Dijk, F. Bruning, H. Maalderink, S. Monni and F. E. van Vliet, "Additive Manufactured Antenna in Mixed Material Technology for 24 GHz FMCW Miniaturized Radar," *48th European Microwave Conference*, Madrid, pp. 1417-1420, 2018.

[60] D. Cavallo, A. Neto, G. Gerini, A. Micco, and V. Galdi, "A 3-to 5-GHz wideband array of connected dipoles with low cross polarization and wide-scan capability," *IEEE Trans. Antennas Propag.*, vol. 61, no. 3, pp. 1148-1154, Mar. 2013.

[61] G. Matthaei, *Microwave Filters, Impedance-Matching Networks, and Coupling Structures.* Norwood: Artech House, 1980.

[62] J.-S. Hong and M. J. Lancaster, *Microstrip Filters for RF/Microwave Applications.* New York: John Wiley & Sons, Inc., 2001.

[63] O. Luukkonen, C. Simovski, G. Granet, G. Goussetis, D. Lioubtchenko, A. V. Räisänen, and S. A. Tretyakov, "Simple and accurate analytical model of planar grids and high-impedance surfaces comprising metal strips or patches," *IEEE Trans. Antennas Propag.*, vol. 56, no. 6, pp. 1624-1632, Jun. 2008.

[64] D. Cavallo, W. H. Syed and A. Neto, "Closed-form analysis of artificial dielectric layers Part I: Properties of a single layer under plane wave incidence," *IEEE Trans. Antennas Propag.*, vol. 62, no. 12, pp. 6265-6273, Dec. 2014.

[65] "CST Microwave Studio 2015," Available: http://www.cst.com.

[66] C. Yepes, D. Cavallo, A. Neto, E. Gandini, S. Monni and F. E. van Vliet, "Subwavelength frequency selective surface design for improved antenna array out-of-band rejection," *IEEE Int. Symp. Phased Array Systems Technology*, Waltham, MA, 2016, pp. 1-5.

[67] M. Kominami, D. Pozar, and D. Schaubert, "Dipole and slot elements and arrays on semi-infinite substrates," *IEEE Trans. Antennas Propag.*, vol. 33, no. 6, pp. 600-607, Jun. 1985.

[68] D. Kwon and D. M. Pozar, "Energy storage and radiation Q of infinite planar dipole phased arrays," *IEEE Trans. Antennas Propag.*, vol. 62, no. 1, pp. 153-162, Jan. 2014.

[69] Chich-Hsing Tsao and R. Mittra, "Spectral-domain analysis of frequency selective surfaces comprised of periodic arrays of cross dipoles and Jerusalem crosses," *IEEE Trans. Antennas Propag.*, vol. 32, no. 5, pp. 478-486, May 1984.

[70] A. Neto and S. Maci, "Green's function for an infinite slot printed between two homogeneous dielectrics. I. Magnetic currents," *IEEE Trans. Antennas Propag.*, vol. 51, no. 7, pp. 1572-1581, July 2003.

[71] R. F. Harrington, *Field Computation by Moment Methods.* Piscataway: IEEE Press, 1993.

[72] "Ansys HFSS, Ansys, Inc.", Available: htto://www.ansys.com

[73] R. C. Hansen, *Phased Array Antennas.* John Wiley and Sons, Inc.: New York, 2001.

[74] C. A. Balanis, *Antenna theory: Analysis and design, 3rd ed.* Hoboken: John Wiley & Sons, 2005.

[75] A. Clemente, M. Pigeon, L. Rudant and C. Delaveaud, "Design of a super directive four-element compact antenna array using spherical wave expansion," *IEEE Trans. Antennas Propag.*, vol. 63, no. 11, pp.4715-4722, Nov. 2015.

[76] A. Ishimaru, R. Coe, G. Miller, and W. Geren, "Finite periodic structure approach to large scanning array problems," *IEEE Trans. Antennas Propag.*, vol. 33, no. 11, pp. 1213-1220, Nov. 1985.

[77] A. K. Skrivervik and J. R. Mosig, "Analysis of finite phase arrays of microstrip patches," *IEEE Trans. Antennas Propag.*, vol. 41, no. 8, pp. 1105-1114, Aug. 1993.

[78] D. Cavallo, "Connected array antennas: Analysis and design," Ph.D. Dissertation, Eindhoven University of Technology, Eindhoven, The Netherlands, Nov. 2011.

[79] H. King, "Mutual impedance of unequal length antennas in echelon," *IRE Trans. Antennas Propag.*, vol. 5, no. 3, pp. 306-313, Jul. 1957.

[80] J. H. Richmond and N.H. Geary, "Mutual impedance of nonplanar-skew sinusoidal dipoles," *IEEE Trans. Antennas Propag.*, vol. AP-23, pp. 412-414, May 1975.

[81] C. Yepes, E. Gandini, S. Monni, A. Neto, F. E. van Vliet, and D. Cavallo, "Analysis of tilted dipole arrays: Impedance and radiation properties," *IEEE Trans. Antennas Propag.*, doi: 10.1109/TAP.2019.2938838, Dec. 2019.

[82] E. M. Suijker, R. J. Bolt, M. van Wanum, M. van Heijningen, A. P. M. Maas and F. E. van Vliet, "Low cost low power 24 GHz FMCW radar transceiver for indoor presence detection," *44th European Microwave Conference*, Rome, pp. 1758-1761, 2014.

[83] https://www.aniwaa.com/product/3d-printers/rapidshape-s60-mini/

[84] http://vfp-ink-technologies.com/wp-content/uploads/sites/4/2016/02/Silver-Electron-Ink-1.pdf

[85] https://www.keysight.com/en/pd-1078775-pn-85072A/10-ghz-splitcylinder-resonator?&cc=NL&lc=dut

[86] http://www.rexolite.com/specifications/

[87] D. M. Pozar, *Microwave Engineering, 4th ed.* Hoboken: John Wiley & Sons, 2012.

[88] D. K. Schroder, *Semiconductor material and device characterization, 3rd ed.* Hoboken: John Wiley & Sons, 2006.

[89] A. P. Prudnikov, Yu. A. Brychkov, and O. I. Marichev, *Integral and Series, Volume 2: Special Functions.* Amsterdam: Gordon and Breach Science Publisher, 1986.

[90] M. Abramowitz, I. A. Stegun, *Handbook of Mathematical Functions with Formulas, Graphs, and Mathematical Tables.* New York: United States Department of Commerce, National Bureau of Standards; Dover Publications, 1964.

[91] W. H. Press, S. A. Teukolsky, W. T. Vetterling, B. P. Flannery, *Numerical Recipes: The Art of Scientific Computing (3rd ed.).* New York: Cambridge University Press, 2007.

List of Publications

Journal Papers

J1. C. Yepes, D. Cavallo, E. Gandini, S. Monni, A. Neto and F. E. van Vliet, "Angularly Stable Frequency Selective Surface Combined with a Wide-Scan Phased Array," *IEEE Trans. Antennas Propag.*, vol. 66, no. 2, pp. 1046-1051, Feb. 2018.

J2. C. Yepes, E. Gandini, S. Monni, A. Neto, F. E. van Vliet, and D. Cavallo, "Analysis of Tilted Dipole Arrays: Impedance and Radiation Properties," *IEEE Trans. Antennas Propag.*, accepted for publication, doi: 10.1109/TAP.2019.2938838, Dec. 2019.

J3. C. Yepes, E. Gandini, S. Monni, A. Neto, F. E. van Vliet and D. Cavallo, "A Linear Array of Skewed Dipoles with Asymmetric Radiation Pattern for Angular Filtering," *IEEE Trans. Antennas Propag.*, awaiting recommendation.

Conference Papers

C1. C. Yepes, D. Cavallo, A. Neto, E. Gandini, S. Monni and F. E. van Vliet, "Sub-wavelength Frequency Selective Surface Design for Improved Antenna Array Out-of-Band Rejection," *IEEE International Symposium on Phased Array Systems and Technology (PAST)*, Waltham, MA, October 18-21, pp. 1-5, 2016.

C2. C. Yepes, D. Cavallo, A. Neto, E. Gandini, S. Monni and F. E. van Vliet, "Co-Design of Frequency Selective Surface and Antenna Array with Low Angular Depence," *11th European Conference on Antennas and Propagation (EUCAP 2017)*, Paris, France, March 19-24, 2017.

C3. C. Yepes, D. Cavallo, A. Neto, E. Gandini, S. Monni and F. E. van Vliet, "Frequency Selective Surface for Spatial Filtering of Wide-Angle Scanning Phased Ar-

rays," *IEEE AP-S Symposium on Antennas and Propagation and USNC-URSI Radio Science Meeting*, San Diego, California, July 9-14, 2017.

C4. C. Yepes, D. Cavallo, A. Neto, E. Gandini, S. Monni and F. E. van Vliet, "Spatial Filtering Frequency Selective Surface for Wide-angle Scanning Phased Arrays," *47th European Microwave Conference*, Nuremberg, Germany, 2017, pp. 596-599.

C5. C. Yepes, R. van Schelven, D. Cavallo, A. Neto, E. Gandini, S. Monni and F. E. van Vliet, "Radiation Characteristics of Skewed Loaded Dipoles Arrays," *12th European Conference on Antennas and Propagation*, London, UK, April 9-13, 2018.

C6. C. Yepes, R. van Schelven, D. Cavallo, E. Gandini, S. Monni, F. E. van Vliet, and A. Neto, "On the Radiation Properties of Array of Skewed Stacked Dipoles," *11th IEEE AP-S Symposium on Antennas and Propagation and USNC-URSI Radio Science Meeting*, Boston, Massachusetts, July 8-13, 2018.

C7. C. Yepes, E. Gandini, R. van Dijk, F. Bruning, H. Maalderink, and S. Monni, "Additive Manufactured Antenna in Mixed Material Technology for 24 GHz FMCW Miniaturized Radar," *48th European Microwave Conference*, Madrid, Spain, 2018, , pp. 397-400.

C8. C. Yepes, R. van Schelven, D. Cavallo, E. Gandini, S. Monni, F. E. van Vliet, and A. Neto, "On the Radiation Properties of Skewed Stacked Dipoles Arrays," *39th ESA Antenna Workshop on Multibeam and Multibeam and Reconfigurable Antennas for Space Applications*, Noordwijk, Netherlands, October 2-4, 2018.

C9. C. Yepes, E. Gandini, S. Monni, R. van Dijk, F. Bruning, H. Maalderink and F. E. van Vliet, "24 GHz Additive Manufactured Antenna in Mixed Material Technology," *39th ESA Antenna Workshop on Multibeam and Multibeam and Reconfigurable Antennas for Space Applications*, Noordwijk, Netherlands, October 2-4, 2018.

C10. C. Yepes, E. Gandini, S. Monni, F. E. van Vliet, D. Cavallo, and A. Neto, "3D Array Element Design for Pattern Shaping," *13th European Conference on Antennas and Propagation*, Krakow, Poland, March 31-April 5, 2019. (**Convened paper**)

C11. C. Yepes, E. Gandini, S. Monni, R. van Dijk and F.E. van Vliet, "24GHz Additive Manufacture Antenna in Mixed Material Technology," *13th European Conference on Antennas and Propagation*, Krakow, Poland, March 31-April 5, 2019. (**Convened paper**)

C12. C. Yepes, E. Gandini, S. Monni, F. E. van Vliet, A. Neto and D. Cavallo, "Theory and Design of an Array of Skewed Stacked Dipoles," *IEEE AP-S Symposium on Antennas and Propagation and USNC-URSI Radio Science Meeting*, Atlanta, Georgia, July 7-12, 2019.

C13. C. Yepes, E. Gandini, S. Monni, F. E. van Vliet, A. Neto and D. Cavallo, "Analysis and Design of Arrays with Tilted Directive Dipole Elements," *49th European Microwave Conference*, Paris, France, September 29 - October 4, 2019.

C14. C. Yepes, E. Gandini, S. Monni, F. E. van Vliet, A. Neto and D. Cavallo, "An Array of Tilted Dipoles Loaded with Artificial Dielectrics with an Asymmetric Pattern," *IEEE International Symposium on Phased Array Systems and Technology (PAST)*, Waltham, MA, October 15-18, 2019.

Thesis Co-Supervised

T1. R. van Schelven, "Analysis of three dimensional array antenna elements to achieve asymmetric active element patterns," M.Sc. thesis, Delft University of Technology, Delft, The Netherlands, 2017.

Awards

A1. "Best Innovative Paper Prize" at the 39th ESA Antenna Workshop on Multibeam and Reconfigurable Antennas for Space Applications, 2-4 October, Noordwijk, Netherlands, with the paper "24 GHz Additive Manufactured Antenna in Mixed Material Technology". Coauthors: Erio Gandini, Stefania Monni, Raymond van Dijk, Fabien Bruning, Hessel Maalderink and Frank E. van Vliet.

Summary

3D Elements for Phased-Array Systems: Analysis and Design

In recent years, radar systems and satellite communications require phased array antennas that are capable of incorporating frequency and angular selectivity while maintaining a low profile. Active phased array antennas must comply with stringent requirements in terms of sensitivity to interference caused by other nearby radiating systems, especially in complex platforms, where a multitude of sensors and radiating systems need to co-exist. In such environments, antennas working at different frequencies can interfere with each other and the implementation of frequency filtering functions with a good out-of-band rejection are needed. Moreover, the interference between different systems can be mitigated by reducing the radiation in the direct path between them. For this purpose, angular filtering functions for pattern shaping can be beneficial. However, standard planar printed circuit board technology puts constraints on the possible antenna elements that can be realized to achieve frequency and angular selectivity. Thus, using new methods such as additive manufacturing technology and 3D printing can provide more degrees of freedom to fabricate complex geometries with a desired operation.

For these reasons, this work focuses on studying new solutions for frequency selectivity with rejection of higher order harmonics, developing a spectral method of moment to study antennas to achieve angular shaping and finding the guidelines needed to design such antennas, and testing additive manufacturing technology to find its suitability at high frequencies for phased array antennas.

A bandpass miniaturize-element frequency selective surface with harmonic rejection properties has been designed and manufactured. The design is based on an equivalent circuit model, taking a 3-pole Chebyshev bandpass filter as a starting point, where the inter-layer interaction is only described with a single transmission line representing the fundamental Floquet wave. The prototype consists of five metallic layers, interdigitated patches and grids, separated by dielectric slabs and exhibiting good stability over a wide conical incidence range. A practical case to estimate the effects of placing the FSS in the prox-

imity of a wide-scanning wideband connected array of dipoles has been performed. The performance of the array combined with the FSS has been experimentally characterized, defining the optimal distance between FSS and array to avoid the propagation of surface waves between both structures, showing a good response within the FSS bandwidth and a good frequency rejection outside of this bandwidth.

A spectral method of moments for tilted elements in free space and in the presence of a backing reflector for infinite and finite arrays has been derived. Such method allows to study dipole and stacked dipole elements and find the guidelines needed to design, in a future, a phased array antenna with an undesired angular range where suppression of gain is intended. The parametric study concluded that the main parameters that shapes the pattern are the inter-element distance between elements and the tilt angle of the elements. The requirements to achieve an asymmetric radiation pattern are a directive element and an inter-elements distance higher than half wavelength, while the tilt of the elements allows to shape the gain levels in the suppressed angular region. To validate this study a linear arrays consisting of tilted dipoles loaded with artificial dielectric layers has been fabricated. The prototype shows a good comparison with simulations and measurements.

A simple design of a dipole antenna has been derived and fabricated using Stereolithography process as an additive manufacturing method. The polymer and metal paste used in the process have been characterized and results have been discussed. A good agreement between simulations and measurements has been achieved after including the geometric deviations found in the fabricated antenna. The fabrication process for high frequencies appears to be prone to systematic errors and the challenges related to the use of additive manufacturing technology for high frequency RF antennas and components has been discussed.

Samenvatting

3D-elementen voor antennestelsel systemen: analyse en ontwerp

In de afgelopen jaren hebben radarsystemen en systemen voor satellietcommunicatie antennestelsels met een laag profiel nodig, die frequentie- en hoekselectieve eigenschappen kunnen hebben. Actieve antennestelsels moeten voldoen aan strenge eisen op het gebied van gevoeligheid voor interferentie veroorzaakt door andere stralingssystemen in de buurt, met name in complexe platforms, waar een groot aantal sensoren en stralingssystemen in de buurt van elkaar moeten werken. In dergelijke omgevingen kunnen antennes die op verschillende frequenties werken elkaar storen en is de implementatie van frequentiefilterfuncties met een goede afwijzing van een gewenste band nodig. Bovendien kan de interferentie tussen verschillende systemen worden beperkt door de straling in het directe pad tussen de systemen te verminderen. Voor dit doel kunnen hoekfilterfuncties voor patroonvorming voordelig zijn. De standaard planaire printplaattechnologie legt echter beperkingen op aan de mogelijke antenne-elementen die kunnen worden gerealiseerd om frequentie- en hoekselectiviteit te bereiken. Het gebruik van nieuwe methoden zoals additieve productietechnologie en 3D-printen kan dus meer vrijheidsgraden bieden om complexe geometrien met een gewenste functie te fabriceren.

Om deze redenen richt dit werk zich op het bestuderen van nieuwe oplossingen voor frequentieselectiviteit met afwijzing van hogere orde harmonischen, het ontwikkelen van een spectrale moment methode om antennes te bestuderen om patroonvorming in het elevatievlak te bereiken en het vinden van de richtlijnen die nodig zijn om dergelijke antennes te ontwerpen, en het testen van additieve productietechnologie om zijn geschiktheid te vinden bij hoge frequenties voor antennestelsels.

Een frequentieselectief oppervlak (FSO) voor banddoorlaatminiaturisatie-elementen met harmonische afwijzingseigenschappen is ontworpen en vervaardigd. Het ontwerp is gebaseerd op een equivalent circuitmodel, met een 3-polig Chebyshev-banddoorlaatfilter als uitgangspunt, waar de interactie tussen lagen alleen wordt beschreven met een enkele transmissielijn, die de fundamentele Floquet-golf vertegenwoordigt. Het prototype bestaat uit

vijf metallische lagen, in elkaar grijpende plaatjes en rasters, gescheiden door diëlektrische platen en vertoont een goede stabiliteit over een breed conisch invalsbereik. Een praktische casus om de effecten van het plaatsen van het FSO in de nabijheid van een breedgestuurd breedband verbonden stelsel van dipolen te schatten, is uitgevoerd. De prestaties van het stelsel in combinatie met het FSO zijn experimenteel gekarakteriseerd, waarbij de optimale afstand tussen het FSO en het stelsel is gedefinieerd om de propagatie van oppervlaktegolven tussen beide structuren te voorkomen, met een goede respons binnen de FSO-bandbreedte en een goede frequentieafwijzing buiten deze bandbreedte .

Een spectrale moment methode voor gekantelde elementen in vacuüm en in de aanwezigheid van een achtergrondreflector voor oneindige en eindige stelsels is afgeleid. Een dergelijke methode maakt het mogelijk dipool- en gestapelde dipoolelementen te bestuderen en de richtlijnen te vinden die nodig zijn om in de toekomst een antennestelsel te ontwerpen met een ongewenst hoekbereik, waar onderdrukking van versterking is bedoeld. De parametrische studie concludeerde dat de afstand tussen elementen en de kantelhoek van de elementen de belangrijkste parameters die het patroon vormen zijn. De vereisten om een asymmetrisch stralingspatroon te realiseren zijn gerichte elementen en een afstand groter dan een halve golflengte tussen de elementen, terwijl de kanteling van de elementen het mogelijk maakt om de versterkingsniveaus in het onderdrukte hoekgebied te vormen. Om deze studie te valideren, zijn lineaire stelsels gefabriceerd die bestaan uit gekantelde dipolen die zijn geladen met kunstmatige diëlektrische lagen. Het prototype toont een goede overeenkomst met simulaties en metingen.

Een eenvoudig ontwerp van een dipoolantenne is afgeleid en gefabriceerd met behulp van stereolithografieproces als een additieve productiemethode. De in het proces gebruikte polymeer en metaalpasta zijn gekarakteriseerd en de resultaten zijn besproken. Een goede overeenkomst tussen simulaties en metingen is bereikt na het opnemen van de geometrische afwijkingen in de gefabriceerde antenne. Het fabricageproces voor hoge frequenties lijkt vatbaar voor systematische fouten en de uitdagingen met betrekking tot het gebruik van additieve productietechnologie voor hoogfrequente RF-antennes en componenten zijn besproken.

About the Author

Cristina Yepes was born on August 2, 1990 in Abarán, Murcia, Spain. She received her M.Sc. degree in Telecommunication Engineering from Public University of Navarra, Navarra, Spain, in April 2015. For her B.Sc. thesis, she carried out a nine-months internship with Antenna Group at the Electrical and Electronic Engineering Department, Public University of Navarra, from July 2014 to April 2015. The project dealt with an investigation of the performance of metamaterial structures used to design tunable antennas, under the supervision of prof. dr. ir. Ramón Gonzalo.

From September 2015, she started working towards the Ph.D. degree at the THz Sensing Group in the Microelectronics department of the Electrical Engineering, Mathematics and Computer Science (EEMCS) faculty at Delft University of Technology, Delft, Netherlands; in collaboration with the Antenna Group of the Radar Technology department at TNO Defense, Safety and Security, The Hague, Netherlands. Her Ph.D. topic was about the analysis and design of phased array antenna with a non-symmetric radiation pattern and of frequency selective surfaces with angular stability and higher order harmonics rejection. The research has resulted in four journal publications and fourteen conference papers This research has been carried out in under the supervision of prof.dr.ir. A. Neto as a promotor, prof.dr.ir. F.E. van Vliet as a promotor, and dr.ir. D. Cavallo as a copromotor, dr.ir. E. Gandini and dr.ir. S. Monni as supervisors.

During her Ph.D., she has co-supervised one M.Sc. student R. van Schelven (Delft University of Technology and TNO Defense, Safety and Security).

She was first author of the paper awarded with the best innovative paper prize at the 39th ESA Antenna Workshop in 2018.